



KTH Electrical Engineering

Online power transformer diagnostics using multiple modes of microwave radiation

MARIANA DALARSSON

Licentiate Thesis
Stockholm, Sweden 2013

TRITA-EE 2013:033
ISSN 1653-5146
ISBN 978-91-7501-832-4

Elektroteknisk teori och konstruktion
Teknikringen 33
SE-100 44 Stockholm
SWEDEN

Akademisk avhandling som med tillstånd av Kungl Tekniska högskolan framlägges till offentlig granskning för avläggande av teknologie licentiatexamen fredagen den 25 oktober 2013 klockan 10.00 i sal H1, Teknikringen 33, Kungl Tekniska högskolan, Valhallavägen 79, Stockholm.

© Mariana Dalarsson, Oktober 2013

Tryck: Universitetsservice US AB

Abstract

In the present thesis, we propose and investigate a new approach to diagnose the effects of the various degradation mechanisms, including thermal degradation at hot spots, winding deformations due to the mechanical forces from short circuit currents, partial discharges due to local electric field surges, and increased moisture levels in the cellulose insulation due to decomposition, that affect electric power transformers during their normal operation in an electric power grid.

Although the proposed diagnostics method can in principle be used to detect various degradation mechanisms mentioned above, we focus in the present thesis on mechanical deformations of transformer winding structures. Such mechanical deformations are most often caused by mechanical forces from short circuit currents, but they may also be caused by initial manufacturing errors and inconsistencies not detected by the power transformers' suppliers quality assurance processes.

We model a transformer winding surrounded by the transformer-tank wall and the magnetic core as a two-dimensional parallel plate waveguide or as a three-dimensional coaxial waveguide, where one metallic boundary (plate or cylinder) represents the wall of the transformer tank and the other metallic boundary (plate or cylinder) represents the iron core that conducts the magnetic flux. In between there is a set of parallel or coaxial conductors representing the winding segments.

The new principle proposed in the present thesis is to insert a number of antennas into a transformer tank to radiate and measure microwave fields interacting with metallic structures and insulation. The responses from the emitted microwave radiation are expected to be sensitive to material properties that reflect the changes caused by any harmful deterioration processes mentioned above. Specifically, we investigate the mechanical deformations of transformer winding structures by determining the locations of the individual winding segments or turns, using measurements of the scattered fields at both ends of the winding structure. We solve the propagation problem using conventional waveguide theory, including mode-matching and cascading techniques.

The inverse problem is solved using modified steepest-descent optimization methods. The optimization model is tested by comparing our calculated scattering data with synthetic measurement data generated by the commercial program HFSS.

A good agreement is obtained between the calculated and measured positions of winding segments for a number of studied cases, which indicates that the diagnostics method proposed in the present thesis could be potentially useful as a basis for the design of a future commercial on-line winding monitoring device. However, further development of the theoretical analysis of a number of typical winding deformations, improvements of the optimization algorithms and a practical study with measurements on an actual power transformer structure are all needed to make an attempt to design a commercial winding monitoring device feasible.

Acknowledgments

It is my pleasure to express my gratitude to a number of people without whom this work would not be possible. First of all I thank my parents, who motivated me to get my education and supported me in all my achievements. Another person who greatly influenced my life and career is my professor at the Royal Institute of Technology Dr. Martin Norgren who opened the possibility for me first to do my MSc thesis and subsequently to join the School of Electrical Engineering at the Royal Institute as a PhD student.

I would like to thank the Swedish Energy Agency, who are funding my research through Project Nr 34146-1. My work has also been part of KIC InnoEnergy through the CIPower innovation project.

Otherwise, I am generally very grateful to all the colleagues at the School of Electrical Engineering, with whom I have a good fortune to interact, particularly to my former fellow PhD student and co-author Dr. Alireza Motevasselian. Finally, although it is not possible to mention them all, I would like to express my sincere gratitude to a large number of people from other departments of the Royal Institute of Technology, who have to various extent contributed to the success of my education and subsequent research.

List of papers

This thesis consists of a general thesis text and the following scientific papers:

Papers included in the thesis:

- I. M. Dalarsson, A. Motevasselian and M. Norgren, “*Online power transformer diagnostics using multiple modes of microwave radiation to reconstruct winding conductor locations*”, Inverse Problems in Science and Engineering, Vol. 21, DOI 10.1080/17415977.2013.827182, 2013.
- II. M. Dalarsson, A. Motevasselian and M. Norgren, “*Using multiple modes to reconstruct conductor locations in a cylindrical model of a power transformer winding*”, International Journal of Applied Electromagnetics and Mechanics, Vol. 41, No. 3, DOI 10.3233/JAE-121612, 2013.
- III. M. Dalarsson and M. Norgren, “*First-order perturbation approach to elliptic winding deformations*”, URSI-EMTS 2013 Proceedings, Hiroshima, Japan, May 20-24, 2013.
- IV. M. Dalarsson and M. Norgren, “*Conductor locations reconstruction in a cylindrical winding model*”, PIERS 2013 Proceedings, Stockholm, Sweden, August 12-15, 2013.

Papers not included but relevant to the thesis:

- V. M. Dalarsson, A. Motevasselian and M. Norgren, “*On using multiple modes to reconstruct conductor locations in a power transformer winding*”, PIERS 2012 Proceedings, Kuala Lumpur, Malaysia, March 27-30, pp. 516-523, 2012.
- VI. M. Norgren and M. Dalarsson, “*Reconstruction of boundary perturbations in a waveguide*”, URSI-EMTS 2013 Proceedings, Hiroshima, Japan, May 20-24, 2013.

The author’s contribution to the included papers

I performed the main part of the work in the papers included in this thesis. Martin Norgren suggested the topic and provided the initial theoretical basis for the continued work in Paper I. Thereafter, Martin Norgren proposed a number of additional theoretical improvements in Papers II - IV. Alireza Motevasselian provided the initial HFSS simulations used in Papers I - II.

Contents

Contents	ix
1 Introduction	1
1.1 General	1
1.2 Power transformer fundamentals	1
1.3 Radial winding deformations	5
1.4 Transformer diagnostic methods	9
1.5 Models for wave propagation analysis	11
1.6 Aim of the present thesis	12
1.7 Thesis disposition	13
2 Parallel-plate model	15
2.1 Transformer model description	15
2.2 Parallel-plate waveguides	17
2.3 Mode-matching analysis of TM waves	20
2.4 Scattering analysis of TM waves	30
2.5 Scattering matrices for TM waves	35
2.6 Cascading of two cells	37
3 Approximate cylindrical model	41
3.1 Transformer model description	41
3.2 TM waves in cylindrical waveguides	43
3.3 TM waves in a coaxial cylindrical waveguide	45
3.4 Approximate coaxial waveguide model	48
4 Elliptical perturbation model	51
4.1 The unperturbed problem description	52
4.2 The first-order perturbation model	52
4.3 Mode-matching in the perturbation model	56
5 Exact coaxial model with Bessel functions	57
5.1 TM waves in a coaxial waveguide revisited	57
5.2 Mode-matching analysis in an axially symmetric cylindrical case	61

6	Results and interpretation	69
6.1	Optimization principles	69
6.2	Parallel-plate model	69
6.3	Approximate coaxial model	75
6.4	Elliptic perturbation model	76
6.5	Exact coaxial model with Bessel functions.	76
7	Conclusions and future work	79
	Bibliography	83
A	General waveguide theory	87

Chapter 1

Introduction

1.1 General

Power transformers are critical components in the electric power grid and their occasional failures may result in major power outages in their geographical areas. During their operation, power transformers are subject to several degradation mechanisms. These include thermal degradation at hot spots, partial discharges due to local electric field surges, increased levels of moisture in the cellulose insulation due to decomposition, as well as winding deformations due to mechanical forces from short circuit currents or manufacturing errors [1], [2].

This thesis focuses on detecting the radial mechanical winding deformations in power transformers. The present method can in principle be used to detect the effects of the other degradation mechanisms mentioned above, but the current investigation is limited to detection of radial mechanical winding deformations only. They are therefore described in more detail in Section 1.3 below, while no detailed accounts of other abovementioned degradation mechanisms are included, since they are less related to the scope of the present study.

1.2 Power transformer fundamentals

An electric power transformer is an electrical machine that changes the voltage level of the electrical power supplied to its primary terminals to a higher voltage level (step-up transformer) or a lower voltage level (step-down transformer) by means of inductive coupling between its winding circuits (primary and secondary winding). An applied AC-voltage over the primary winding gives rise to an AC-current in the primary winding and consequently creates a varying magnetic induction in the iron core as well as a varying magnetic flux through the secondary winding. This varying magnetic flux induces a voltage over the secondary winding. Depending on the ratio between the numbers of turns in the primary and secondary winding, a transformer may be a step-up transformer or a step-down transformer. The princi-

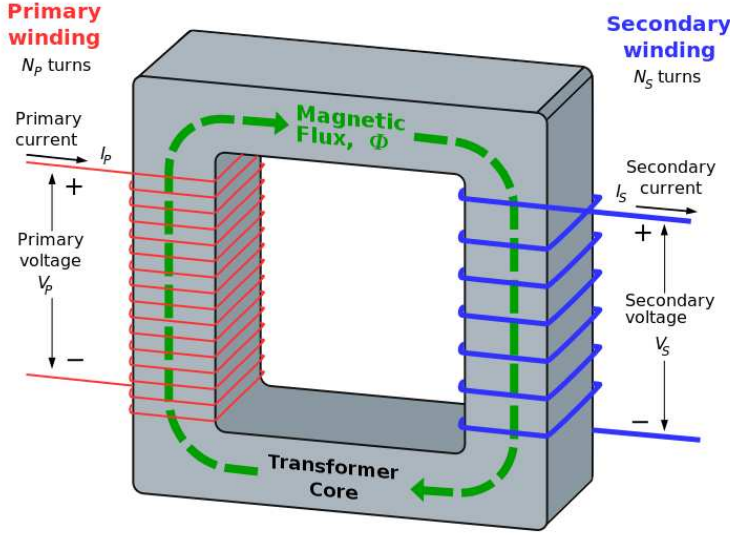


Figure 1.1: Principal sketch of a transformer [3].

ples of the power transformer function are illustrated in Fig. 1.1.

It should be noted that Fig. 1.1 is merely a principal sketch of a transformer as a circuit element and that the actual mechanical structure of practical power transformers is very different from the mechanical structure that seems to be implied by this principal sketch. From Fig. 1.1, it is easily seen that for an ideal, lossless, perfectly-coupled transformer with primary and secondary windings having N_P and N_S turns, respectively, one has the following relationship between the secondary voltage U_S and primary voltage U_P

$$\frac{U_S}{U_P} = \frac{N_S}{N_P} \quad . \quad (1.1)$$

The ideal transformer model described above [3] is based on a number of approximations, such as the neglecting of the losses in the iron core and winding conductors, and the assumption that the transformer windings have zero impedance.

Power transformer windings

Power transformer windings are cylindrical in shape and wound as concentric rings. The windings are manufactured in dust-free temperature controlled winding workshops using paper insulated high-conductivity copper wires [4]. For insulation between layers and turns, it is customary to use pressboard with proper electrical

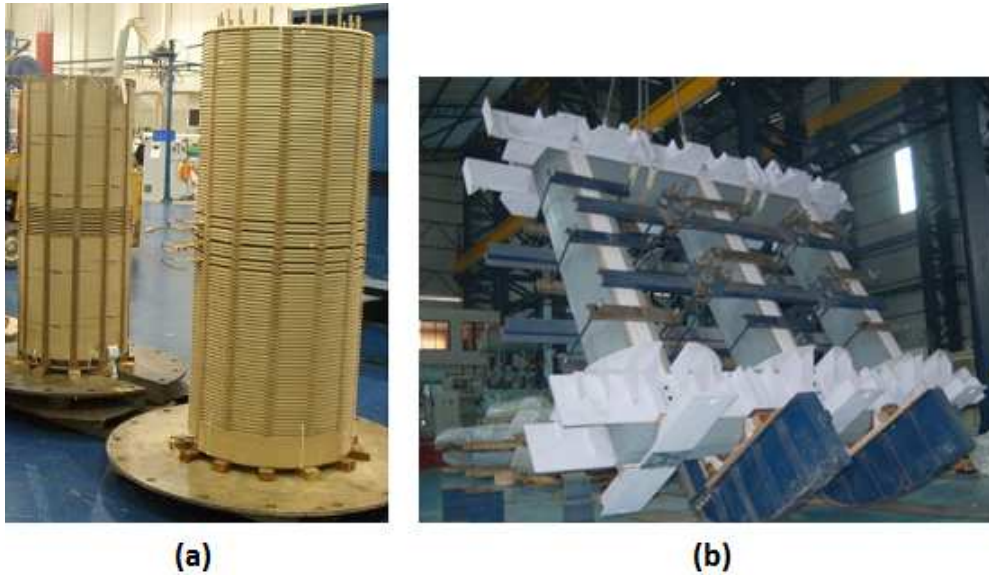


Figure 1.2: (a) Power transformer windings [5]. (b) Power transformer core assembly [4].

and mechanical strength. Between the conductor layers, there are axial and radial cooling ducts where the transformer oil can flow in order to reduce the temperature gradient between winding conductors and surrounding oil, such that the hot spot temperature is kept to a minimum. This reduces the rate of degradation of the winding insulation due to hot spots and consequently ensures a longer life expectancy of a power transformer. Typical power transformer windings are shown in Fig. 1.2(a).

Iron core

The iron core is manufactured using very thin (e.g. 0,23 mm) [4] laser etched grain-oriented low loss steel laminations and rigid core clamps. The core clamps reduce vibrations and noise level. In power transformer iron cores, cooling ducts between lamination sections are provided in order to facilitate efficient circulation of transformer oil and keep the iron core temperature within the required limit. The iron core laminations are also insulated in order to reduce the eddy currents and minimize the iron core losses. The iron core yokes are clamped with solid mild steel plates to ensure the ability to withstand mechanical deformations during transportation and short circuits. A typical power transformer iron core assembly is shown in Fig. 1.2(b).

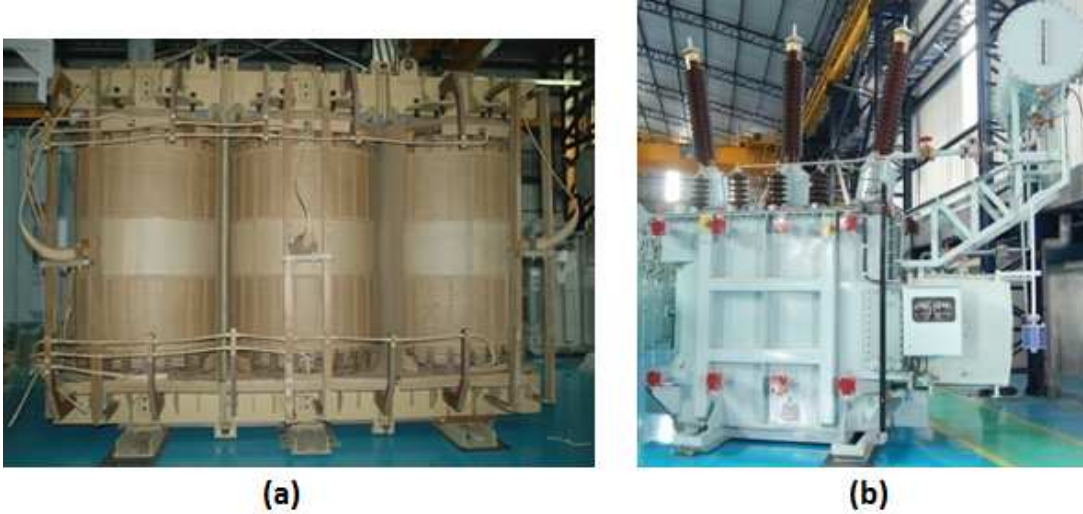


Figure 1.3: (a) Power transformer active part assembly [4]. (b) Power transformer final assembly with transformer tank and accessories [4].

Active part assembly and connections

The low voltage windings are generally mounted near the iron core over the insulating cylinder and oil ducts. High voltage windings are in such a case mounted coaxially and placed outside the low voltage windings [4]. Pressboard spacers between coils are shaped for maximum firmness. The coils are assembled with high quality insulating materials and are firmly clamped. The cleats and leads of both windings are connected by extra flexible insulated copper cables rigidly braced in position. A typical power transformer active part assembly is shown in Fig. 1.3(a).

Transformer tank

The transformer tank stores the transformer insulation oil and protects the active part of the power transformer [4]. Transformer tanks are manufactured by welding suitable parts of low carbon steel sheets. The tanks are manufactured such that they can withstand vacuum and pressure tests according to the requirements. Robust skids under the active part are provided and guide bars are located inside the tank to securely fix the active part assembly in order to prevent any movements during the transportation and on-site handling. A typical power transformer tank can be seen in Fig. 1.3(b).

Final assembly and accessories

The finalized transformer includes the active part, transformer tank and a number of standard accessories which include e.g. bushings with accessories, cooling equipment (radiators and/or heat exchangers with oil/water circulating pumps), conservator tank, magnetic oil level gauge, winding temperature indicator, double-float Buchholz relay, pressure relief valve, disconnecting chambers for cable boxes, flow indicators with differential gauges, silica gel breathers etc [4]. A typical power transformer final assembly is shown in Fig. 1.3(b).

1.3 Radial winding deformations

Radial winding deformations of transformers are generally caused by the mechanical forces from short circuit currents, although some radial deformations may be a result of original manufacturing errors. It is equally important to detect both types of radial deformations, since small manufacturing deviations may represent weak spots particularly sensitive to mechanical forces from short circuit currents that occur during the lifetime of a power transformer. In this section, a short theoretical analysis of the radial forces acting on transformer windings due to short circuit currents will be presented. A graphical summary of the various mechanical forces acting on power transformer windings and the potential consequences of these forces in terms of radial winding deformations [5], is shown in Fig. 1.4.

For an easy understanding of the transformer in operation it is convenient to use the ampere-turn diagram [6], as shown in Fig. 1.5(a). The figure shows the cross section of the winding structure where the inner (normally low-voltage) winding has N_1 turns and carries the current I_1 and the outer (normally high-voltage) winding has N_2 turns and carries the current I_2 . The trapezoidal area diagram in Fig. 1.5(a) represents the surface integral of the current density in the direction of the radial axis (here denoted by r). From Fig. 1.5(a), it is seen that the current density in the inner winding of height h and thickness t_1 is equal to $J_1 = (N_1 I_1)/(h t_1)$. The corresponding current density in the outer winding of height h and thickness t_2 is equal to $J_2 = -(N_2 I_2)/(h t_2) = -(N_1 I_1)/(h t_2)$, since by (1.1) one has $N_1 I_1 = N_2 I_2$. For the inner winding, the Ampere law in integral form can be used

$$\oint_C \mathbf{H} \cdot d\mathbf{l} = \int_A \mathbf{J} \cdot \mathbf{n} dA \quad , \quad (1.2)$$

where it is noted that the magnetic field strength \mathbf{H} is assumed to be zero everywhere along the contour C , except for the part of length h within the winding, where it is constant due to symmetry. Furthermore, one notes that the current density J_1 defined above is constant on the area A . Thus one obtains from (1.2)

$$H h = \frac{N_1 I_1}{h t_1} h \int_0^r dr \quad \Rightarrow \quad H = H_0 \frac{r}{t_1} \quad , \quad H_0 = \frac{N_1 I_1}{h} = \frac{N_2 I_2}{h} \quad . \quad (1.3)$$

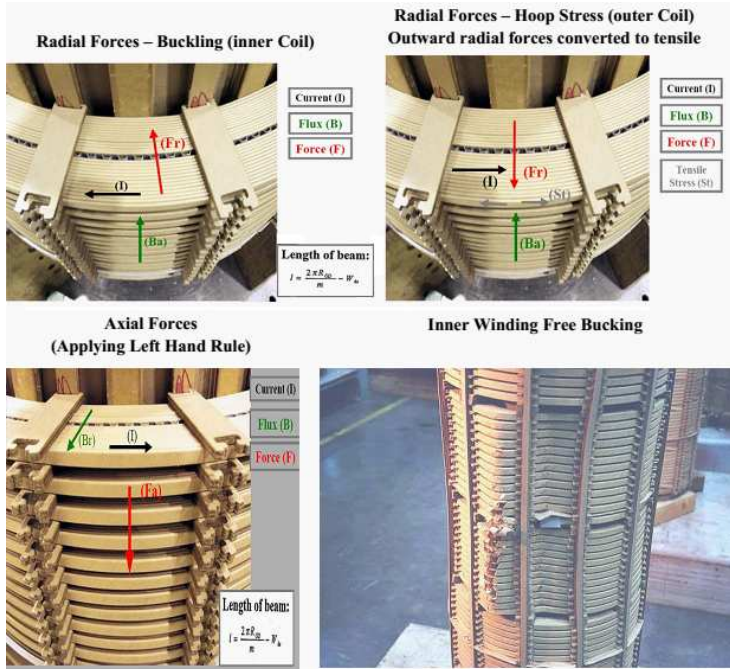


Figure 1.4: Summary of mechanical forces [5].

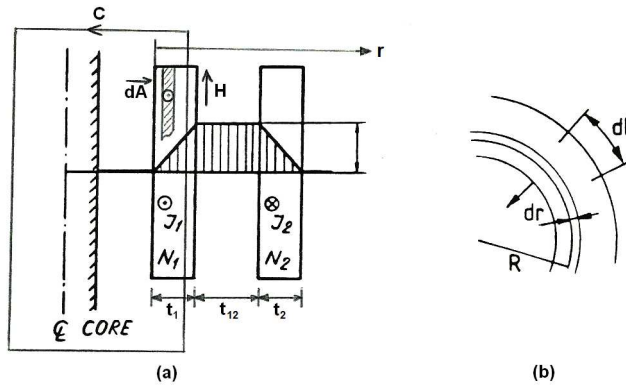


Figure 1.5: Cross sections of the winding structure [6].

In the duct between the inner and outer winding, the Ampere law gives simply

$$H h = N_1 I_1 \quad \Rightarrow \quad H = H_0 = \frac{N_1 I_1}{h} = \frac{N_2 I_2}{h} \quad . \quad (1.4)$$

Finally, for the outer winding, the Ampere law gives

$$H h = N_1 I_1 - \frac{N_2 I_2}{h t_2} h \int_{t_1+t_{12}}^r dr \quad \Rightarrow \quad H = H_0 \left(1 - \frac{r - t_1 - t_{12}}{t_2} \right) \quad , \quad (1.5)$$

where t_{12} is the thickness of the duct between the two windings. Thus in this idealized model, the ampere-turn value starts from zero at $r = 0$ (inner boundary of the inner winding). Along the inner winding it linearly rises to the value of H_0 at the outer boundary of the inner winding. It then maintains a constant value H_0 along the duct between the two windings. Finally, along the outer winding, the ampere-turn value linearly decreases to zero. Thus the trapezoidal shape of the ampere-turn diagram as anticipated in Fig. 1.5(a) is mathematically verified. The ampere-turn diagram obtained using results (1.3)-(1.5) will be useful in studying the mechanical forces that cause the radial deformations of transformer windings.

In this case, mechanical forces are results of electromagnetic interaction between two or more conductors that carry electric current. As both inner and outer windings of a power transformer in normal operation carry relatively large electric currents, the transformer windings are subject to both radial and axial mechanical forces during their entire lifecycle [5]. However, power transformers are designed in such a way that they can withstand the mechanical forces due to normal operation conditions practically indefinitely. Thus, in steady state conditions, mechanical deformations of transformer windings are highly unlikely. However, when a transformer is subject to transient phenomena, much higher transient currents can flow through the windings during a short period of time. The highest currents through the transformer windings normally appear in a short circuit condition, i.e. when one side of the transformer (usually the high-voltage side) is energized while the other side of the transformer (usually the low-voltage side) is short-circuited.

The calculation of the short circuit currents in power transformers is based on a simple circuit model, where the feeding network is modeled as an ideal voltage source behind a linear impedance while a transformer is represented by a short-circuit impedance [6]. A straightforward transient analysis of such a simple model, when the voltage is switched on, shows that the theoretical maximum of the first peak of the transient current is equal to $2\sqrt{2} \approx 2,82$ times the steady-state root-mean-square value of the current. This value is based on the assumption that there is zero resistance in the circuit. In a more realistic model, with resistances taken into account, this short-circuit factor is reduced. For example, the IEC 60076-5:2000(E) standard stipulates the maximum value of 2,55 [7].

The mechanical forces due to the electromagnetic interaction between two conductors are generally proportional to the product of their currents. In view of the

relation (1.1), for power transformer windings interacting with each other, the radial mechanical forces are therefore proportional to the square of the short-circuit current. Now, as the short-circuit current can be up to 2,55 times higher than the corresponding current in normal operation, this means that the short-circuit mechanical forces can be up to $2,55^2 = 6,5$ times larger than the normal operation mechanical forces. Such forces, in particular if they are frequently applied, can be potentially damaging and give rise to radial winding deformations. In order to derive a suitable formula for the dimensioning radial forces, let us consider the outer winding with the following data

t_2 - Winding width

R - Winding mean radius

N_2 - Number of turns

I_2 - Winding current

A_C - Conductor wire cross-section area

ρ - Conductor material (copper) density

As shown in (1.5), the magnetic field strength H and consequently the magnetic induction $B = \mu_0 H$ decreases linearly from a maximum value B_0 to zero along the winding

$$B = B_0 \left(1 - \frac{r - t_1 - t_{12}}{t_2} \right) = B_0 \left(1 - \frac{t}{t_2} \right) \quad , \quad (1.6)$$

where a new radial variable $t = r - t_1 - t_{12}$ is introduced and

$$B_0 = \mu_0 \frac{N_2 I_2}{h} \quad . \quad (1.7)$$

On the other hand, each infinitesimal segment of the radial cross section of the winding with area $dA = dr dz$, where dr is an infinitesimal element in the radial direction and dz is an infinitesimal element in the axial direction, carries the current

$$dI = \frac{N_2 I_2}{h t_2} dA = \frac{N_2 I_2}{h t_2} dt dz \quad . \quad (1.8)$$

The radial force on an infinitesimal element of winding conductor wire of circumferential length dl , as indicated in Fig. 1.5(b), is then given by $\mathbf{F} = I d\mathbf{l} \times \mathbf{B}$, i.e.

$$dF = B dI dl = \mu_0 \frac{N_2 I_2}{h} \left(1 - \frac{t}{t_2} \right) \frac{N_2 I_2}{h t_2} dt dz dl \quad . \quad (1.9)$$

Integrating this force element over $0 < t < t_2$ and $0 < z < h$, one obtains

$$\frac{dF}{dl} = \mu_0 \frac{(N_2 I_2)^2}{h} \int_0^{t_2} \left(1 - \frac{t}{t_2} \right) \frac{dt}{t_2} \int_0^h \frac{dz}{h} = \mu_0 \frac{(N_2 I_2)^2}{2h} \quad . \quad (1.10)$$

The tensile force on the wires of the winding of mean radius R , due to radial forces along the winding circumference, is then obtained using the formula

$$F = 2R \frac{dF}{dl} = \mu_0 \frac{R}{h} (N_2 I_2)^2 \quad (\text{N}) \quad . \quad (1.11)$$

For practical design of power transformers, it is common to use the radial mechanical stress in the conductor material rather than the actual radial mechanical force. With the notation above, the mechanical stress in the winding conductor is defined by the tensile force (1.11) divided by the total conductor area in the radial cross section of the winding $N_2 A_C$, i.e.

$$\sigma = \frac{F}{N_2 A_C} = \frac{\mu_0 R N_2 I_2^2}{h A_C} \quad . \quad (1.12)$$

Introducing now the total conductor mass in the winding and short-circuit conductor current density by

$$G = \rho N_2 A_C 2\pi R \quad , \quad J_{max} = k J_k = \frac{I_2}{A_C} \quad , \quad (1.13)$$

one can rewrite (1.12) as follows

$$\sigma = \frac{\mu_0}{2\pi\rho} \frac{\rho N_2 A_C 2\pi R}{h} \left(\frac{I_2}{A_C} \right)^2 = \frac{\mu_0 k^2}{2\pi\rho} \frac{G}{h} J_k^2 \quad (\text{N/m}^2) \quad , \quad (1.14)$$

where typically $k = 2,55$ and $\rho = 8,9 \times 10^3 \text{ kg/m}^3$ for copper. Using the result (1.14), it is possible to calculate the short-circuit mechanical stress in the conductor material. On the other hand, the typical value of the tensile strength of power transformer winding copper wires is between $2,0 \times 10^8 \text{ N/m}^2$ and $2,5 \times 10^8 \text{ N/m}^2$. At some extreme short-circuit conditions, such values of radial forces may be reached, in which case severe radial winding deformations can occur.

1.4 Transformer diagnostic methods

There are several diagnostic methods for power transformers currently available on the market. A short review of these diagnostic methods will be presented below.

Existing on-line methods

One frequently used on-line method to detect insulation degradation is Dissolved Gas in oil Analysis (DGA), where one takes a sample of the oil and measures the amount of dissolved gases (H_2 , CO_2 , C_2H_2 , etc). The absolute concentrations as

well as the ratios between concentrations of some of these gases, are then used for identification of potentially on-going faults. Oil samples are usually taken manually from a tap and sent to a chemical laboratory. Some transformer manufacturers offer real-time on-line monitoring equipment for DGA as well [8].

The main disadvantage of the DGA methods is their low predictive ability. For example, high concentrations of C_2H_2 in combination of unfavorable ratios of concentrations of some other hydrocarbons are generally considered as a clear indicator of an on-going fault. However, the various schemes used to evaluate the state of the insulation based on DGA generally do not provide sufficient information to a grid owner how advanced the fault is or what the probable cause of the fault is. Thus it is difficult to make a reasonable prediction of the remaining lifetime of the transformer based on the DGA analysis. Since purchasing a new replacement transformer is a major investment, grid owners are generally reluctant to make such a decision based on predictions provided by DGA.

Another on-line diagnostic method for power transformers is the so-called Partial Discharge (PD) method. The PD method is applied on-line using an external measurement equipment. The sparks from induced partial discharges emit electromagnetic waves over a broad frequency range together with pressure waves that can be detected with acoustical techniques [9]. The detection of partial discharges is usually done by placing inductive and capacitive sensors around conductors and connecting them to capacitive foils in the bushing field-grading [10], [11]. For localization purposes it is customary to use acoustic triangulation by mounting pressure sensors outside the tank [12]. Recently, a study of detection of partial discharges using ultra-high frequency (UHF) triangulation was proposed in [13]. The main disadvantage of the PD method is the fact that, while connected to the power grid, the safe operation of a power transformer does not allow the PD-test voltage to be controlled and there is no possibility to perform any overvoltage testing.

As far as the present author is aware, methods that offer on-line monitoring of possible winding deformations due to the mechanical forces from short circuit currents are generally not available.

Existing off-line methods

Frequency response analysis (FRA) is a frequency-domain method which is used to detect mechanical winding deformations due to high short circuit currents in combination with the weakening of the cellulose based pressboard spacers. The FRA method is applied off-line [14]. The material properties and geometry of a transformer determines its frequency response, and can be considered as the transformer's fingerprint [15]. If mechanical changes occur, for example when the windings are distorted, the frequency response/fingerprint of a transformer will be changed. The usual upper frequency limit for FRA is around 2 MHz.

Studies of some typical mechanical deformations of winding segments using FRA are found in [16] and [17]. For FRA to be a reliable diagnostic method, it is beneficial to make a reference measurement when the transformer is newly manufactured or

well before there are indications of any mechanical deformations, or to make a comparison with a measurement on a sister unit (i.e. a transformer of the same type). However, the interpretation of FRA measurement results is not standardized.

In order to enhance the understanding of the information contained in FRA measurements, two strategies were proposed in [15]: (1) extending the upper frequency limit of the FRA method by an order of magnitude, in order to detect and interpret new phenomena that occur at high frequencies and investigate the potential of this high-frequency region for detection of winding deteriorations, and (2) combining the FRA method with Time Domain Reflectometry (TDR), so that FRA measurements are visualized in the time domain, in order to get a more intuitive detection and localization of faults.

Dielectric spectroscopy can be used to monitor the dielectric properties of cellulose based solid insulation (paper, pressboard etc.) and transformer oil [18]. In this method, it is common to apply a relatively low-voltage signal (below 200 V) between two windings, or between a winding and the iron core or transformer tank wall. The small current flowing through the insulation is measured as a function of frequency in the range between 0,1 mHz and up to the order of 1 kHz. The moisture effects are most notable in the sub-Hz region, where the dissociative strength of the moisture can create quasi free charge carriers visible by means of a low frequency dispersion (LFD) process. When the frequency approaches the microwave frequencies, the dipolar nature of moisture water becomes significant and contributes to an increase of dielectric losses in the paper insulation. The main disadvantage of all the off-line methods is that they require disconnection from the grid, generally implying a non-service stress of the transformer [2], [19], [20].

1.5 Models for wave propagation analysis

Typically, power transformers operate at frequencies of 50 Hz or 60 Hz, depending on the geographical region [21]. For such low frequencies, the overall length of the winding is short compared to the typical wavelengths in the surrounding media. Thus, a power transformer winding can be modelled by a small number of lumped circuit elements. The magnetic field distribution in the iron core, on the other hand, requires a more detailed model. Furthermore, the analysis of fast transients in a power transformer winding requires models that are used at considerably higher frequencies than the abovementioned operational frequencies.

For frequencies below 1 MHz, lumped network models of a power transformer winding can be used. In these models, each turn of a power transformer winding is approximated by a set of lumped circuit elements which describe interactions within the turn itself, interactions with adjacent turns, as well as interactions with the iron core/transformer tank wall [22].

For frequencies above 1 MHz, more complex network models are needed but they are on the other hand less attractive from the computational point of view. The network models are therefore generally replaced by multi-conductor transmission

line (MTL) models [23]. In MTL models, the winding turns are treated as parallel conductors, connected in series at the endpoints, and the winding is described by distributed impedance and admittance MTL-matrices.

In the analysis of very fast transients, MTL models are used for frequencies up to about 5 MHz [24]. However, provided that the axial winding dimensions are not too large, the MTL model is potentially useful even for somewhat higher frequencies. However, as far as the present author is aware, the survey of the available literature shows that no systematic studies of wave propagation in power transformers have been reported for frequencies in the range 10 MHz - 100 MHz, i.e. just below the lower microwave region.

One study of transformer diagnosis using microwave radiation is a numerical study in [25]. In this study, a radar antenna, operating at 9,5 GHz and located in the wall of the tank, has been used to detect axial displacements of the winding. This study is very generic and the winding is modeled as a solid piece of metal, such that some new aspects that must be considered at such high frequencies are not taken into account.

1.6 Aim of the present thesis

In view of the above descriptions of existing diagnostic methods, as well as on the discussion of their strengths and weaknesses, the aim of the present thesis is to propose and study a new on-line diagnostic method with a potential to detect the effects of various deterioration processes in power transformers in a more accurate way, with less risks of adverse consequences of the measurement process, for the normal operation.

The idea behind the on-line diagnostic method proposed in the present thesis is to insert antennas inside the transformer tank, above and below the transformer windings, to radiate and measure microwave fields that interact with the winding structure. The microwave radiation (up to a few GHz) has wavelengths comparable to the distances between the winding segments in realistic power transformers, which makes it suitable for detection of various deformations of the winding structure including radial displacements, elliptic deformations, eccentric shifts etc. The analysis of the measured microwave signals and their relations to the structure parameters, being the signatures of mechanical deformations, is an inverse electromagnetic problem [26].

Here, the propagation problem is solved by conventional waveguide theory, including mode-matching and cascading techniques [27]. Optimization is used to solve the inverse problem in order to reconstruct the actual positions of the displaced winding segments. The proposed method is intended to complement the existing methods described in Section 1.4, especially since it can be used on-line for "silent" problems that do not cause partial discharges.

The main advantage of the diagnostic method proposed here, is that it is an on-line method that does not require the disconnection of a monitored power trans-

former from the electric power grid, thus avoiding the non-service stress of the transformer. On the other hand, compared to the existing on-line methods like e.g. the PD method, the proposed method does not require connection of the test voltages to the actual primary or secondary terminals (bushings) of the monitored power transformer. In other words, the test signals (high-frequency microwave radiation) are completely independent on any low-frequency signals applied to the windings of the monitored power transformer in the course of its regular operation. Furthermore, the diagnostic method proposed in the present thesis, unlike e.g. the DGA methods, is not an integral method and it actually gives a snapshot of the present state of the power transformer. Thus it can be used to detect the actual winding deformations measured in suitable length units (e.g. mm) at the very instant when the measurement is performed.

1.7 Thesis disposition

After an introduction and an overview of the power transformer fundamentals, with a short summary of the existing diagnostic methods, in Chapter 1, the simplest power transformer model - the parallel-plate model - is studied in Chapter 2. This model is used in Paper I. Then in Chapter 3, the approximate cylindrical model of the transformer, used in Paper II, is studied. Thereafter, in Chapter 4, the perturbation approach to the approximate cylindrical model, for the special case of the elliptic mechanical deformations, is studied. This model is used in Paper III. In Chapter 5 the exact cylindrical model used in Paper IV, with solutions for the electromagnetic fields in terms of Bessel-functions, is studied. In Chapter 6, the optimization results for the inverse problems, based on the theoretical considerations described in Chapters 2 - 5, are presented and discussed. Finally in Chapter 7, the conclusions and proposals for future work are discussed.

Chapter 2

Parallel-plate model

2.1 Transformer model description

From the descriptions in the previous chapter, it is seen that the iron core and the winding package (mutually coaxial low voltage winding and high voltage winding with insulation) have a cylindrical shape. The transformer tank on the other hand, is usually of an irregular shape and can not be described as any simple waveguide boundary. This applies particularly to three-phase power transformers as the one with assembly depicted in Fig. 1.3(b).

As a simplest possible waveguide model of a large three-phase power transformer, an angular segment of the transformer active part shown in the left-hand part of Fig. 2.1 can be considered. Under some geometrical conditions, which will be discussed in more detail in Chapter 3, this angular segment of the transformer active part can be described as a planar structure, shown in the right-hand part of Fig. 2.1, resembling a two-dimensional parallel plate waveguide.

The electromagnetic theory of a direct problem for a two-dimensional parallel plate waveguide model is used as a theoretical basis for the study presented in Paper I.

Thus, as the simplest first step, the model of a transformer as a two-dimensional parallel plate waveguide is chosen where one plate represents the wall of the transformer tank and the other plate represents the iron core that conducts the magnetic flux. In between there is a set of parallel conductors representing the segments of the winding package. Then it is assumed that suitable antennas are inserted inside the transformer tank, above and below the winding package, to radiate and measure microwave fields that interact with the winding conductors, as shown in Fig. 2.2. Before starting the analysis of such a structure, a review of the waveguide theory applied to the propagation of transverse magnetic (TM) waves in a two-dimensional parallel plate waveguide is given. A more detailed review of general waveguide theory can be found in Appendix 1.

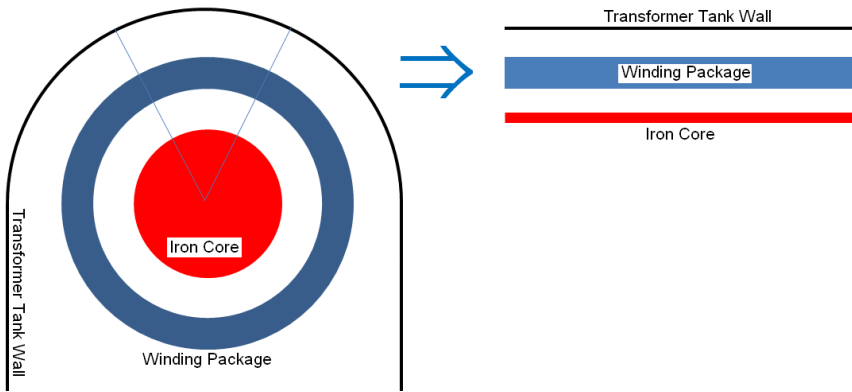


Figure 2.1: Angular segment of an active part of a power transformer, described as a two-dimensional parallel plate waveguide.

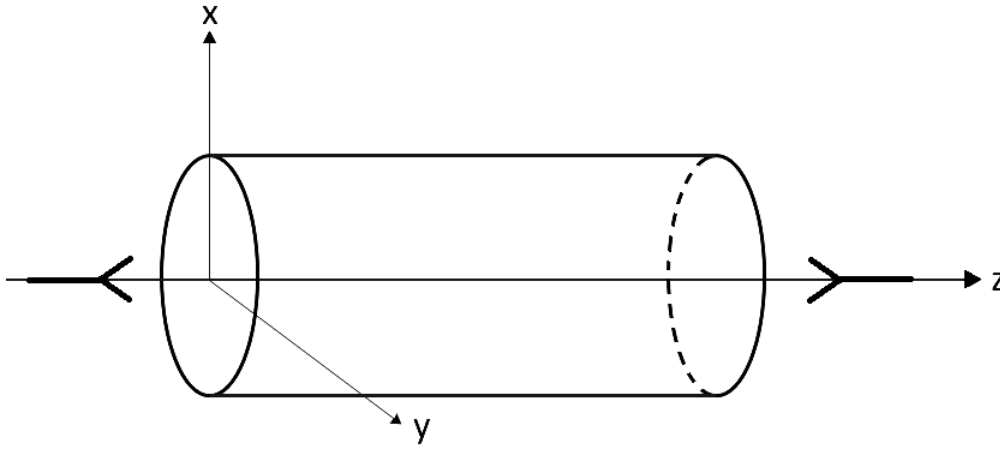


Figure 2.2: An example of a circular waveguide in the z -direction with antennas emitting waves on both sides of the structure.

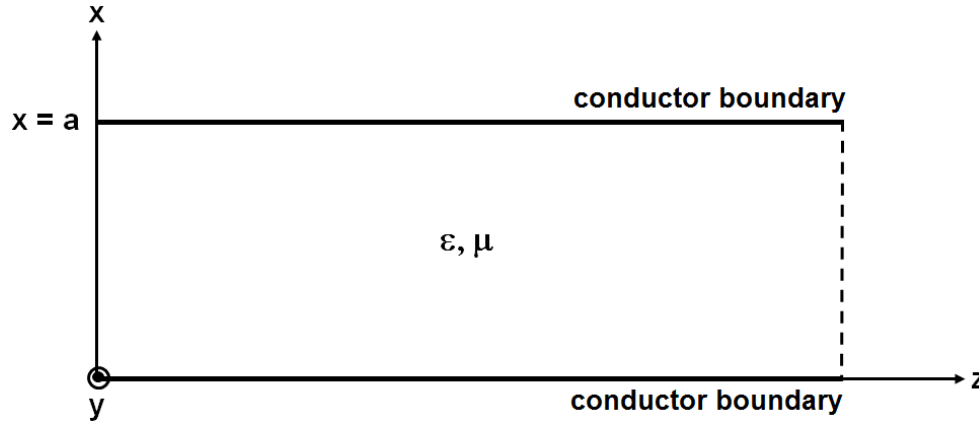


Figure 2.3: An example of a parallel-plate waveguide.

2.2 Parallel-plate waveguides

TM waves ($H_z = 0$) between parallel plates

Consider two conducting planes separated by a dielectric medium with constitutive parameters ϵ and μ , as shown in Fig. 2.3 [28]. Throughout the thesis, sinusoidal time dependence ($e^{j\omega t}$) and no sources of the field inside the waveguide ($\rho = 0$ and $\mathbf{J} = 0$) will be assumed. Due to the symmetry of the problem in Fig. 2.3, the transverse dependence of the longitudinal electric field E_z is only a function of x and not a function of y . Thus one obtains, using equation (A.14) from Appendix 1 for the longitudinal component of the electric field

$$\frac{d^2 E_z}{dx^2} + k_T^2 E_z = 0 \quad . \quad (2.1)$$

For TM waves, the boundary conditions, defined by (A.40) in Appendix 1, are

$$E_z(0) = 0 \quad , \quad E_z(a) = 0 \quad . \quad (2.2)$$

With these boundary conditions, the solution for the longitudinal field becomes

$$E_z(x) = E_0 \sin\left(\frac{n\pi x}{a}\right) \quad , \quad k_{Tn} = \frac{n\pi}{a} \quad , \quad n = 1, 2, 3 \dots \quad . \quad (2.3)$$

The transverse fields are then given by

$$\mathbf{E}_T = \pm \frac{jk_z}{k_{Tn}^2} \nabla_T E_z = \pm \frac{jk_z}{k_{Tn}^2} \left(\frac{\partial E_z}{\partial x} \mathbf{e}_x + \frac{\partial E_z}{\partial y} \mathbf{e}_y \right) \quad , \quad (2.4)$$

or

$$E_x = \pm \frac{j k_z}{k_{Tn}^2} \frac{dE_z}{dx} = \pm \frac{j k_z}{\left(\frac{n\pi}{a}\right)^2} \cdot \left(\frac{n\pi}{a}\right) E_0 \cos\left(\frac{n\pi x}{a}\right) \quad , \quad (2.5)$$

$$E_y = 0 \quad , \quad (2.6)$$

and

$$\mathbf{H}_T = \frac{-j\omega\epsilon}{k_{Tn}^2} \mathbf{e}_z \times \nabla_T E_z = \frac{-j\omega\epsilon}{k_{Tn}^2} \mathbf{e}_z \times \left(\frac{\partial E_z}{\partial x} \mathbf{e}_x + \frac{\partial E_z}{\partial y} \mathbf{e}_y \right) \quad . \quad (2.7)$$

Using now $\mathbf{e}_z \times \mathbf{e}_x = \mathbf{e}_y$ and $\mathbf{e}_z \times \mathbf{e}_y = -\mathbf{e}_x$, one obtains

$$\mathbf{H}_T = \frac{-j\omega\epsilon}{k_{Tn}^2} \left(-\frac{\partial E_z}{\partial y} \mathbf{e}_x + \frac{\partial E_z}{\partial x} \mathbf{e}_y \right) \quad , \quad (2.8)$$

or

$$H_x = 0 \quad , \quad (2.9)$$

$$H_y = \frac{-j\omega\epsilon}{k_{Tn}^2} \frac{dE_z}{dx} = \frac{-j\omega\epsilon}{\left(\frac{n\pi}{a}\right)^2} \cdot \left(\frac{n\pi}{a}\right) E_0 \cos\left(\frac{n\pi x}{a}\right) \quad . \quad (2.10)$$

Using (A.53), it is seen that the TM waves can only propagate for operating angular frequencies higher than the cutoff angular frequency

$$\frac{\omega}{c} > \frac{\omega_{cn}}{c} = k_{Tn} = \frac{n\pi}{a} \quad , \quad n = 1, 2, 3 \dots \quad . \quad (2.11)$$

The result (2.3) requires $n > 0$ in order to obtain a non-trivial solution. However, from (2.3), (2.5) and (2.10) it is seen that a TM_0 mode, i.e. a TM mode with $n = 0$, can also exist in the parallel-plate waveguide. For $n = 0$, $E_z = 0$ and only the transverse components of the fields E_x and H_y exist. Using $k_T = 0$ in (A.14)-(A.15), one obtains

$$\nabla_T E_x = \frac{d^2 E_x}{dx^2} = 0 \quad , \quad \nabla_T H_y = \frac{d^2 H_y}{dx^2} = 0 \quad . \quad (2.12)$$

The solutions of these equations, for a parallel-plate waveguide, are of the form

$$\mathbf{E}_T(x, y) = E_0 \mathbf{e}_x \quad , \quad \mathbf{H}_T(x, y) = \mp \frac{1}{Z} \mathbf{e}_z \times \mathbf{E}_T = H_0 \mathbf{e}_y \quad , \quad (2.13)$$

where $H_0 = \mp E_0/Z$. Hence, the TM_0 mode is the TEM mode, for which the cutoff angular frequency is zero ($\omega_{cn} = 0$) and it propagates at all frequencies. The mode having the lowest cutoff frequency is called the dominant mode, such that for the parallel-plate waveguide, the dominant TM mode is the TEM-mode.

For $n \neq 0$, the fields are of the form

$$E_x = \pm \frac{j k_z a}{n\pi} E_0 \cos\left(\frac{n\pi x}{a}\right) \quad , \quad (2.14)$$

$$H_y = \frac{-j\omega\epsilon a}{n\pi} E_0 \cos\left(\frac{n\pi x}{a}\right) \quad . \quad (2.15)$$

These fields satisfy the general relations (A.46). From (2.14) and (2.15), the appropriate basis function for this TM_n mode is thus of the form

$$\psi_n = A_n \cos\left(\frac{n\pi x}{a}\right) \quad . \quad (2.16)$$

Defining now an inner product of the basis functions

$$\langle \psi_n | \psi_m \rangle = \int_0^a \psi_n(x) \psi_m(x) dx \quad . \quad (2.17)$$

the basis functions (2.16) can be normalized as follows

$$\langle \psi_n | \psi_m \rangle = \delta_{nm} \quad . \quad (2.18)$$

For $n \neq m$, this is obviously zero, due to the properties of cosine functions. For $n = m$, one has

$$\langle \psi_n | \psi_n \rangle = \int_0^a [\psi_n(x)]^2 dx = 1 \quad , \quad (2.19)$$

which gives

$$A_n = \left[\int_0^a \cos^2\left(\frac{n\pi x}{a}\right) dx \right]^{-1/2} \quad . \quad (2.20)$$

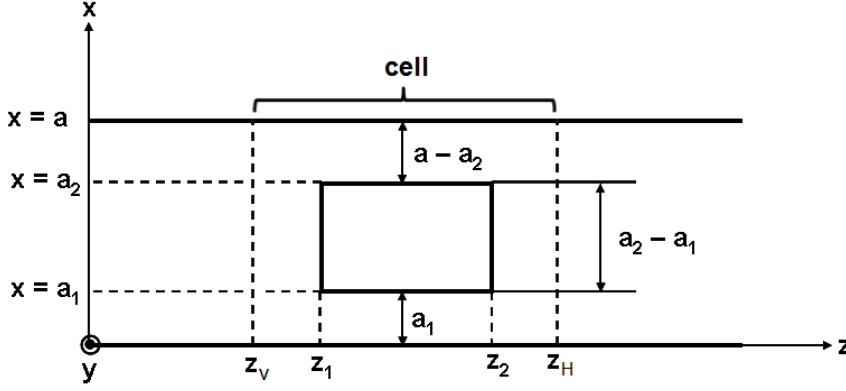


Figure 2.4: Two-dimensional model of a rectangular winding.

The results for A_n for $n = 0$ and $n \geq 1$ can be summarized as

$$A_n = \sqrt{\frac{2 - \delta_{n,0}}{a}} = \begin{cases} \sqrt{\frac{1}{a}} & , \quad n = 0 \\ \sqrt{\frac{2}{a}} & , \quad n \geq 1 \end{cases} . \quad (2.21)$$

Thus the basis functions are

$$\psi_n = \sqrt{\frac{2 - \delta_{n,0}}{a}} \cos\left(\frac{n\pi x}{a}\right) , \quad (2.22)$$

for TM_n modes.

2.3 Mode-matching analysis of TM waves

Consider a TM wave traveling in the z -direction between the two parallel plates with a rectangular conductive obstacle, as shown in Fig. 2.4. The region between the plates is assumed to be filled with a lossless medium. For the propagation problem, only TM modes ($H_z = 0$) are considered, as they include the dominant TEM mode which propagates at all frequencies. The four relevant regions between the plates and the conductive obstacle are denoted as in Fig. 2.5. The basis functions in the four regions above are then given by

$$\psi_n^{(1)}(x) = \sqrt{\frac{2 - \delta_{n,0}}{a_1}} \cos\left(\frac{n\pi x}{a_1}\right) , \quad (2.23)$$

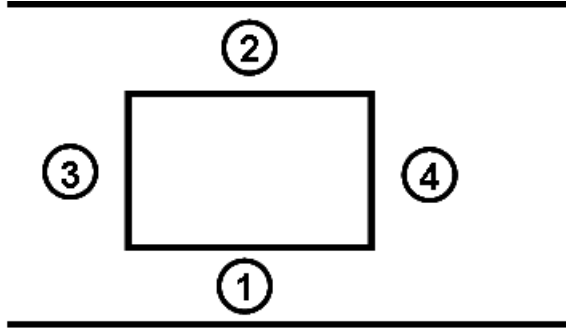


Figure 2.5: The four regions in the two-dimensional model of a rectangular winding.

$$\psi_n^{(2)}(x) = \sqrt{\frac{2 - \delta_{n,0}}{a_2}} \cos \left[\frac{n\pi}{a_2} (a - x) \right] \quad , \quad (2.24)$$

and with no obstacle present in the regions 3 and 4,

$$\psi_n^{(3)}(x) = \psi_n^{(4)}(x) = \sqrt{\frac{2 - \delta_{n,0}}{a}} \cos \left(\frac{n\pi x}{a} \right) \quad . \quad (2.25)$$

Let us now use the definition of the wave number k_{Tn} , i.e.

$$k_{Tn}^2 = \omega^2 \mu \epsilon - k_{zn}^2 \quad , \quad (2.26)$$

where the longitudinal wave number for the n -th mode is denoted by k_{zn} , and the usual notation $k^2 = \omega^2 \mu \epsilon$ is used. Thus the longitudinal wave number is obtained as

$$k_{zn}^{(i)2} = \omega^2 \mu \epsilon - k_{Tn}^2 = k^2 - \left(\frac{n\pi}{a_i} \right)^2 \quad , \quad (2.27)$$

The TM_n -mode impedance is given by the general formula

$$Z = \frac{k_z}{k} \sqrt{\frac{\mu}{\epsilon}} = \frac{k_z}{k} \eta \quad , \quad \eta = \sqrt{\frac{\mu}{\epsilon}} \quad , \quad (2.28)$$

such that for the four different regions, the impedance becomes

$$Z_n^{(i)} = \frac{k_{zn}^{(i)}}{k} \eta \quad , \quad i = 1, 2, 3, 4 \quad , \quad (2.29)$$

The transverse electric and magnetic fields are now linear combinations of the basis functions $\psi_n^{(i)}(x)$ for the respective region. Let us now recall the general result

$$E_x = \mp Z H_y \quad . \quad (2.30)$$

For waves propagating in the positive z -direction ($e^{-jk_z z}$), the lower sign is used, such that

$$E_x = +Z H_y \quad \Rightarrow \quad E_{xn}^{(i)} = Z_n^{(i)} H_{yn}^{(i)} \quad , \quad (2.31)$$

for each mode and each region. The transverse fields can then be expanded, in terms of the basis functions, in the following series

$$E_x^{(i)}(x, z) = E^{(i)}(x, z) = \sum_{n=0}^{\infty} \left[c_n^{(i)+}(z) + c_n^{(i)-}(z) \right] Z_n^{(i)} \psi_n^{(i)}(x) \quad , \quad (2.32)$$

$$H_y^{(i)}(x, z) = H^{(i)}(x, z) = \sum_{n=0}^{\infty} \left[c_n^{(i)+}(z) - c_n^{(i)-}(z) \right] \psi_n^{(i)}(x) \quad , \quad (2.33)$$

where it is seen that the condition (2.30) is satisfied individually for each mode and each region. Now the boundary conditions at the planes $z = z_1$ and $z = z_2$ need to be considered. The electric field $\mathbf{E} = E_x \mathbf{e}_x$ is tangential to the plane $z = z_1$, and the boundary conditions in the plane $z = z_1$ indicate that the electric field is continuous over that boundary, i.e.

$$E_t(z_1-) = E_t(z_1+) \quad \Rightarrow \quad E(z_1-) = E(z_1+) \quad . \quad (2.34)$$

Since $E = 0$ inside the conductive material of the obstacle, the electric field E vanishes at the metallic part of the boundary. Thus one can write

$$\begin{aligned} & \sum_{n=0}^{\infty} \left[c_n^{(3)+}(z_1) + c_n^{(3)-}(z_1) \right] Z_n^{(3)} \psi_n^{(3)}(x) = \\ & = \begin{cases} \sum_{n=0}^{\infty} \left[c_n^{(1)+}(z_1) + c_n^{(1)-}(z_1) \right] Z_n^{(1)} \psi_n^{(1)}(x) & , \quad 0 < x < a_1 \\ 0 & , \quad a_1 < x < a - a_2 \\ \sum_{n=0}^{\infty} \left[c_n^{(2)+}(z_1) + c_n^{(2)-}(z_1) \right] Z_n^{(2)} \psi_n^{(2)}(x) & , \quad a - a_2 < x < a \end{cases} \quad (2.35) \end{aligned}$$

In addition, the magnetic field is continuous over the apertures, such that

$$\begin{aligned} & \sum_{n=0}^{\infty} \left[c_n^{(3)+}(z_1) - c_n^{(3)-}(z_1) \right] \psi_n^{(3)}(x) = \\ & = \begin{cases} \sum_{n=0}^{\infty} \left[c_n^{(1)+}(z_1) - c_n^{(1)-}(z_1) \right] \psi_n^{(1)}(x) & , \quad 0 < x < a_1 \\ \sum_{n=0}^{\infty} \left[c_n^{(2)+}(z_1) - c_n^{(2)-}(z_1) \right] \psi_n^{(2)}(x) & , \quad a - a_2 < x < a \end{cases} . \end{aligned} \quad (2.36)$$

Multiplying the boundary condition for the electric field (2.35) by $\psi_{n_3}^{(3)}(x)$, where n_3 is a specific value of the coefficient n , and integrating over the interval $0 < x < a$, one obtains

$$\begin{aligned} & \sum_{n=0}^{\infty} \left[c_n^{(3)+}(z_1) + c_n^{(3)-}(z_1) \right] Z_n^{(3)} \langle \psi_{n_3}^{(3)}(x) | \psi_n^{(3)}(x) \rangle = \\ & = \sum_{n=0}^{\infty} \left[c_n^{(3)+}(z_1) + c_n^{(3)-}(z_1) \right] Z_n^{(3)} \delta_{n_3, n} = \left[c_{n_3}^{(3)+}(z_1) + c_{n_3}^{(3)-}(z_1) \right] Z_{n_3}^{(3)} = \\ & = \sum_{n=0}^{\infty} \left[c_n^{(1)+}(z_1) + c_n^{(1)-}(z_1) \right] Z_n^{(1)} \int_0^{a_1} \psi_{n_3}^{(3)}(x) \psi_n^{(1)}(x) dx + \\ & + \sum_{n=0}^{\infty} \left[c_n^{(2)+}(z_1) + c_n^{(2)-}(z_1) \right] Z_n^{(2)} \int_{a-a_2}^a \psi_{n_3}^{(3)}(x) \psi_n^{(2)}(x) dx \quad . \end{aligned} \quad (2.37)$$

Introducing here the notation

$$\langle \psi_{n_3}^{(3)}(x) | \psi_n^{(1)}(x) \rangle_1 = \int_0^{a_1} \psi_{n_3}^{(3)}(x) \psi_n^{(1)}(x) dx \quad , \quad (2.38)$$

$$\langle \psi_{n_3}^{(3)}(x) | \psi_n^{(2)}(x) \rangle_2 = \int_{a-a_2}^a \psi_{n_3}^{(3)}(x) \psi_n^{(2)}(x) dx \quad , \quad (2.39)$$

one obtains

$$\left[c_{n_3}^{(3)+}(z_1) + c_{n_3}^{(3)-}(z_1) \right] Z_{n_3}^{(3)} = \sum_{n=0}^{\infty} \left[c_n^{(1)+}(z_1) + c_n^{(1)-}(z_1) \right] Z_n^{(1)} \langle \psi_{n_3}^{(3)}(x) | \psi_n^{(1)}(x) \rangle_1 +$$

$$+ \sum_{n=0}^{\infty} \left[c_n^{(2)+}(z_1) + c_n^{(2)-}(z_1) \right] Z_n^{(2)} \langle \psi_{n_3}^{(3)}(x) | \psi_n^{(2)}(x) \rangle_2 \quad . \quad (2.40)$$

Next by multiplying the boundary condition for the magnetic field (2.36) by $Z_{n_1}^{(1)} \psi_{n_1}^{(1)}(x)$, where n_1 is a specific value of the coefficient n , and integrating over the interval $0 < x < a_1$, one obtains

$$\begin{aligned} & \sum_{n=0}^{\infty} \left[c_n^{(3)+}(z_1) - c_n^{(3)-}(z_1) \right] Z_{n_1}^{(1)} \int_0^{a_1} \psi_{n_1}^{(1)}(x) \psi_n^{(3)}(x) dx = \\ & = \sum_{n=0}^{\infty} \left[c_n^{(1)+}(z_1) - c_n^{(1)-}(z_1) \right] Z_{n_1}^{(1)} \int_0^{a_1} \psi_{n_1}^{(1)}(x) \psi_n^{(1)}(x) dx \quad . \end{aligned} \quad (2.41)$$

Here,

$$\langle \psi_{n_1}^{(1)}(x) | \psi_n^{(3)}(x) \rangle_1 = \int_0^{a_1} \psi_{n_1}^{(1)}(x) \psi_n^{(3)}(x) dx \quad , \quad (2.42)$$

$$\langle \psi_{n_1}^{(1)}(x) | \psi_n^{(1)}(x) \rangle_1 = \int_0^{a_1} \psi_{n_1}^{(1)}(x) \psi_n^{(1)}(x) dx = \delta_{n_1, n} \quad , \quad (2.43)$$

such that

$$\begin{aligned} & \sum_{n=0}^{\infty} \left[c_n^{(3)+}(z_1) - c_n^{(3)-}(z_1) \right] Z_{n_1}^{(1)} \langle \psi_{n_1}^{(1)}(x) | \psi_n^{(3)}(x) \rangle_1 = \\ & = \sum_{n=0}^{\infty} \left[c_n^{(1)+}(z_1) - c_n^{(1)-}(z_1) \right] Z_{n_1}^{(1)} \delta_{n_1, n} \quad , \end{aligned} \quad (2.44)$$

or

$$\begin{aligned} & \left[c_{n_1}^{(1)+}(z_1) - c_{n_1}^{(1)-}(z_1) \right] Z_{n_1}^{(1)} = \\ & = \sum_{n=0}^{\infty} \left[c_n^{(3)+}(z_1) - c_n^{(3)-}(z_1) \right] Z_{n_1}^{(1)} \langle \psi_{n_1}^{(1)}(x) | \psi_n^{(3)}(x) \rangle_1 \quad , \end{aligned} \quad (2.45)$$

Finally, by multiplying the boundary condition for the magnetic field (2.36) by $Z_{n_2}^{(2)} \psi_{n_1}^{(1)}(x)$, where n_2 is a specific value of the coefficient n , and integrating over the interval $a - a_2 < x < a$, one obtains

$$\sum_{n=0}^{\infty} \left[c_n^{(3)+}(z_1) - c_n^{(3)-}(z_1) \right] Z_{n_2}^{(2)} \int_{a-a_2}^a \psi_{n_2}^{(2)}(x) \psi_n^{(3)}(x) dx =$$

$$= \sum_{n=0}^{\infty} \left[c_n^{(2)+}(z_1) - c_n^{(2)-}(z_1) \right] Z_{n_2}^{(2)} \int_{a-a_2}^a \psi_{n_2}^{(2)}(x) \psi_n^{(2)}(x) dx \quad . \quad (2.46)$$

Here,

$$\langle \psi_{n_2}^{(2)}(x) | \psi_n^{(3)}(x) \rangle_2 = \int_{a-a_2}^a \psi_{n_2}^{(2)}(x) \psi_n^{(3)}(x) dx \quad , \quad (2.47)$$

$$\langle \psi_{n_2}^{(2)}(x) | \psi_n^{(2)}(x) \rangle_2 = \int_{a-a_2}^a \psi_{n_2}^{(2)}(x) \psi_n^{(2)}(x) dx = \delta_{n_2, n} \quad , \quad (2.48)$$

such that

$$\begin{aligned} \sum_{n=0}^{\infty} \left[c_n^{(3)+}(z_1) - c_n^{(3)-}(z_1) \right] Z_{n_2}^{(2)} \langle \psi_{n_2}^{(2)}(x) | \psi_n^{(3)}(x) \rangle_2 &= \\ &= \sum_{n=0}^{\infty} \left[c_n^{(2)+}(z_1) - c_n^{(2)-}(z_1) \right] Z_{n_2}^{(2)} \delta_{n_2, n} \quad . \end{aligned} \quad (2.49)$$

or

$$\begin{aligned} &\left[c_{n_2}^{(2)+}(z_1) - c_{n_2}^{(2)-}(z_1) \right] Z_{n_2}^{(2)} = \\ &= \sum_{n=0}^{\infty} \left[c_n^{(3)+}(z_1) - c_n^{(3)-}(z_1) \right] Z_{n_2}^{(2)} \langle \psi_{n_2}^{(2)}(x) | \psi_n^{(3)}(x) \rangle_2 \quad . \end{aligned} \quad (2.50)$$

Collecting together equations (2.40), (2.45) and (2.50) the complete set of boundary conditions at the plane $z = z_1$ is obtained in the form

$$\begin{aligned} Z_{n_3}^{(3)} \left[c_{n_3}^{(3)+}(z_1) + c_{n_3}^{(3)-}(z_1) \right] &= \sum_{n=0}^{\infty} \left[c_n^{(1)+}(z_1) + c_n^{(1)-}(z_1) \right] Z_n^{(1)} \langle \psi_{n_3}^{(3)}(x) | \psi_n^{(1)}(x) \rangle_1 + \\ &+ \sum_{n=0}^{\infty} \left[c_n^{(2)+}(z_1) + c_n^{(2)-}(z_1) \right] Z_n^{(2)} \langle \psi_{n_3}^{(3)}(x) | \psi_n^{(2)}(x) \rangle_2 \quad , \end{aligned} \quad (2.51)$$

$$\begin{aligned} &Z_{n_1}^{(1)} \left[c_{n_1}^{(1)+}(z_1) - c_{n_1}^{(1)-}(z_1) \right] = \\ &= \sum_{n=0}^{\infty} \left[c_n^{(3)+}(z_1) - c_n^{(3)-}(z_1) \right] Z_{n_1}^{(1)} \langle \psi_{n_1}^{(1)}(x) | \psi_n^{(3)}(x) \rangle_1 \quad , \end{aligned} \quad (2.52)$$

$$\begin{aligned}
& Z_{n_2}^{(2)} \left[c_{n_2}^{(2)+}(z_1) - c_{n_2}^{(2)-}(z_1) \right] = \\
& = \sum_{n=0}^{\infty} \left[c_n^{(3)+}(z_1) - c_n^{(3)-}(z_1) \right] Z_{n_2}^{(2)} \langle \psi_{n_2}^{(2)}(x) | \psi_n^{(3)}(x) \rangle_2 \quad . \quad (2.53)
\end{aligned}$$

By means of an analogous procedure in the boundary plane $z = z_2$, it is easily shown that the corresponding complete set of boundary conditions at the plane $z = z_2$ has the form

$$\begin{aligned}
Z_{n_4}^{(4)} \left[c_{n_4}^{(4)+}(z_2) + c_{n_4}^{(4)-}(z_2) \right] &= \sum_{n=0}^{\infty} \left[c_n^{(1)+}(z_2) + c_n^{(1)-}(z_2) \right] Z_n^{(1)} \langle \psi_{n_4}^{(4)}(x) | \psi_n^{(1)}(x) \rangle_1 + \\
&+ \sum_{n=0}^{\infty} \left[c_n^{(2)+}(z_2) + c_n^{(2)-}(z_2) \right] Z_n^{(2)} \langle \psi_{n_4}^{(4)}(x) | \psi_n^{(2)}(x) \rangle_2 \quad , \quad (2.54)
\end{aligned}$$

$$\begin{aligned}
& Z_{n_1}^{(1)} \left[c_{n_1}^{(1)+}(z_2) - c_{n_1}^{(1)-}(z_2) \right] = \\
& = \sum_{n=0}^{\infty} \left[c_n^{(4)+}(z_2) - c_n^{(4)-}(z_2) \right] Z_{n_1}^{(1)} \langle \psi_{n_1}^{(1)}(x) | \psi_n^{(4)}(x) \rangle_1 \quad , \quad (2.55)
\end{aligned}$$

$$\begin{aligned}
& Z_{n_2}^{(2)} \left[c_{n_2}^{(2)+}(z_2) - c_{n_2}^{(2)-}(z_2) \right] = \\
& = \sum_{n=0}^{\infty} \left[c_n^{(4)+}(z_2) - c_n^{(4)-}(z_2) \right] Z_{n_2}^{(2)} \langle \psi_{n_2}^{(2)}(x) | \psi_n^{(4)}(x) \rangle_2 \quad . \quad (2.56)
\end{aligned}$$

The six equations (2.51)-(2.56) are the matrix equations for the mode coefficients at the boundaries $z = z_1$ and $z = z_2$. For the numerical implementation, each set of modes must be truncated to a finite number of N_i ($i = 1, 2, 3, 4$) lowest modes. The choice of N_i can be made based on the size of the region. The mode coefficients can then be collected into finite-dimensional vectors of the form

$$\mathbf{c}_{(i)}^{\pm}(z) = \begin{bmatrix} c_1^{(i)\pm}(z) \\ c_2^{(i)\pm}(z) \\ \vdots \\ c_{N_i}^{(i)\pm}(z) \end{bmatrix} \quad , \quad i = 1, 2, 3, 4 \quad . \quad (2.57)$$

The mode impedances in the four regions can be collected into four diagonal impedance matrices as follows

$$\mathbf{D}_{(i)} = \text{diag} \left\{ Z_n^{(i)} \right\}_{n=1}^{N_i} = \begin{bmatrix} Z_1^{(i)} & 0 & \dots & 0 \\ 0 & Z_2^{(i)} & \dots & 0 \\ \vdots & \vdots & \ddots & \vdots \\ 0 & 0 & \dots & Z_{N_i}^{(i)} \end{bmatrix} . \quad (2.58)$$

Finally the mode coupling matrix elements

$$K_{(i,j)n_i,n_j} = Z_{n_i}^{(i)} \langle \psi_{n_i}^{(i)}(x) | \psi_{n_j}^{(j)}(x) \rangle_i , \quad (2.59)$$

can be collected into the mode coupling $\mathbf{K}_{(i,j)}$ -matrices, where

$$n_i = 1, 2, \dots, N_i , \quad n_j = 1, 2, \dots, N_j , \quad (2.60)$$

and

$$i = 1, 2 , \quad j = 3, 4 . \quad (2.61)$$

The definitions (2.61) indicate that any of the regions $i = 1, 2$ couples to any of the regions $j = 3, 4$. On the other hand there is **no** coupling between the regions 1 and 2 or between the regions 3 and 4 respectively. From the above definition of the mode-coupling matrix elements, it is seen that the elements of the corresponding transposed matrix $\mathbf{K}_{(i,j)}^T$ are

$$K_{(i,j)n_i,n_j}^T = Z_{n_i}^{(i)} \langle \psi_{n_j}^{(j)}(x) | \psi_{n_i}^{(i)}(x) \rangle_i . \quad (2.62)$$

The matrix elements $\langle \psi_{n_i}^{(i)}(x) | \psi_{n_j}^{(j)}(x) \rangle_i$ are calculated using (2.17) such that

$$\langle \psi_{n_i}^{(i)}(x) | \psi_{n_j}^{(j)}(x) \rangle_i = \int_{I_i} \psi_{n_i}^{(i)}(x) \psi_{n_j}^{(j)}(x) dx , \quad (2.63)$$

where I_i denotes the interval of integration for each of the regions. For example for region 1, $I_1 = [0, a_1]$. From the explicit results (2.23)-(2.25) for the basis functions $\psi_n^{(i)}(x)$, it is seen that the matrix elements (2.63) are of the following general form

$$\langle \psi_{n_i}^{(i)}(x) | \psi_{n_j}^{(j)}(x) \rangle_i = \sqrt{\frac{2 - \delta_{n_i,0}}{a_i}} \sqrt{\frac{2 - \delta_{n_j,0}}{a_j}} \times$$

$$\times \int_{I_i} \cos \left[\frac{n_i \pi}{a_i} (x + b_i) \right] \cos \left[\frac{n_j \pi}{a_j} (x + b_j) \right] dx \quad . \quad (2.64)$$

For practical calculation of the matrix elements (2.63), the general integral therefore needs to be calculated

$$I = \int_{x_1}^{x_2} \cos (p_1 x + q_1) \cos (p_2 x + q_2) dx \quad . \quad (2.65)$$

Using the trigonometric formula

$$\cos \alpha \cos \beta = \frac{1}{2} [\cos(\alpha + \beta) + \cos(\alpha - \beta)] \quad , \quad (2.66)$$

one obtains

$$\begin{aligned} I &= \frac{1}{2} \int_{x_1}^{x_2} \cos[(p_1 + p_2)x + (q_1 + q_2)] dx + \\ &+ \frac{1}{2} \int_{x_1}^{x_2} \cos[(p_1 - p_2)x + (q_1 - q_2)] dx \quad , \end{aligned} \quad (2.67)$$

or finally

$$\begin{aligned} I &= \frac{1}{2(p_1 + p_2)} \{ \sin[(p_1 + p_2)x_2 + (q_1 + q_2)] - \sin[(p_1 + p_2)x_1 + (q_1 + q_2)] \} + \\ &+ \frac{1}{2(p_1 - p_2)} \{ \sin[(p_1 - p_2)x_2 + (q_1 - q_2)] - \sin[(p_1 - p_2)x_1 + (q_1 - q_2)] \} \quad . \end{aligned} \quad (2.68)$$

This integral will be used for numerical calculation of the matrix elements (2.63). Using now the matrix notation (2.57)-(2.59), the six equations (2.51)-(2.56) can be rewritten as follows

$$\mathbf{D}_{(3)} \left[\mathbf{c}_{(3)}^+(z_1) + \mathbf{c}_{(3)}^-(z_1) \right] = \mathbf{K}_{(1,3)}^T \left[\mathbf{c}_{(1)}^+(z_1) + \mathbf{c}_{(1)}^-(z_1) \right] + \mathbf{K}_{(2,3)}^T \left[\mathbf{c}_{(2)}^+(z_1) + \mathbf{c}_{(2)}^-(z_1) \right] \quad , \quad (2.69)$$

$$\mathbf{D}_{(1)} \left[\mathbf{c}_{(1)}^+(z_1) - \mathbf{c}_{(1)}^-(z_1) \right] = \mathbf{K}_{(1,3)} \left[\mathbf{c}_{(3)}^+(z_1) - \mathbf{c}_{(3)}^-(z_1) \right] \quad , \quad (2.70)$$

$$\mathbf{D}_{(2)} \left[\mathbf{c}_{(2)}^+(z_1) - \mathbf{c}_{(2)}^-(z_1) \right] = \mathbf{K}_{(2,3)} \left[\mathbf{c}_{(3)}^+(z_1) - \mathbf{c}_{(3)}^-(z_1) \right] \quad , \quad (2.71)$$

$$\mathbf{D}_{(4)} \left[\mathbf{c}_{(4)}^+(z_2) + \mathbf{c}_{(4)}^-(z_2) \right] = \mathbf{K}_{(1,4)}^T \left[\mathbf{c}_{(1)}^+(z_2) + \mathbf{c}_{(1)}^-(z_2) \right] + \mathbf{K}_{(2,4)}^T \left[\mathbf{c}_{(2)}^+(z_2) + \mathbf{c}_{(2)}^-(z_2) \right] , \quad (2.72)$$

$$\mathbf{D}_{(1)} \left[\mathbf{c}_{(1)}^+(z_2) - \mathbf{c}_{(1)}^-(z_2) \right] = \mathbf{K}_{(1,4)} \left[\mathbf{c}_{(4)}^+(z_2) - \mathbf{c}_{(4)}^-(z_2) \right] , \quad (2.73)$$

$$\mathbf{D}_{(2)} \left[\mathbf{c}_{(2)}^+(z_2) - \mathbf{c}_{(2)}^-(z_2) \right] = \mathbf{K}_{(2,4)} \left[\mathbf{c}_{(4)}^+(z_2) - \mathbf{c}_{(4)}^-(z_2) \right] . \quad (2.74)$$

Each individual mode can, by definition, be represented by the fields

$$E_n^{(i)\pm}(x, z) = A_n^{(i)} Z_n^{(i)} \psi_n^{(i)}(x) \exp(\mp j k_{zn}^i z) = c_n^{(i)\pm}(z) Z_n^{(i)} \psi_n^{(i)}(x) , \quad (2.75)$$

$$H_n^{(i)\pm}(x, z) = \pm A_n^{(i)} \psi_n^{(i)}(x) \exp(\mp j k_{zn}^i z) = \pm c_n^{(i)\pm}(z) \psi_n^{(i)}(x) . \quad (2.76)$$

Thus for homogeneous solutions for the fields, with no sources in the regions, one has

$$c_n^{(i)\pm}(z) = A_n^{(i)} \exp(\mp j k_{zn}^i z) , \quad (2.77)$$

such that

$$c_n^{(i)\pm}(z_2) = \exp[\mp j k_{zn}^i (z_2 - z_1)] A_n^{(i)} \exp(\mp j k_{zn}^i z_1) , \quad (2.78)$$

or

$$c_n^{(i)\pm}(z_2) = \exp[\mp j k_{zn}^i (z_2 - z_1)] c_n^{(i)\pm}(z_1) , \quad (2.79)$$

Based on the above result for propagation of the mode coefficients, it is here convenient to introduce the following diagonal matrix

$$\mathbf{P}_{(i)}^\pm(z_2 - z_1) = \text{diag} \left\{ \exp[\mp j k_{zn}^i (z_2 - z_1)] \right\}_{n=1}^{N_i} , \quad i = 1, 2, 3, 4 . \quad (2.80)$$

Introducing here $\Delta z = z_2 - z_1$, one can write

$$\mathbf{P}_{(i)}^\pm(\Delta z) = \begin{bmatrix} \exp[\mp j k_{z1}^i \Delta z] & 0 & .. & 0 \\ 0 & \exp[\mp j k_{z2}^i \Delta z] & .. & 0 \\ : & : & : & : \\ 0 & 0 & .. & \exp[\mp j k_{zN_i}^i \Delta z] \end{bmatrix} . \quad (2.81)$$

Using this definition of the matrices $\mathbf{P}_{(i)}^\pm$ and the definition of the vectors $\mathbf{c}_{(i)}^\pm(z)$, i.e.

$$\mathbf{c}_{(i)}^\pm(z) = \begin{bmatrix} c_1^{(i)\pm}(z) \\ c_2^{(i)\pm}(z) \\ \vdots \\ c_{N_i}^{(i)\pm}(z) \end{bmatrix}, \quad i = 1, 2, 3, 4 \quad . \quad (2.82)$$

it is seen that the propagation equations (2.79) for different modes and regions can be summarized into the following matrix equation

$$\mathbf{c}_{(i)}^\pm(z_2) = \mathbf{P}_{(i)}^\pm(\Delta z) \mathbf{c}_{(i)}^\pm(z_1) = \mathbf{P}_{(i)}^\pm(z_2 - z_1) \mathbf{c}_{(i)}^\pm(z_1) \quad , \quad i = 1, 2, 3, 4 \quad . \quad (2.83)$$

2.4 Scattering analysis of TM waves

Let us now consider the scattering of TM_n waves from the conductive obstacle depicted in Fig. 2.4. From the geometry of the problem, it is convenient to use the same number of modes at each side of the conductive obstacle, i.e. in the regions 3 and 4. Thus, $N_3 = N_4 = N_0$ is assumed. Hence,

$$\mathbf{D}_{(3)} = \mathbf{D}_{(4)} = \mathbf{D}_{(0)} \quad , \quad \mathbf{K}_{(1,3)} = \mathbf{K}_{(1,4)} = \mathbf{K}_{(1)} \quad , \quad \mathbf{K}_{(2,3)} = \mathbf{K}_{(2,4)} = \mathbf{K}_{(2)} \quad (2.84)$$

Furthermore, in the regions 1 and 2, the shorthand notation

$$\begin{aligned} \mathbf{P}_{(1)} &= \mathbf{P}_{(1)}^+(z_2 - z_1) = \mathbf{P}_{(1)}^-(z_1 - z_2) \quad , \\ \mathbf{P}_{(2)} &= \mathbf{P}_{(2)}^+(z_2 - z_1) = \mathbf{P}_{(2)}^-(z_1 - z_2) \quad . \end{aligned} \quad (2.85)$$

can be defined. Using the notation (2.85) in the matrix equations (2.83), one can further write

$$\mathbf{c}_{(1)}^+(z_2) = \mathbf{P}_{(1)} \mathbf{c}_{(1)}^+(z_1) \quad , \quad (2.86)$$

$$\mathbf{c}_{(1)}^-(z_1) = \mathbf{P}_{(1)} \mathbf{c}_{(1)}^-(z_2) \quad , \quad (2.87)$$

$$\mathbf{c}_{(2)}^+(z_2) = \mathbf{P}_{(2)} \mathbf{c}_{(2)}^+(z_1) \quad , \quad (2.88)$$

$$\mathbf{c}_{(2)}^-(z_1) = \mathbf{P}_{(2)} \mathbf{c}_{(2)}^-(z_2) \quad . \quad (2.89)$$

Thus the six matrix equations (2.69)-(2.74) can be rewritten as follows

$$\begin{aligned} \mathbf{D}_{(0)} \left[\mathbf{c}_{(3)}^+(z_1) + \mathbf{c}_{(3)}^-(z_1) \right] &= \mathbf{K}_{(1)}^T \left[\mathbf{c}_{(1)}^+(z_1) + \mathbf{P}_{(1)} \mathbf{c}_{(1)}^-(z_2) \right] + \\ &+ \mathbf{K}_{(2)}^T \left[\mathbf{c}_{(2)}^+(z_1) + \mathbf{P}_{(1)} \mathbf{c}_{(2)}^-(z_2) \right] \quad , \end{aligned} \quad (2.90)$$

$$\mathbf{D}_{(1)} \left[\mathbf{c}_{(1)}^+(z_1) - \mathbf{P}_{(1)} \mathbf{c}_{(1)}^-(z_2) \right] = \mathbf{K}_{(1)} \left[\mathbf{c}_{(3)}^+(z_1) - \mathbf{c}_{(3)}^-(z_1) \right] \quad , \quad (2.91)$$

$$\mathbf{D}_{(2)} \left[\mathbf{c}_{(2)}^+(z_1) - \mathbf{P}_{(2)} \mathbf{c}_{(2)}^-(z_2) \right] = \mathbf{K}_{(2)} \left[\mathbf{c}_{(3)}^+(z_1) - \mathbf{c}_{(3)}^-(z_1) \right] \quad , \quad (2.92)$$

$$\begin{aligned} \mathbf{D}_{(0)} \left[\mathbf{c}_{(4)}^+(z_2) + \mathbf{c}_{(4)}^-(z_2) \right] &= \mathbf{K}_{(1)}^T \left[\mathbf{P}_{(1)} \mathbf{c}_{(1)}^+(z_1) + \mathbf{c}_{(1)}^-(z_2) \right] + \\ &+ \mathbf{K}_{(2)}^T \left[\mathbf{P}_{(2)} \mathbf{c}_{(2)}^+(z_1) + \mathbf{c}_{(2)}^-(z_2) \right] \quad , \end{aligned} \quad (2.93)$$

$$\mathbf{D}_{(1)} \left[\mathbf{P}_{(1)} \mathbf{c}_{(1)}^+(z_1) - \mathbf{c}_{(1)}^-(z_2) \right] = \mathbf{K}_{(1)} \left[\mathbf{c}_{(4)}^+(z_2) - \mathbf{c}_{(4)}^-(z_2) \right] \quad , \quad (2.94)$$

$$\mathbf{D}_{(2)} \left[\mathbf{P}_{(2)} \mathbf{c}_{(2)}^+(z_1) - \mathbf{c}_{(2)}^-(z_2) \right] = \mathbf{K}_{(2)} \left[\mathbf{c}_{(4)}^+(z_2) - \mathbf{c}_{(4)}^-(z_2) \right] \quad . \quad (2.95)$$

The two equations (2.91) and (2.94) can be rewritten as follows

$$\mathbf{c}_{(1)}^+(z_1) - \mathbf{P}_{(1)} \mathbf{c}_{(1)}^-(z_2) = \mathbf{D}_{(1)}^{-1} \mathbf{K}_{(1)} \left[\mathbf{c}_{(3)}^+(z_1) - \mathbf{c}_{(3)}^-(z_1) \right] \quad , \quad (2.96)$$

$$\mathbf{P}_{(1)} \mathbf{c}_{(1)}^+(z_1) - \mathbf{c}_{(1)}^-(z_2) = \mathbf{D}_{(1)}^{-1} \mathbf{K}_{(1)} \left[\mathbf{c}_{(4)}^+(z_2) - \mathbf{c}_{(4)}^-(z_2) \right] \quad , \quad (2.97)$$

or

$$\mathbf{c}_{(1)}^+(z_1) - \mathbf{P}_{(1)} \mathbf{c}_{(1)}^-(z_2) = \mathbf{D}_{(1)}^{-1} \mathbf{K}_{(1)} \left[\mathbf{c}_{(3)}^+(z_1) - \mathbf{c}_{(3)}^-(z_1) \right] \quad , \quad (2.98)$$

$$-\mathbf{c}_{(1)}^+(z_1) + \mathbf{P}_{(1)}^{-1} \mathbf{c}_{(1)}^-(z_2) = -\mathbf{P}_{(1)}^{-1} \mathbf{D}_{(1)}^{-1} \mathbf{K}_{(1)} \left[\mathbf{c}_{(4)}^+(z_2) - \mathbf{c}_{(4)}^-(z_2) \right] \quad , \quad (2.99)$$

Adding together the two equations (2.98) and (2.99), one obtains

$$\begin{aligned} (\mathbf{P}_{(1)}^{-1} - \mathbf{P}_{(1)})\mathbf{c}_{(1)}^-(z_2) &= \mathbf{D}_{(1)}^{-1}\mathbf{K}_{(1)} \left[\mathbf{c}_{(3)}^+(z_1) - \mathbf{c}_{(3)}^-(z_1) \right] - \\ &\quad - \mathbf{P}_{(1)}^{-1}\mathbf{D}_{(1)}^{-1}\mathbf{K}_{(1)} \left[\mathbf{c}_{(4)}^+(z_2) - \mathbf{c}_{(4)}^-(z_2) \right] \quad , \end{aligned} \quad (2.100)$$

Multiplying the equation (2.100) from the right by $\mathbf{P}_{(1)}$, gives

$$\begin{aligned} (\mathbf{I} - \mathbf{P}_{(1)}^2) \mathbf{c}_{(1)}^-(z_2) &= \mathbf{P}_{(1)}\mathbf{D}_{(1)}^{-1}\mathbf{K}_{(1)} \left[\mathbf{c}_{(3)}^+(z_1) - \mathbf{c}_{(3)}^-(z_1) \right] - \\ &\quad - \mathbf{D}_{(1)}^{-1}\mathbf{K}_{(1)} \left[\mathbf{c}_{(4)}^+(z_2) - \mathbf{c}_{(4)}^-(z_2) \right] \quad , \end{aligned} \quad (2.101)$$

The two equations (2.96) and (2.97) can also be rewritten as

$$\mathbf{c}_{(1)}^+(z_1) - \mathbf{P}_{(1)}\mathbf{c}_{(1)}^-(z_2) = \mathbf{D}_{(1)}^{-1}\mathbf{K}_{(1)} \left[\mathbf{c}_{(3)}^+(z_1) - \mathbf{c}_{(3)}^-(z_1) \right] \quad , \quad (2.102)$$

$$-\mathbf{P}_{(1)}^2\mathbf{c}_{(1)}^+(z_1) + \mathbf{P}_{(1)}\mathbf{c}_{(1)}^-(z_2) = -\mathbf{P}_{(1)}\mathbf{D}_{(1)}^{-1}\mathbf{K}_{(1)} \left[\mathbf{c}_{(4)}^+(z_2) - \mathbf{c}_{(4)}^-(z_2) \right] \quad , \quad (2.103)$$

Adding together the two equations (2.102) and (2.103), one obtains

$$\begin{aligned} (\mathbf{I} - \mathbf{P}_{(1)}^2) \mathbf{c}_{(1)}^+(z_1) &= \mathbf{D}_{(1)}^{-1}\mathbf{K}_{(1)} \left[\mathbf{c}_{(3)}^+(z_1) - \mathbf{c}_{(3)}^-(z_1) \right] - \\ &\quad - \mathbf{P}_{(1)}\mathbf{D}_{(1)}^{-1}\mathbf{K}_{(1)} \left[\mathbf{c}_{(4)}^+(z_2) - \mathbf{c}_{(4)}^-(z_2) \right] \quad , \end{aligned} \quad (2.104)$$

Multiplying from the right by $(\mathbf{I} - \mathbf{P}_{(1)}^2)^{-1}$, the two equations (2.101) and (2.104), can be rewritten as

$$\mathbf{c}_{(1)}^+(z_1) = \mathbf{A}_{(1)} \left[\mathbf{c}_{(3)}^+(z_1) - \mathbf{c}_{(3)}^-(z_1) \right] - \mathbf{B}_{(1)} \left[\mathbf{c}_{(4)}^+(z_2) - \mathbf{c}_{(4)}^-(z_2) \right] \quad , \quad (2.105)$$

$$\mathbf{c}_{(1)}^-(z_2) = \mathbf{B}_{(1)} \left[\mathbf{c}_{(3)}^+(z_1) - \mathbf{c}_{(3)}^-(z_1) \right] - \mathbf{A}_{(1)} \left[\mathbf{c}_{(4)}^+(z_2) - \mathbf{c}_{(4)}^-(z_2) \right] \quad , \quad (2.106)$$

where the two new matrices $\mathbf{A}_{(1)}$ and $\mathbf{B}_{(1)}$ are introduced using

$$\mathbf{A}_{(1)} = (\mathbf{I} - \mathbf{P}_{(1)}^2)^{-1}\mathbf{D}_{(1)}^{-1}\mathbf{K}_{(1)} \quad , \quad \mathbf{B}_{(1)} = (\mathbf{I} - \mathbf{P}_{(1)}^2)^{-1}\mathbf{P}_{(1)}\mathbf{D}_{(1)}^{-1}\mathbf{K}_{(1)} \quad . \quad (2.107)$$

Next, the two equations (2.92) and (2.95) are considered, which can be rewritten as follows

$$\mathbf{c}_{(2)}^+(z_1) - \mathbf{P}_{(2)}\mathbf{c}_{(2)}^-(z_2) = \mathbf{D}_{(2)}^{-1}\mathbf{K}_{(2)} \left[\mathbf{c}_{(3)}^+(z_1) - \mathbf{c}_{(3)}^-(z_1) \right] \quad , \quad (2.108)$$

$$\mathbf{P}_{(2)}\mathbf{c}_{(2)}^+(z_1) - \mathbf{c}_{(2)}^-(z_2) = \mathbf{D}_{(2)}^{-1}\mathbf{K}_{(2)} \left[\mathbf{c}_{(4)}^+(z_2) - \mathbf{c}_{(4)}^-(z_2) \right] \quad . \quad (2.109)$$

Following the analogous procedure leading to the solutions (2.105) and (2.106), the following results are obtained from (2.108) and (2.109)

$$\mathbf{c}_{(2)}^+(z_1) = \mathbf{A}_{(2)} \left[\mathbf{c}_{(3)}^+(z_1) - \mathbf{c}_{(3)}^-(z_1) \right] - \mathbf{B}_{(2)} \left[\mathbf{c}_{(4)}^+(z_2) - \mathbf{c}_{(4)}^-(z_2) \right] \quad , \quad (2.110)$$

$$\mathbf{c}_{(2)}^-(z_2) = \mathbf{B}_{(2)} \left[\mathbf{c}_{(3)}^+(z_1) - \mathbf{c}_{(3)}^-(z_1) \right] - \mathbf{A}_{(2)} \left[\mathbf{c}_{(4)}^+(z_2) - \mathbf{c}_{(4)}^-(z_2) \right] \quad , \quad (2.111)$$

with

$$\mathbf{A}_{(2)} = (\mathbf{I} - \mathbf{P}_{(2)}^2)^{-1}\mathbf{D}_{(2)}^{-1}\mathbf{K}_{(2)} \quad , \quad \mathbf{B}_{(2)} = (\mathbf{I} - \mathbf{P}_{(2)}^2)^{-1}\mathbf{P}_{(2)}\mathbf{D}_{(2)}^{-1}\mathbf{K}_{(2)} \quad . \quad (2.112)$$

Let us now insert the above obtained results for $\mathbf{c}_{(1)}^+(z_1)$, $\mathbf{c}_{(1)}^-(z_2)$, $\mathbf{c}_{(2)}^+(z_1)$ and $\mathbf{c}_{(2)}^-(z_2)$ into the equation (2.90), i.e.

$$\begin{aligned} \mathbf{D}_{(0)} \left[\mathbf{c}_{(3)}^+(z_1) + \mathbf{c}_{(3)}^-(z_1) \right] &= \mathbf{K}_{(1)}^T \mathbf{c}_{(1)}^+(z_1) + \\ &+ \mathbf{K}_{(1)}^T \mathbf{P}_{(1)} \mathbf{c}_{(1)}^-(z_2) + \mathbf{K}_{(2)}^T \mathbf{c}_{(2)}^+(z_1) + \mathbf{K}_{(2)}^T \mathbf{P}_{(1)} \mathbf{c}_{(2)}^-(z_2) \quad , \end{aligned} \quad (2.113)$$

such that

$$\begin{aligned} \mathbf{D}_{(0)} \left[\mathbf{c}_{(3)}^+(z_1) + \mathbf{c}_{(3)}^-(z_1) \right] &= \\ &= \mathbf{K}_{(1)}^T \left\{ \mathbf{A}_{(1)} \left[\mathbf{c}_{(3)}^+(z_1) - \mathbf{c}_{(3)}^-(z_1) \right] - \mathbf{B}_{(1)} \left[\mathbf{c}_{(4)}^+(z_2) - \mathbf{c}_{(4)}^-(z_2) \right] \right\} + \\ &+ \mathbf{K}_{(1)}^T \mathbf{P}_{(1)} \left\{ \mathbf{B}_{(1)} \left[\mathbf{c}_{(3)}^+(z_1) - \mathbf{c}_{(3)}^-(z_1) \right] - \mathbf{A}_{(1)} \left[\mathbf{c}_{(4)}^+(z_2) - \mathbf{c}_{(4)}^-(z_2) \right] \right\} + \end{aligned}$$

$$\begin{aligned}
& +\mathbf{K}_{(2)}^T \left\{ \mathbf{A}_{(2)} \left[\mathbf{c}_{(3)}^+(z_1) - \mathbf{c}_{(3)}^-(z_1) \right] - \mathbf{B}_{(2)} \left[\mathbf{c}_{(4)}^+(z_2) - \mathbf{c}_{(4)}^-(z_2) \right] \right\} + \\
& +\mathbf{K}_{(2)}^T \mathbf{P}_{(1)} \left\{ \mathbf{B}_{(2)} \left[\mathbf{c}_{(3)}^+(z_1) - \mathbf{c}_{(3)}^-(z_1) \right] - \mathbf{A}_{(2)} \left[\mathbf{c}_{(4)}^+(z_2) - \mathbf{c}_{(4)}^-(z_2) \right] \right\} \quad , \quad (2.114)
\end{aligned}$$

or regrouping the modes

$$\begin{aligned}
& \mathbf{D}_{(0)} \mathbf{c}_{(3)}^+(z_1) + \mathbf{D}_{(0)} \mathbf{c}_{(3)}^-(z_1) = \\
& = \left[\mathbf{K}_{(1)}^T \mathbf{A}_{(1)} + \mathbf{K}_{(1)}^T \mathbf{P}_{(1)} \mathbf{B}_{(1)} + \mathbf{K}_{(2)}^T \mathbf{A}_{(2)} + \mathbf{K}_{(2)}^T \mathbf{P}_{(2)} \mathbf{B}_{(2)} \right] \mathbf{c}_{(3)}^+(z_1) - \\
& - \left[\mathbf{K}_{(1)}^T \mathbf{A}_{(1)} + \mathbf{K}_{(1)}^T \mathbf{P}_{(1)} \mathbf{B}_{(1)} + \mathbf{K}_{(2)}^T \mathbf{A}_{(2)} + \mathbf{K}_{(2)}^T \mathbf{P}_{(2)} \mathbf{B}_{(2)} \right] \mathbf{c}_{(3)}^-(z_1) - \\
& - \left[\mathbf{K}_{(1)}^T \mathbf{B}_{(1)} + \mathbf{K}_{(1)}^T \mathbf{P}_{(1)} \mathbf{A}_{(1)} + \mathbf{K}_{(2)}^T \mathbf{B}_{(2)} + \mathbf{K}_{(2)}^T \mathbf{P}_{(2)} \mathbf{A}_{(2)} \right] \mathbf{c}_{(4)}^+(z_2) + \\
& + \left[\mathbf{K}_{(1)}^T \mathbf{B}_{(1)} + \mathbf{K}_{(1)}^T \mathbf{P}_{(1)} \mathbf{A}_{(1)} + \mathbf{K}_{(2)}^T \mathbf{B}_{(2)} + \mathbf{K}_{(2)}^T \mathbf{P}_{(2)} \mathbf{A}_{(2)} \right] \mathbf{c}_{(4)}^-(z_2) \quad . \quad (2.115)
\end{aligned}$$

Introducing here two new matrices

$$\mathbf{M} = \mathbf{K}_{(1)}^T \mathbf{A}_{(1)} + \mathbf{K}_{(1)}^T \mathbf{P}_{(1)} \mathbf{B}_{(1)} + \mathbf{K}_{(2)}^T \mathbf{A}_{(2)} + \mathbf{K}_{(2)}^T \mathbf{P}_{(2)} \mathbf{B}_{(2)} \quad , \quad (2.116)$$

$$\mathbf{N} = \mathbf{K}_{(1)}^T \mathbf{B}_{(1)} + \mathbf{K}_{(1)}^T \mathbf{P}_{(1)} \mathbf{A}_{(1)} + \mathbf{K}_{(2)}^T \mathbf{B}_{(2)} + \mathbf{K}_{(2)}^T \mathbf{P}_{(2)} \mathbf{A}_{(2)} \quad , \quad (2.117)$$

the matrix equation (2.115) becomes

$$\begin{aligned}
& \mathbf{D}_{(0)} \mathbf{c}_{(3)}^+(z_1) + \mathbf{D}_{(0)} \mathbf{c}_{(3)}^-(z_1) = \\
& \mathbf{M} \mathbf{c}_{(3)}^+(z_1) - \mathbf{M} \mathbf{c}_{(3)}^-(z_1) - \mathbf{N} \mathbf{c}_{(4)}^+(z_2) + \mathbf{N} \mathbf{c}_{(4)}^-(z_2) \quad , \quad (2.118)
\end{aligned}$$

or finally

$$(\mathbf{D}_{(0)} - \mathbf{M}) \mathbf{c}_{(3)}^+(z_1) + (\mathbf{D}_{(0)} + \mathbf{M}) \mathbf{c}_{(3)}^-(z_1) + \mathbf{N} \mathbf{c}_{(4)}^+(z_2) - \mathbf{N} \mathbf{c}_{(4)}^-(z_2) = 0 \quad . \quad (2.119)$$

If the above obtained results for $\mathbf{c}_{(1)}^+(z_1)$, $\mathbf{c}_{(1)}^-(z_2)$, $\mathbf{c}_{(2)}^+(z_1)$ and $\mathbf{c}_{(2)}^-(z_2)$ are inserted into the equation (2.93), following an analogous procedure, one obtains

$$-\mathbf{N} \mathbf{c}_{(3)}^+(z_1) + \mathbf{N} \mathbf{c}_{(3)}^-(z_1) + (\mathbf{D}_{(0)} + \mathbf{M}) \mathbf{c}_{(4)}^+(z_2) + (\mathbf{D}_{(0)} - \mathbf{M}) \mathbf{c}_{(4)}^-(z_2) = 0 \quad . \quad (2.120)$$

The two matrix equations (2.122) and (2.120) can be combined into a single matrix equation of the form

$$\begin{bmatrix} \mathbf{D}_{(0)} - \mathbf{M} & \mathbf{D}_{(0)} + \mathbf{M} & \mathbf{N} & -\mathbf{N} \\ -\mathbf{N} & \mathbf{N} & \mathbf{D}_{(0)} + \mathbf{M} & \mathbf{D}_{(0)} - \mathbf{M} \end{bmatrix} \begin{bmatrix} \mathbf{c}_{(3)}^+(z_1) \\ \mathbf{c}_{(3)}^-(z_1) \\ \mathbf{c}_{(4)}^+(z_2) \\ \mathbf{c}_{(4)}^-(z_2) \end{bmatrix} = 0 \quad . \quad (2.121)$$

2.5 Scattering matrices for TM waves

From the matrix equation (2.121), one can write

$$\begin{bmatrix} \mathbf{D}_{(0)} + \mathbf{M} & \mathbf{N} \\ \mathbf{N} & \mathbf{D}_{(0)} + \mathbf{M} \end{bmatrix} \begin{bmatrix} \mathbf{c}_{(3)}^-(z_1) \\ \mathbf{c}_{(4)}^+(z_2) \end{bmatrix} + \begin{bmatrix} \mathbf{D}_{(0)} - \mathbf{M} & -\mathbf{N} \\ -\mathbf{N} & \mathbf{D}_{(0)} - \mathbf{M} \end{bmatrix} \begin{bmatrix} \mathbf{c}_{(3)}^+(z_1) \\ \mathbf{c}_{(4)}^-(z_2) \end{bmatrix} = 0 \quad , \quad (2.122)$$

or

$$\begin{bmatrix} \mathbf{c}_{(3)}^-(z_1) \\ \mathbf{c}_{(4)}^+(z_2) \end{bmatrix} = \mathbf{S}' \begin{bmatrix} \mathbf{c}_{(3)}^+(z_1) \\ \mathbf{c}_{(4)}^-(z_2) \end{bmatrix} \quad , \quad (2.123)$$

where the scattering matrix for our two-dimensional model is defined as follows

$$\begin{aligned} \mathbf{S}' &= \begin{bmatrix} \mathbf{S}'_{11} & \mathbf{S}'_{12} \\ \mathbf{S}'_{21} & \mathbf{S}'_{22} \end{bmatrix} = \\ &= \begin{bmatrix} \mathbf{D}_{(0)} + \mathbf{M} & \mathbf{N} \\ \mathbf{N} & \mathbf{D}_{(0)} + \mathbf{M} \end{bmatrix}^{-1} \times \begin{bmatrix} \mathbf{D}_{(0)} - \mathbf{M} & -\mathbf{N} \\ -\mathbf{N} & \mathbf{D}_{(0)} - \mathbf{M} \end{bmatrix} \quad . \quad (2.124) \end{aligned}$$

The scattering matrix (2.124) describes the propagation over the metal obstacle only (from z_1 to z_2). Since the conductor is immersed in a "cell" extending from z_V ($< z_1$) to z_H ($> z_2$), one needs to find the scattering matrix for the propagation over the entire "cell", that is from z_V to z_H . In order to do that, the matrices

$$\mathbf{P}_V = \mathbf{P}_{(0)}^+(z_1 - z_V) \quad , \quad \mathbf{P}_H = \mathbf{P}_{(0)}^+(z_H - z_2) \quad . \quad (2.125)$$

are introduced. Using these matrices, one can write

$$\mathbf{c}^+(z_1) = \mathbf{P}_V \mathbf{c}^+(z_V) \quad , \quad (2.126)$$

$$\mathbf{c}^-(z_V) = \mathbf{P}_V \mathbf{c}^-(z_1) \quad , \quad (2.127)$$

$$\mathbf{c}^+(z_H) = \mathbf{P}_H \mathbf{c}^+(z_2) \quad , \quad (2.128)$$

$$\mathbf{c}^-(z_2) = \mathbf{P}_H \mathbf{c}^-(z_H) \quad . \quad (2.129)$$

The results (2.127) and (2.128) can be collected into a matrix equation

$$\begin{bmatrix} \mathbf{c}^-(z_V) \\ \mathbf{c}^+(z_H) \end{bmatrix} = \begin{bmatrix} \mathbf{P}_V & 0 \\ 0 & \mathbf{P}_H \end{bmatrix} \begin{bmatrix} \mathbf{c}^-(z_1) \\ \mathbf{c}^+(z_2) \end{bmatrix} \quad . \quad (2.130)$$

Using the equation (2.123), one further obtains

$$\begin{bmatrix} \mathbf{c}^-(z_V) \\ \mathbf{c}^+(z_H) \end{bmatrix} = \begin{bmatrix} \mathbf{P}_V & 0 \\ 0 & \mathbf{P}_H \end{bmatrix} \begin{bmatrix} \mathbf{S}'_{11} & \mathbf{S}'_{12} \\ \mathbf{S}'_{21} & \mathbf{S}'_{22} \end{bmatrix} \begin{bmatrix} \mathbf{c}^+(z_1) \\ \mathbf{c}^-(z_2) \end{bmatrix} \quad . \quad (2.131)$$

Using now the results (2.126) and (2.127) one can write

$$\begin{bmatrix} \mathbf{c}^+(z_1) \\ \mathbf{c}^-(z_2) \end{bmatrix} = \begin{bmatrix} \mathbf{P}_V & 0 \\ 0 & \mathbf{P}_H \end{bmatrix} \begin{bmatrix} \mathbf{c}^+(z_V) \\ \mathbf{c}^-(z_H) \end{bmatrix} \quad . \quad (2.132)$$

Inserting the equation (2.132) into (2.131) one obtains

$$\begin{bmatrix} \mathbf{c}^-(z_V) \\ \mathbf{c}^+(z_H) \end{bmatrix} = \begin{bmatrix} \mathbf{P}_V \mathbf{S}'_{11} & \mathbf{P}_V \mathbf{S}'_{12} \\ \mathbf{P}_H \mathbf{S}'_{21} & \mathbf{P}_H \mathbf{S}'_{22} \end{bmatrix} \begin{bmatrix} \mathbf{P}_V & 0 \\ 0 & \mathbf{P}_H \end{bmatrix} \begin{bmatrix} \mathbf{c}^+(z_V) \\ \mathbf{c}^-(z_H) \end{bmatrix} \quad . \quad (2.133)$$

or

$$\begin{bmatrix} \mathbf{c}^-(z_V) \\ \mathbf{c}^+(z_H) \end{bmatrix} = \begin{bmatrix} \mathbf{P}_V \mathbf{S}'_{11} \mathbf{P}_V & \mathbf{P}_V \mathbf{S}'_{12} \mathbf{P}_H \\ \mathbf{P}_H \mathbf{S}'_{21} \mathbf{P}_V & \mathbf{P}_H \mathbf{S}'_{22} \mathbf{P}_H \end{bmatrix} \begin{bmatrix} \mathbf{c}^+(z_V) \\ \mathbf{c}^-(z_H) \end{bmatrix} \quad , \quad (2.134)$$

or

$$\begin{bmatrix} \mathbf{c}^-(z_V) \\ \mathbf{c}^+(z_H) \end{bmatrix} = \begin{bmatrix} \mathbf{S}_{11} & \mathbf{S}_{12} \\ \mathbf{S}_{21} & \mathbf{S}_{22} \end{bmatrix} \begin{bmatrix} \mathbf{c}^+(z_V) \\ \mathbf{c}^-(z_H) \end{bmatrix} \quad , \quad (2.135)$$

or finally

$$\begin{bmatrix} \mathbf{c}^-(z_V) \\ \mathbf{c}^+(z_H) \end{bmatrix} = \mathbf{S} \begin{bmatrix} \mathbf{c}^+(z_V) \\ \mathbf{c}^-(z_H) \end{bmatrix} \quad , \quad (2.136)$$

where the complete scattering matrix elements for propagation over the entire "cell", i.e. from z_V to z_H as indicated in Fig. 2.4, is defined by

$$\mathbf{S}_{11} = \mathbf{P}_V \mathbf{S}'_{11} \mathbf{P}_V, \quad \mathbf{S}_{12} = \mathbf{P}_V \mathbf{S}'_{12} \mathbf{P}_H, \quad \mathbf{S}_{21} = \mathbf{P}_H \mathbf{S}'_{21} \mathbf{P}_V, \quad \mathbf{S}_{22} = \mathbf{P}_H \mathbf{S}'_{22} \mathbf{P}_H. \quad (2.137)$$

2.6 Cascading of two cells

Consider two neighboring cells denoted by "a" ($z_1 \leq z \leq z_2$) and "b" ($z_2 \leq z \leq z_3$). Then one has

$$\mathbf{c}^-(z_1) = S_{11}^a \mathbf{c}^+(z_1) + S_{12}^a \mathbf{c}^-(z_2), \quad (2.138)$$

$$\mathbf{c}^+(z_2) = S_{21}^a \mathbf{c}^+(z_1) + S_{22}^a \mathbf{c}^-(z_2), \quad (2.139)$$

and

$$\mathbf{c}^-(z_2) = S_{11}^b \mathbf{c}^+(z_2) + S_{12}^b \mathbf{c}^-(z_3), \quad (2.140)$$

$$\mathbf{c}^+(z_3) = S_{21}^b \mathbf{c}^+(z_2) + S_{22}^b \mathbf{c}^-(z_3). \quad (2.141)$$

The two equations (2.139) and (2.140) can be rewritten as

$$\mathbf{c}^+(z_2) - S_{22}^a \mathbf{c}^-(z_2) = S_{21}^a \mathbf{c}^+(z_1), \quad (2.142)$$

$$- S_{11}^b \mathbf{c}^+(z_2) - \mathbf{c}^-(z_2) = S_{12}^b \mathbf{c}^-(z_3). \quad (2.143)$$

Now the solution of the two equations for $\mathbf{c}^+(z_2)$ and $\mathbf{c}^-(z_2)$ is sought. Thus one may write

$$S_{11}^b \mathbf{c}^+(z_2) - S_{11}^b S_{22}^a \mathbf{c}^-(z_2) = S_{11}^b S_{21}^a \mathbf{c}^+(z_1), \quad (2.144)$$

$$- S_{11}^b \mathbf{c}^+(z_2) - \mathbf{c}^-(z_2) = S_{12}^b \mathbf{c}^-(z_3). \quad (2.145)$$

The sum of the equations (2.144) and (2.145) gives

$$\mathbf{c}^-(z_2) [I - S_{11}^b S_{22}^a] = S_{11}^b S_{21}^a \mathbf{c}^+(z_1) + S_{12}^b \mathbf{c}^-(z_3), \quad (2.146)$$

or

$$\mathbf{c}^-(z_2) = (I - S_{11}^b S_{22}^a)^{-1} (S_{11}^b S_{21}^a \mathbf{c}^+(z_1) + S_{12}^b \mathbf{c}^-(z_3)). \quad (2.147)$$

On the other hand, the two equations (2.142) and (2.143) can be rewritten as

$$\mathbf{c}^+(z_2) - S_{22}^a \mathbf{c}^-(z_2) = S_{21}^a \mathbf{c}^+(z_1) \quad (2.148)$$

$$- S_{22}^a S_{11}^b \mathbf{c}^+(z_2) + S_{22}^a \mathbf{c}^-(z_2) = S_{22}^a S_{12}^b \mathbf{c}^-(z_3) \quad . \quad (2.149)$$

The sum of the equations (2.148) and (2.149) gives

$$\mathbf{c}^+(z_2) [I - S_{22}^a S_{11}^b] = S_{21}^a \mathbf{c}^+(z_1) + S_{22}^a S_{12}^b \mathbf{c}^-(z_3) \quad , \quad (2.150)$$

or

$$\mathbf{c}^+(z_2) = (I - S_{22}^a S_{11}^b)^{-1} (S_{21}^a \mathbf{c}^+(z_1) + S_{22}^a S_{12}^b \mathbf{c}^-(z_3)) \quad . \quad (2.151)$$

Thus the results (2.147) and (2.151) give the solutions for $\mathbf{c}^+(z_2)$ and $\mathbf{c}^-(z_2)$. Substituting $\mathbf{c}^-(z_2)$ given by (2.147) into (2.148), one obtains

$$\begin{aligned} \mathbf{c}^-(z_1) = S_{11}^a \mathbf{c}^+(z_1) + S_{12}^a [(I - S_{11}^b S_{22}^a)^{-1} (S_{11}^b S_{21}^a \mathbf{c}^+(z_1) \\ + S_{12}^b \mathbf{c}^-(z_3))] \quad , \end{aligned} \quad (2.152)$$

or

$$\begin{aligned} \mathbf{c}^-(z_1) = [S_{11}^a + S_{12}^a (I - S_{11}^b S_{22}^a)^{-1} S_{11}^b S_{21}^a] \mathbf{c}^+(z_1) + \\ S_{12}^a (I - S_{11}^b S_{22}^a)^{-1} S_{12}^b \mathbf{c}^-(z_3) \quad . \end{aligned} \quad (2.153)$$

Substituting $\mathbf{c}^+(z_2)$ given by (2.151) into (2.141), one obtains

$$\begin{aligned} \mathbf{c}^+(z_3) = S_{21}^b [(I - S_{22}^a S_{11}^b)^{-1} (S_{21}^a \mathbf{c}^+(z_1) + S_{22}^a S_{12}^b \mathbf{c}^-(z_3))] + \\ S_{22}^b \mathbf{c}^-(z_3) \quad , \end{aligned} \quad (2.154)$$

or

$$\begin{aligned} \mathbf{c}^+(z_3) = S_{21}^b (I - S_{22}^a S_{11}^b)^{-1} S_{21}^a \mathbf{c}^+(z_1) + \\ [S_{22}^b + S_{21}^b (I - S_{22}^a S_{11}^b)^{-1} S_{22}^a S_{12}^b] \mathbf{c}^-(z_3) \quad . \end{aligned} \quad (2.155)$$

Finally, the scattering relation for two combined cells is obtained as

$$\begin{bmatrix} \mathbf{c}^-(z_1) \\ \mathbf{c}^+(z_3) \end{bmatrix} = \begin{bmatrix} S_{11}^c & S_{12}^c \\ S_{21}^c & S_{22}^c \end{bmatrix} \begin{bmatrix} \mathbf{c}^+(z_1) \\ \mathbf{c}^-(z_3) \end{bmatrix} \quad , \quad (2.156)$$

where

$$S_{11}^c = S_{11}^a + S_{12}^a (I - S_{11}^b S_{22}^a)^{-1} S_{11}^b S_{21}^a \quad , \quad (2.157)$$

$$S_{12}^c = S_{12}^a (I - S_{11}^b S_{22}^a)^{-1} S_{12}^b \quad , \quad (2.158)$$

$$S_{21}^c = S_{21}^b (I - S_{11}^b S_{22}^a)^{-1} S_{21}^a \quad , \quad (2.159)$$

$$S_{22}^c = S_{22}^b + S_{21}^b (I - S_{11}^b S_{22}^a)^{-1} S_{22}^a S_{12}^b \quad . \quad (2.160)$$

Chapter 3

Approximate cylindrical model

3.1 Transformer model description

As an improvement of the simple two-dimensional parallel plate waveguide model, let us now model a transformer winding structure as a coaxial cylindrical waveguide where the inner conducting cylinder represents the iron core that conducts the magnetic flux and the outer conducting cylinder represents the wall of the transformer tank, as shown in Fig. 3.1. In between there is a set of conducting cylindrical rings (winding segments or turns) that are situated within a coaxial cylindrical waveguide. From Fig. 3.1, it is seen that the coaxial cylindrical model is well-suited for

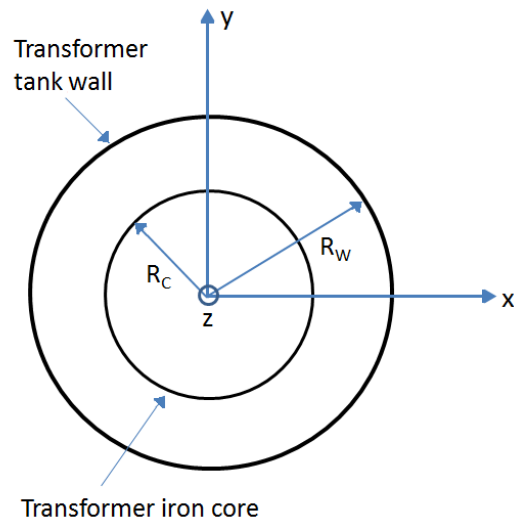


Figure 3.1: The power transformer as a coaxial cylindrical waveguide.

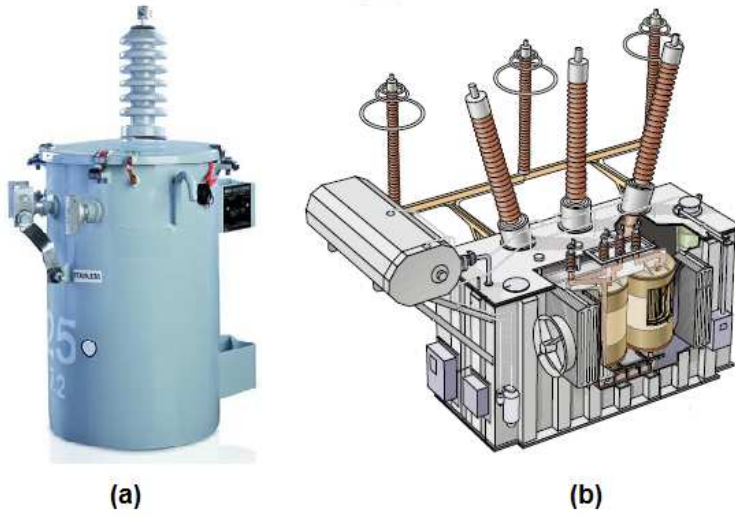


Figure 3.2: (a) Single-phase overhead distribution transformer [29]. (b) Three-phase power transformer [30].

some designs of practical power transformers. Such designs include for example the single-phase overhead (pole-mounted) distribution transformer that could be considered to actually resemble our ideal structure, as shown in Fig. 3.2(a). Furthermore, some large single-phase shunt reactors may also be considered to show a closer resemblance to our ideal structure. On the other hand, a large three-phase power transformer has a more complex mechanical structure as shown in Fig. 3.2(b). In these more complex transformers, the tank wall often does not possess a cylindrical symmetry. Furthermore, the tank wall (even if it has a suitable circular shape) does not encircle the entire core and windings.

More complex power transformers, as the one shown in Fig. 3.2(b), would require some modifications to the basic model depicted in Fig. 3.1. However, as the present model is the first step towards the establishing of the principles for the solution of the inverse electromagnetic problem at hand, a simple symmetric model is deliberately chosen, in order to avoid a high numerical calculation complexity and more advanced code optimization.

The approximate electromagnetic theory of a direct problem for a coaxial waveguide model, with a mathematical formalism that can effectively be reduced to the mathematical formalism used in the case of a two-dimensional parallel plate waveguide model from Chapter 2, is used as a theoretical basis for the study presented in Paper II.

3.2 TM waves in cylindrical waveguides

Consider a TM wave traveling in the z -direction, through a cylindrical waveguide [31] as shown in Fig. 2.2. Let us use (2.1) with the transverse nabla operator ∇_T in cylindrical coordinates:

$$\nabla_T = \mathbf{e}_r \frac{\partial}{\partial r} + \mathbf{e}_\phi \frac{1}{r} \frac{\partial}{\partial \phi} \quad . \quad (3.1)$$

Using (A.11) for progressive waves, one can write

$$E_z(r, \phi, z) = T(r, \phi) e^{-jk_z \cdot z} \quad . \quad (3.2)$$

In cylindrical coordinates, the equation for T becomes

$$\frac{1}{r} \frac{\partial}{\partial r} \left(r \frac{\partial T}{\partial r} \right) + \frac{1}{r^2} \frac{\partial^2 T}{\partial \phi^2} + k_T^2 T = 0 \quad . \quad (3.3)$$

Separating the variables, one can write

$$T(r, \phi) = R(r) \Phi(\phi) \quad , \quad (3.4)$$

such that

$$\frac{1}{r} \frac{d}{dr} \left(r \frac{dR}{dr} \right) \Phi + \frac{1}{r^2} \frac{d^2 \Phi}{d\phi^2} R = -k_T^2 R \Phi \quad , \quad (3.5)$$

or

$$\frac{1}{rR} \frac{d}{dr} \left(r \frac{dR}{dr} \right) + \frac{1}{r^2} \frac{1}{\Phi} \frac{d^2 \Phi}{d\phi^2} = -k_T^2 \quad , \quad (3.6)$$

or

$$\frac{r}{R} \frac{d}{dr} \left(r \frac{dR}{dr} \right) + k_T^2 r^2 = -\frac{1}{\Phi} \frac{d^2 \Phi}{d\phi^2} \quad . \quad (3.7)$$

Putting here

$$-\frac{1}{\Phi} \frac{d^2 \Phi}{d\phi^2} = k_\phi^2 \quad \implies \quad \frac{d^2 \Phi}{d\phi^2} + k_\phi^2 \Phi = 0 \quad , \quad (3.8)$$

with solutions

$$\Phi(\phi) = M \cos(k_\phi \cdot \phi) + N \sin(k_\phi \cdot \phi) \quad , \quad (3.9)$$

one obtains

$$r \frac{d}{dr} \left(r \frac{dR}{dr} \right) + (k_T^2 r^2 - k_\phi^2) R = 0 \quad . \quad (3.10)$$

Introducing here a new variable

$$u = k_T r \quad , \quad (3.11)$$

one obtains

$$u \frac{d}{du} \left(u \frac{dR}{du} \right) + (u^2 - k_\phi^2) R = 0 \quad . \quad (3.12)$$

This is a Bessel differential equation for cylindrical structures. The usual periodic boundary condition

$$\Phi(\phi + 2\pi) = \Phi(\phi) \quad , \quad (3.13)$$

is used. This requires $k_\phi = n$ ($n = 0, 1, 2, \dots$) to be an integer. Thus,

$$\Phi(\phi) = M \cos(n\phi) + N \sin(n\phi) \quad , \quad (3.14)$$

and

$$u \frac{d}{du} \left(u \frac{dR}{du} \right) + (u^2 - n^2) R = 0 \quad , \quad (3.15)$$

or

$$u^2 \frac{d^2 R}{du^2} + u \frac{dR}{du} + (u^2 - n^2) R = 0 \quad . \quad (3.16)$$

The general solution of this equation is

$$R(u) = P J_n(u) + Q N_n(u) \quad , \quad (3.17)$$

where $J_n(u)$ is the Bessel function of integer order, while $N_n(u)$ is the Neumann function of integer order.

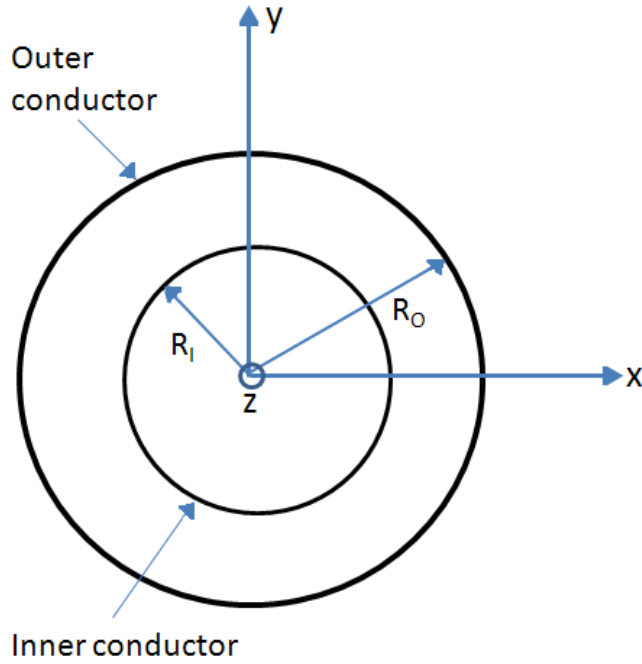


Figure 3.3: Cross section of a coaxial waveguide.

3.3 TM waves in a coaxial cylindrical waveguide

Consider the case of TM waves propagating between two coaxial cylinders, where $r = R_I$ is the radius of the inner cylinder and $r = R_O$ is the radius of the outer cylinder, as shown in Fig. 3.3. Using the results (3.14) and (3.17), the transverse function $T(r, \phi)$, suitable for the present geometry, can be constructed in the form [31]

$$T(r, \phi) = [P J_n(k_T r) + Q N_n(k_T r)] \cos n\phi \quad . \quad (3.18)$$

On the other hand, E_z is tangential to both conductor boundaries at $r = R_I$ and $r = R_O$ for any angle ϕ . Thus the boundary conditions for TM waves in a coaxial waveguide are the following

$$E_z(R_I, \phi, z) = 0 \quad , \quad E_z(R_O, \phi, z) = 0 \quad , \quad (3.19)$$

or

$$T(R_I, \phi) = 0 \quad , \quad T(R_O, \phi) = 0 \quad . \quad (3.20)$$

This implies

$$PJ_n(k_T R_I) + QN_n(k_T R_I) = 0 \quad , \quad (3.21)$$

and

$$PJ_n(k_T R_O) + QN_n(k_T R_O) = 0 \quad . \quad (3.22)$$

This requires

$$-\frac{Q}{P} = \frac{J_n(k_T R_I)}{N_n(k_T R_I)} = \frac{J_n(k_T R_O)}{N_n(k_T R_O)} \quad . \quad (3.23)$$

For $R_O - R_I$ small, i.e. for

$$R_O - R_I \ll \frac{R_O + R_I}{2} \quad , \quad (3.24)$$

the curvature effect on the field distribution is small and an approximate solution can be used [31]:

$$T(r, \phi) = \left[P \cos \frac{m\pi(r - R_I)}{R_O - R_I} + Q \sin \frac{m\pi(r - R_I)}{R_O - R_I} \right] \cos n\phi \quad . \quad (3.25)$$

As $T(R_I, \phi) = 0$ for TM waves, $P = 0$ is required such that

$$T_{m,n}(r, \phi) = Q \sin \left(\frac{m\pi(r - R_I)}{R_O - R_I} \right) \cos n\phi \quad , \quad (3.26)$$

and

$$k_{T(m,n)}^2 = \frac{m^2 \pi^2}{(R_O - R_I)^2} + \frac{4n^2}{(R_O + R_I)^2} \quad , \quad (3.27)$$

with

$$k_{z(m,n)} = \sqrt{k^2 - k_{T(m,n)}^2} = \sqrt{\omega^2 \mu \epsilon - k_{T(m,n)}^2} \quad , \quad (3.28)$$

or

$$k_{z(m,n)} = \sqrt{\omega^2 \mu \epsilon - \frac{m^2 \pi^2}{(R_O - R_I)^2} - \frac{4n^2}{(R_O + R_I)^2}} \quad . \quad (3.29)$$

Using now (A.38)-(A.39), one obtains for TM waves ($H_z = 0$)

$$\mathbf{H}_T = \frac{-j\omega\epsilon}{k_T^2} \mathbf{e}_z \times \nabla_T E_z \quad , \quad (3.30)$$

$$\mathbf{E}_T = \pm j \frac{k_z}{k_T^2} \nabla_T E_z \quad , \quad (3.31)$$

or

$$\mathbf{H}_T \propto \mathbf{e}_z \times \nabla_T E_z = -\mathbf{e}_r \frac{1}{r} \frac{\partial E_z}{\partial \phi} + \mathbf{e}_\phi \frac{\partial E_z}{\partial r} \quad , \quad (3.32)$$

$$\mathbf{E}_T \propto Z \nabla_T E_z = \mathbf{e}_r Z \frac{\partial E_z}{\partial r} + \mathbf{e}_\phi Z \frac{1}{r} \frac{\partial E_z}{\partial \phi} \quad , \quad (3.33)$$

or

$$H_r \propto -\frac{1}{r} \frac{\partial E_z}{\partial \phi} \propto -\frac{1}{r} \frac{\partial T}{\partial \phi} \quad , \quad H_\phi \propto \frac{\partial E_z}{\partial r} \propto \frac{\partial T}{\partial r} \quad , \quad (3.34)$$

$$E_r = Z H_\phi \propto Z \frac{\partial E_z}{\partial r} \propto Z \frac{\partial T}{\partial r} \quad , \quad E_\phi = -Z H_r \propto Z \frac{1}{r} \frac{\partial E_z}{\partial \phi} \propto Z \frac{1}{r} \frac{\partial T}{\partial \phi} \quad . \quad (3.35)$$

In the case of a symmetric structure with respect to ϕ , one can put $n = 0$ and consider the $\text{TM}_{m,0}$ -modes

$$E_r^{(m,0)}(r) \propto \cos \left[\frac{m\pi(r - R_I)}{R_O - R_I} \right] \quad , \quad (3.36)$$

$$H_\phi^{(m,n)}(r) \propto \cos \left[\frac{m\pi(r - R_I)}{R_O - R_I} \right] \quad , \quad (3.37)$$

while $E_\phi^{(m,0)} \equiv 0$ and $H_r^{(m,0)} \equiv 0$. Introducing here a new variable $\rho = r - R_I$, such that $0 < \rho < a$, where $a = R_O - R_I$, the set of orthonormal basis functions for TM_n -modes is introduced in the form

$$\psi_n = \sqrt{\frac{2 - \delta_{n,0}}{a}} \cos \left(\frac{n\pi\rho}{a} \right) \quad , \quad (3.38)$$

which satisfy the the orthonormality conditions

$$\langle \psi_n | \psi_k \rangle = \int_a^b \psi_n(r) \psi_k(r) dr = \delta_{nk} \quad , \quad (3.39)$$

with

$$k_{zn} = \sqrt{\omega^2 \mu \epsilon - \frac{n^2 \pi^2}{a^2}} \quad . \quad (3.40)$$

3.4 Approximate coaxial waveguide model

The geometry of the approximate model of a transformer winding surrounded by the transformer-tank wall and the magnetic core is shown in Fig. 3.4. The four regions (1-4) between the two cylindrical conductive surfaces of the coaxial waveguide (iron core and tank wall) and the conductive obstacle (winding segment or turn) are denoted as indicated. The basis functions in the regions 1 (below the conductive obstacle) and 2 (above the conductive obstacle), are then given by

$$\psi_n^{(1)}(x) = \sqrt{\frac{2 - \delta_{n,0}}{a_1}} \cos\left(\frac{n\pi\rho}{a_1}\right), \quad n = 0, 1, \dots \quad , \quad (3.41)$$

$$\psi_n^{(2)}(x) = \sqrt{\frac{2 - \delta_{n,0}}{a_2}} \cos\left[\frac{n\pi}{a_2}(a - \rho)\right], \quad n = 0, 1, \dots \quad , \quad (3.42)$$

while in the regions 3 and 4, with no obstacle present, the basis functions are equal to each other and given by

$$\psi_n^{(3)}(x) = \psi_n^{(4)}(x) = \sqrt{\frac{2 - \delta_{n,0}}{a}} \cos\left(\frac{n\pi\rho}{a}\right), \quad n = 0, 1, 2, \dots \quad . \quad (3.43)$$

Using the definition of the transverse wave number k_{Tn} in the lossless case, i.e. $k_{Tn}^2 = \omega^2 \mu \epsilon - k_{zn}^2$, where the longitudinal wave number for the n -th mode is denoted by k_{zn} , the longitudinal wave numbers $k_{zn}^{(i)}$ and the TM_n -mode impedances for the four regions ($i = 1, 2, 3, 4$) are given by

$$k_{zn}^{(i)2} = \omega^2 \mu \epsilon - k_{Tn}^{(i)2} = k^2 - \left(\frac{n\pi}{a_i}\right)^2 \quad , \quad (3.44)$$

$$Z_n^{(i)} = \frac{k_{zn}^{(i)}}{k} \eta \quad , \quad \eta = \sqrt{\frac{\mu}{\epsilon}} \quad . \quad (3.45)$$

integral using the definition formula

$$\langle \psi_{n_i}^{(i)}(\rho) | \psi_{n_j}^{(j)}(\rho) \rangle_i = \int_{I_i} \psi_{n_i}^{(i)}(\rho) \psi_{n_j}^{(j)}(\rho) d\rho \quad , \quad (3.48)$$

where I_i denotes the interval of integration for each of the regions. Using (3.48), the mode coupling matrix elements are defined by

$$K_{(i,j)n_i,n_j} = Z_{n_i}^{(i)} \langle \psi_{n_i}^{(i)}(\rho) | \psi_{n_j}^{(j)}(\rho) \rangle_i \quad . \quad (3.49)$$

They are collected into the mode coupling $\mathbf{K}_{(i,j)}$ -matrices, where

$$n_i = 0, 1, 2, \dots, N_i, \quad n_j = 0, 1, 2, \dots, N_j, \quad i = 1, 2, \quad j = 3, 4. \quad (3.50)$$

The definitions (3.50) indicate that any of the regions $i = 1, 2$ couples to any of the regions $j = 3, 4$. On the other hand, there is no coupling between regions 1 and 2 or between regions 3 and 4 respectively. The mode impedances in the four regions can also be collected into four diagonal impedance matrices as follows:

$$\mathbf{D}_{(i)} = \text{diag} \left\{ Z_n^{(i)} \right\}_{n=0}^{N_i} \quad . \quad (3.51)$$

Using the above notation, the boundary conditions result in the six matrix equations (2.69)-(2.74), where the vectors $\mathbf{c}_{(i)}^{\pm}(z)$ are defined by (2.82). The propagation equations for different modes and regions are summarized into the matrix equation (2.83), where a diagonal matrix (2.80) is introduced. Let us now consider the scattering of TM_n waves from the conductive obstacle depicted in Fig. 3.4. From the geometry of the problem, it is convenient to use the same number of modes at each side of the conductive obstacle, i.e. in the regions 3 and 4. Thus $N_3 = N_4 = N_0$ is assumed. Hereafter, the identical mode-matching technique as in Chapter 2 Eqs. (2.84)-(2.160) is used to calculate the scattering parameters.

Chapter 4

Elliptical perturbation model

In this chapter, the mechanical deformations where one or more winding segments (or turns) have been slightly deformed from the ideal circular form to an elliptic form, are studied using a first-order perturbation approach.

The first-order perturbation theory discussed in this chapter, applied to the approximate coaxial waveguide model described in Chapter 3, is used as a theoretical basis for the study presented in Paper III.

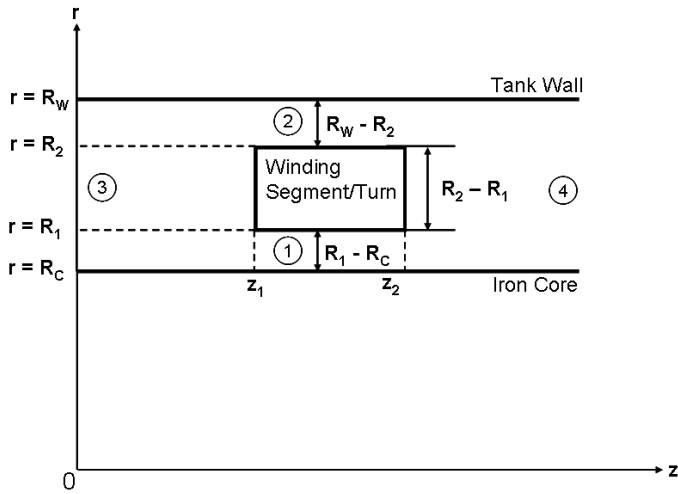


Figure 4.1: Cross section of a coaxial waveguide as a model of a transformer winding.

4.1 The unperturbed problem description

The model of a transformer winding structure as described in Section 3.4 is used. The relevant distances and regions is shown in Fig. 4.1. For the propagation problem, only TM modes ($H_z = 0$) are considered, as they include the TEM mode, which is the dominant mode in all regions. Following Section 3.3, the longitudinal component of the electric field is given by (3.2), for progressive waves traveling in the positive z -direction. The material parameters μ and ϵ are the effective permeability and permittivity, respectively, for the transformer winding insulation. An approximate solution of the scalar transverse equation for TM waves, suitable for our problem, is given by [31]:

$$T_{n,m}(r, \varphi) = Q \sin \frac{n\pi(r - R_I)}{R_O - R_I} \cos(m\varphi) = Q \sin \frac{n\pi\rho}{R_O - R_I} \cos(m\varphi) \quad , \quad (4.1)$$

with $\rho = r - R_I$ and

$$k_{T(n,m)}^2 = \frac{n^2\pi^2}{(R_O - R_I)^2} + \frac{4m^2}{(R_I + R_O)^2} \quad , \quad (4.2)$$

where $n = 1, 2, \dots$ and $m = 0, 1, 2, \dots$ are two integers that denote the TM modes in this case. In (4.1) and (4.2) the radii of the inner and outer cylinders of the coaxial waveguide are denoted by R_I and R_O respectively.

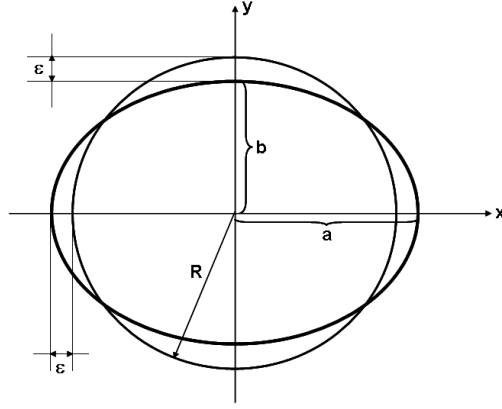
4.2 The first-order perturbation model

Let us now assume that the transformer winding segment (or turn) of radius R (equal to inner radius R_1 or outer radius R_2 according to Fig. 4.1 for regions 1 and 2 respectively) lying between the magnetic core of radius R_C and the transformer tank of radius R_W , is slightly deformed from the expected circular shape of radius R to an ellipse with semi-major axis a and semi-minor axis b . The ideal circular shape and the actual deformed elliptic shape of the transformer winding segment (or turn) are shown in Fig. 4.2.

From Fig. 4.2, to the first order of approximation in the small parameter ε/R , the following result is obtained for the size of the radial deformation $\delta(r, \varphi)$ of the elliptic winding compared to the unperturbed circular winding

$$\delta(r, \varphi) = \delta(\varphi) = r - R = \varepsilon \cos 2\varphi \quad . \quad (4.3)$$

From (4.3), it is seen that $a - R = +\varepsilon$ for the semi-major axis ($r = a$) when $\varphi = 0, \pi$ while $b - R = -\varepsilon$ for the semi-minor axis ($r = b$) when $\varphi = \pi/2, 3\pi/2$ in accordance with Fig. 4.2. Thus $a = R + \varepsilon$ and $b = R - \varepsilon$ such that, to the second order of approximation in the small parameter ε/R , the length of the perturbed

Figure 4.2: Elliptic deformation of the circular winding of radius R .

ellipse is given by

$$O = 2\pi R \left(1 + \frac{\varepsilon^2}{4R^2} \right) \approx 2\pi R \quad , \quad (4.4)$$

and up to the first order in the small parameter ε/R , the turn length of the perturbed winding is approximately equal to the turn length of the corresponding unperturbed winding. Following [32] (Problem 8.12), if the eigenvalue parameters and eigenfunctions of the transverse equation for two boundary contours C and C_0 are (k_T^2, T) and (k_{T0}^2, T_0) , respectively, then to the first order in $\delta(r, \varphi)$ one has for TM modes

$$k_T^2 - k_{T0}^2 = + \frac{\oint_{C_0} \delta(\varphi) \left| \frac{\partial T_0}{\partial n} \right|^2 dl_0}{\int_{S_0} |T_0(r, \varphi)|^2 dS_0} \quad , \quad (4.5)$$

where $\partial T / \partial n = \mathbf{n} \cdot \nabla T$ is the so-called normal derivative of T . In our case, the unperturbed transverse mode functions for TM modes are given by (4.1). Performing the integrations in (4.5), one obtains

$$k_T^2 - k_{T0}^2 = \frac{n^2 \pi^2}{(R_O - R_I)^2} \frac{\varepsilon}{R_O - R_I} \delta_{n,1} \quad , \quad (4.6)$$

where $\delta_{n,1}$ is the Cronecker delta function and should not be confused with our deformation parameter $\delta(r, \varphi)$ or $\delta(\varphi)$. Thus, to the first order of perturbation, only the TM modes with $m = 1$, i.e. TM_{m1} -modes, give a non-zero deviation of the eigenvalues k_T^2 from the unperturbed eigenvalue parameters k_{T0}^2 . Using now the result (4.2) with $m = 1$, the perturbed eigenvalue parameters k_T^2 are obtained in the form

$$k_{T(n,m)}^2 = \frac{n^2 \pi^2}{(R_O - R_I)^2} \left(1 + \frac{\varepsilon}{R_O - R_I} \right) + \frac{4}{(R_O + R_I)^2} \quad . \quad (4.7)$$

Thus, in the regions 1 and 2, as depicted in Fig. 4.1, the elliptic perturbation causes an effective decrease of R_1 and R_2 , i.e.

$$R'_1 = R_1 - \frac{\varepsilon}{2} \quad , \quad R'_2 = R_2 - \frac{\varepsilon}{2} \quad . \quad (4.8)$$

On the other hand, the radii of the magnetic core and the tank wall are not affected by the elliptic deformation of the winding segments (or turns). Thus in the regions 3 and 4, as depicted in Fig. 4.1, there are no effects of the elliptic perturbation and the unperturbed eigenfunctions and eigenvalue parameters can be used. Therefore, a new variable $\rho = r - R_C$ can be introduced, replacing the mode numbers $(n, 1)$ simply by (n) .

Following [32] [see e.g. (8.65)], the perturbed orthonormal basis functions are of the form

$$\psi(\rho, \varphi) \approx \psi_0 + \varepsilon \psi_1 = \psi_0 + \varepsilon \frac{\partial \psi_0}{\partial n} = \psi_0 + \varepsilon \frac{\partial \psi_0}{\partial \rho} \quad . \quad (4.9)$$

It is here convenient to introduce a dimensionless perturbation parameter λ as follows

$$\lambda = \frac{\varepsilon}{R_O - R_I} = \frac{\varepsilon}{A} \quad , \quad A = R_O - R_I \quad . \quad (4.10)$$

In order to be able to calculate the mode-coupling integrals (3.49) for the perturbed case, perturbed orthonormal basis functions as defined in (4.9) are required. However, rather than directly using (4.9), an ad-hoc choice of the perturbed orthonormal basis functions is made as being of the same mathematical form as their unperturbed counterparts, but with perturbed radii defined by (4.7) and (4.8). Thus, the perturbed orthonormal basis functions are chosen in the general form

$$\psi(\rho, \varphi) = Q \cos\left(\frac{n\pi\rho}{A'}\right) \cos \varphi \quad , \quad (4.11)$$

with $A' = R'_O - R_I$. As an example at this point, it is assumed that the perturbation occurs at the outer conductor with radius $r = R_O$. It is also possible to make the opposite assumption, i.e. that the perturbation occurs at the inner conductor with radius $r = R_I$, depending on the region in Fig. 4.1 that one wants to study. In order to justify the ad-hoc choice of perturbed orthonormal basis functions (4.11), one can use the result (4.7) to write

$$\frac{1}{A'} \approx \frac{1}{A} \left(1 + \frac{\varepsilon}{A}\right) = \frac{1}{A} (1 + \lambda) \quad . \quad (4.12)$$

Using (4.12) one can rewrite (4.11) as follows

$$\psi(\rho, \varphi) = Q \cos\left[\frac{n\pi\rho}{A} (1 + \lambda)\right] \cos \varphi \quad , \quad (4.13)$$

For $\lambda \ll 1$ and consequently $\cos(\lambda x) \approx 1$ and $\sin(\lambda x) \approx \lambda x$, the trigonometric formula

$$\cos(x + \lambda x) \approx \cos(x) - \lambda x \sin(x) \quad , \quad (4.14)$$

can be used with the condition that at the position of the perturbed outer conducting surface $r \approx R_O$, one has $\rho/A \approx 1$. Thus one obtains from (4.13)

$$\psi(\rho, \varphi) = Q \cos\left(\frac{n\pi\rho}{A}\right) \cos\varphi - \lambda A Q \frac{n\pi}{A} \sin\left(\frac{n\pi\rho}{A}\right) \cos\varphi \quad . \quad (4.15)$$

Using $\varepsilon = \lambda A$, one further obtains

$$\psi(\rho, \varphi) = Q \cos\left(\frac{n\pi\rho}{A}\right) \cos\varphi + \varepsilon \frac{\partial}{\partial\rho} \left[Q \cos\left(\frac{n\pi\rho}{A}\right) \cos\varphi \right] \quad , \quad (4.16)$$

or

$$\psi(\rho, \varphi) \approx \psi_0 + \varepsilon \frac{\partial\psi_0}{\partial\rho} \quad , \quad (4.17)$$

in agreement with the generic definition of the perturbed orthonormal basis functions (4.9). Thus it can be concluded that, at least in principle, the ad-hoc choice of perturbed orthonormal basis functions (4.11) is mathematically justified.

Let us now return to the study of the actual geometry of our problem, as depicted in Fig. 4.1. Following Paper II, the orthonormal basis functions for TM_{*n*}-modes (TM_{*n,1*}-modes) in the regions 1 (below the conductive obstacle) and 2 (above the conductive obstacle) are defined as follows

$$\psi_n^{(1)}(\rho, \varphi) = \sqrt{\frac{2 - \delta_{n,0}}{\pi(R'_1 - R_C)}} \cos\left(\frac{n\pi\rho}{(R'_1 - R_C)}\right) \cos\varphi \quad , \quad (4.18)$$

$$\psi_n^{(2)}(\rho, \varphi) = \sqrt{\frac{2 - \delta_{n,0}}{\pi(R_W - R'_2)}} \cos\left[\frac{n\pi}{\pi(R_W - R'_2)}(a - \rho)\right] \cos\varphi \quad , \quad (4.19)$$

while in the regions 3 and 4, with no obstacle present, the basis functions are equal to each other and given by

$$\psi_n^{(3)}(\rho, \varphi) = \psi_n^{(4)}(\rho, \varphi) = \sqrt{\frac{2 - \delta_{n,0}}{\pi(R_W - R_C)}} \cos\left(\frac{n\pi\rho}{(R_W - R_C)}\right) \cos\varphi \quad . \quad (4.20)$$

Here the definition of the transverse wave number k_{Tn} , i.e. $k_{Tn}^2 = \omega^2\mu\epsilon - k_{zn}^2$ is used, where the longitudinal wave number for the *n*-th mode is denoted by $k_{zn}^{(i)}$. Thus, the longitudinal wave numbers $k_{zn}^{(i)}$ and the TM_{*n*}-mode impedances $Z_n^{(i)}$ for the four regions (*i* = 1,2,3,4) can be written in the form

$$k_{zn}^{(i)2} = \omega^2\mu\epsilon - k_{Tn}^{(i)2} = k^2 - k_{Tn}^{(i)2} \quad , \quad (4.21)$$

$$Z_n^{(i)} = \frac{k_{zn}^{(i)}}{k} \eta \quad , \quad \eta = \sqrt{\frac{\mu}{\epsilon}} \quad . \quad (4.22)$$

4.3 Mode-matching in the perturbation model

The radial electric fields $E_{rn}^{(i)}$ and azimuthal magnetic fields $H_{\varphi n}^{(i)}$ are now linear combinations of the basis functions $\psi_n^{(i)}(\rho, \varphi)$ for the respective region. These transverse fields can be expanded, in terms of the basis functions, as follows [27]:

$$E_r^{(i)}(\rho, \varphi, z) = \sum_{n=0}^{\infty} \left[c_n^{(i)+}(z) + c_n^{(i)-}(z) \right] Z_n^{(i)} \psi_n^{(i)}(\rho, \varphi) , \quad (4.23)$$

$$H_{\varphi}^{(i)}(\rho, \varphi, z) = \sum_{n=0}^{\infty} \left[c_n^{(i)+}(z) - c_n^{(i)-}(z) \right] \psi_n^{(i)}(\rho, \varphi) , \quad (4.24)$$

where for each mode and each region $E_{rn}^{(i)} = Z_n^{(i)} H_{\varphi n}^{(i)}$, while $c_n^{(i)\pm}(z)$ are coefficients for modes propagating in $\pm z$ -direction. Hereafter, the identical mode-matching technique as in Section 3.4 starting from (3.47) is used to calculate the scattering parameters.

Chapter 5

Exact coaxial model with Bessel functions

In this chapter, the exact coaxial cylindrical model of a transformer winding structure, presented in Section 3.3, is considered without the thin-layer approximation (3.24). The exact electromagnetic theory of a direct problem for a coaxial waveguide model, with a mathematical formalism based on appropriate Bessel functions, is used as a theoretical basis for the study presented in Paper IV.

5.1 TM waves in a coaxial waveguide revisited

Consider the coaxial cylindrical model of a transformer winding structure, presented in Section 3.3. A general solution for the transverse function is given in terms of Bessel functions in the result (3.18). Thus the case of TM waves propagating between two coaxial cylinders is again considered, where $r = a$ is used to denote the radius of the inner cylinder and $r = b$ is used to denote the radius of the outer cylinder, respectively, as shown in Fig. 5.1.

Using now (3.23), i.e.

$$-\frac{Q}{P} = \frac{J_n(k_T a)}{N_n(k_T a)} = \frac{J_n(k_T b)}{N_n(k_T b)} \quad , \quad (5.1)$$

in (3.18), one obtains

$$T(r, \phi) = P \left[J_n(k_T r) - \frac{J_n(k_T a)}{N_n(k_T a)} N_0(k_T r) \right] \quad . \quad (5.2)$$

In case there is an axial symmetry, i.e. when the fields are independent on the angle ϕ , $n = 0$ can be chosen without loss of generality. Thus,

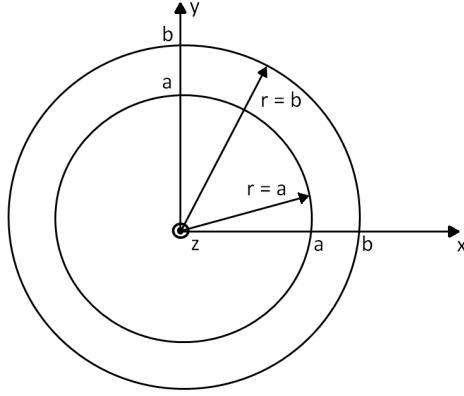


Figure 5.1: Cross section of a coaxial cylindrical waveguide.

$$T(r, \phi) = T(r) = P \left[J_0(k_T r) - \frac{J_0(k_T a)}{N_0(k_T a)} N_0(k_T r) \right] , \quad (5.3)$$

with

$$Z = \frac{1}{\omega \epsilon} \sqrt{\omega^2 \mu \epsilon - k_T^2} , \quad (5.4)$$

where the discrete set of values for k_T (k_{Tm}) is obtained from the cross-product condition (with $b = \lambda a$ and $\lambda > 1$) :

$$J_0(k_T a) N_0(\lambda k_T a) - J_0(\lambda k_T a) N_0(k_T a) = 0 . \quad (5.5)$$

Using now (3.34) and (3.35), one obtains

$$\begin{aligned} E_r &= -Z P e^{-j k_z z} \frac{d}{dr} \left[J_0(k_T r) - \frac{J_0(k_T a)}{N_0(k_T a)} N_0(k_T r) \right] = \\ &= -Z k_T P e^{-j k_z z} \left[J'_0(k_T r) - \frac{J_0(k_T a)}{N_0(k_T a)} N'_0(k_T r) \right] . \end{aligned} \quad (5.6)$$

Using now the formulae ($J'_0(w) = \frac{dJ_0}{dw}$, $N'_0(w) = \frac{dN_0}{dw}$)

$$J'_0(w) = -J_1(w) , \quad N'_0(w) = -N_1(w) , \quad (5.7)$$

one obtains

$$E_r^{(m)} = Zk_T P e^{-jk_z z} \left[J_1(k_T r) - \frac{J_0(k_T a)}{N_0(k_T a)} N_1(k_T r) \right] , \quad (5.8)$$

and

$$H_\phi^{(m)} = k_T P e^{-jk_z z} \left[J_1(k_T r) - \frac{J_0(k_T a)}{N_0(k_T a)} N_1(k_T r) \right] . \quad (5.9)$$

The condition (5.5) is treated in [33]. For $\lambda > 1$, the asymptotic expansion of the m -th zero is

$$k_{Tm} a = \beta + \frac{p}{\beta} + \frac{q - p}{\beta^3} + \frac{r - 4pq + 2p^3}{\beta^5} , \quad (5.10)$$

where

$$\beta = \frac{m\pi}{\lambda - 1} , \quad p = -\frac{1}{8\lambda} , \quad q = \frac{25(\lambda^3 - 1)}{6(4\lambda)^3(\lambda - 1)} , \quad \frac{-1073(\lambda^5 - 1)}{5(4\lambda)^5(\lambda - 1)} . \quad (5.11)$$

Thus one has the formula

$$\begin{aligned} k_{Tm} a = & \frac{m\pi}{\lambda - 1} - \frac{1}{8\lambda} \cdot \frac{\lambda - 1}{m\pi} + \left[\frac{25(\lambda^3 - 1)}{6(4\lambda)^3(\lambda - 1)} - \frac{1}{(8\lambda)^2} \right] \frac{(\lambda - 1)^3}{m^3 \pi^3} - \\ & - \left[\frac{1073(\lambda^5 - 1)}{5(4\lambda)^5(\lambda - 1)} - \frac{25(\lambda^3 - 1)}{12\lambda(4\lambda)^3(\lambda - 1)} + \frac{2}{(8\lambda)^3} \right] \frac{(\lambda - 1)^5}{m^5 \pi^5} . \end{aligned} \quad (5.12)$$

From the results for the transverse fields (5.8) and (5.9), it is seen that the suitable basis functions for $\text{TM}_{m,0}$ -modes (TM_m -modes) in the coaxial waveguide are

$$\psi_m(r) = A_m \left[J_1(k_{Tm} r) - \frac{J_0(k_{Tm} a)}{N_0(k_{Tm} a)} N_1(k_{Tm} r) \right] , \quad (5.13)$$

where $m = 1, 2, 3, \dots$ and A_m is a normalization constant, such that

$$\langle \psi_m | \psi_k \rangle = \int_a^b \psi_m(r) \psi_k(r) 2\pi r dr = \delta_{m,k} . \quad (5.14)$$

The normalization condition (5.14) requires that

$$A_m^2 \int_a^b \left[J_1(k_{Tm} r) - \frac{J_0(k_{Tm} a)}{N_0(k_{Tm} a)} N_1(k_{Tm} r) \right]^2 2\pi r dr = 1 . \quad (5.15)$$

In expanded form, the condition (5.15) can be rewritten as follows

$$A_m^2 \cdot \left[2\pi \int_a^b J_1^2(k_{Tm}r) r dr - 4\pi \frac{J_0(k_{Tm}a)}{N_0(k_{Tm}a)} \int_a^b J_1(k_{Tm}r) N_1(k_{Tm}r) r dr \right] + \\ + \left[2\pi \int_a^b \frac{J_0^2(k_{Tm}a)}{N_0^2(k_{Tm}a)} N_1^2(k_{Tm}r) r dr \right] = 1 \quad . \quad (5.16)$$

In order to solve the integrals in (5.16), the formulae (5.54) in [34] is used. Thus one has

$$I_1 = \int_a^b r J_1^2(k_{Tm}r) dr = \left\{ \frac{r^2}{2} [J_1^2(k_{Tm}r) - J_0(k_{Tm}r) J_2(k_{Tm}r)] \right\}_a^b = \\ = \frac{b^2}{2} [J_1^2(k_{Tm}b) - J_0(k_{Tm}b) J_2(k_{Tm}b)] - \frac{a^2}{2} [J_1^2(k_{Tm}a) - J_0(k_{Tm}a) J_2(k_{Tm}a)] \quad , \quad (5.17)$$

and

$$I_3 = \int_a^b r N_1^2(k_{Tm}r) dr = \left\{ \frac{r^2}{2} [N_1^2(k_{Tm}r) - N_0(k_{Tm}r) N_2(k_{Tm}r)] \right\}_a^b = \\ = \frac{b^2}{2} [N_1^2(k_{Tm}b) - N_0(k_{Tm}b) N_2(k_{Tm}b)] - \frac{a^2}{2} [N_1^2(k_{Tm}a) - N_0(k_{Tm}a) N_2(k_{Tm}a)] \quad . \quad (5.18)$$

The second integral in (5.16) can be calculated as follows using (2.1.10) in [35]

$$I_2 = \int_a^b r J_1(k_{Tm}r) N_1(k_{Tm}r) dr = \\ = \left[\frac{r}{2k_{Tm}} J_1(k_{Tm}r) N_0(k_{Tm}r) - J_0(k_{Tm}r) N_1(k_{Tm}r) \right]_a^b = \\ = \frac{b}{2k_{Tm}} [J_1(k_{Tm}b) N_0(k_{Tm}b) - J_0(k_{Tm}b) N_1(k_{Tm}b)] - \\ - \frac{a}{2k_{Tm}} [J_1(k_{Tm}a) N_0(k_{Tm}a) - J_0(k_{Tm}a) N_1(k_{Tm}a)] \quad . \quad (5.19)$$

Substituting (5.17)-(5.19) into (5.16), the normalization constant A_m can be calculated.

5.2 Mode-matching analysis in an axially symmetric cylindrical case

Consider a TM wave in a coaxial waveguide with a cylindrical conductive obstacle, as shown in Fig. 3.4. The four relevant regions between the coaxial waveguide boundaries and boundaries of the conductive obstacle are denoted as in Fig. 2.5. The basis functions in the regions 1 and 2 are given by

$$\psi_m^{(1)}(r) = A_m^{(1)} \left[J_1(k_{Tm}^{(1)}r) - \frac{J_0(k_{Tm}^{(1)}r_c)}{N_0(k_{Tm}^{(1)}r_c)} N_1(k_{Tm}^{(1)}r) \right] , \quad (5.20)$$

$$\psi_m^{(2)}(r) = A_m^{(2)} \left[J_1(k_{Tm}^{(2)}r) - \frac{J_0(k_{Tm}^{(2)}r_w)}{N_0(k_{Tm}^{(2)}r_w)} N_1(k_{Tm}^{(2)}r) \right] , \quad (5.21)$$

where by (5.12),

$$k_{Tm}^{(1)} = \left(\frac{m\pi}{\lambda_1 - 1} - \frac{1}{8\lambda_1} \cdot \frac{\lambda_1 - 1}{m\pi} + \dots \right) \frac{1}{a_1} , \quad \lambda_1 = 1 + \frac{a_1}{r_c} , \quad (5.22)$$

$$k_{Tm}^{(2)} = \left(\frac{m\pi}{\lambda_2 - 1} - \frac{1}{8\lambda_2} \cdot \frac{\lambda_2 - 1}{m\pi} + \dots \right) \frac{1}{a_2} , \quad \lambda_2 = \frac{r_c + a}{r_c + a - a_2} = \frac{r_w}{r_w - a_2} , \quad (5.23)$$

and $A_m^{(1)}$ and $A_m^{(2)}$ are given by (5.16) with (5.17)-(5.19), such that the boundaries are suitably chosen as follows:

$$\text{Region 1: } a \rightarrow r_c , \quad b \rightarrow r_c + a_1 = \lambda_1 r_c . \quad (5.24)$$

$$\text{Region 2: } a \rightarrow r_c + a - a_2 , \quad b \rightarrow r_c + a = \lambda_2(r_c + a - a_2) . \quad (5.25)$$

The boundary radius a in (5.16) should not be confused with the distance between the magnetic core r_c and the tank wall r_w defined in Fig. 3.4 as $a = r_w - r_c$.

In the regions 3 and 4 with no obstacle present, one has

$$\psi_m^{(3)}(r) = A_m^{(3)} \left[J_1(k_{Tm}^{(3)}r) - \frac{J_0(k_{Tm}^{(3)}r_c)}{N_0(k_{Tm}^{(3)}r_c)} N_1(k_{Tm}^{(3)}r) \right] , \quad (5.26)$$

$$\psi_m^{(4)}(r) = A_m^{(4)} \left[J_1(k_{Tm}^{(4)}r) - \frac{J_0(k_{Tm}^{(4)}r_c)}{N_0(k_{Tm}^{(4)}r_c)} N_1(k_{Tm}^{(4)}r) \right] , \quad (5.27)$$

with

$$k_{Tm}^{(3)} = k_{Tm}^{(4)} = \left(\frac{m\pi}{\lambda - 1} - \frac{1}{8\lambda} \cdot \frac{\lambda - 1}{m\pi} + \dots \right) \frac{1}{a} \quad , \quad \lambda = \frac{r_w}{r_c} \quad , \quad (5.28)$$

and

$$A_m^{(3)} = A_m^{(4)} \quad , \quad (5.29)$$

given by (5.16) with (5.17)-(5.19), such that the boundaries are

$$a \rightarrow r_c \quad , \quad b \rightarrow r_w \quad . \quad (5.30)$$

The impedances in each region are given by (A.50), i.e.

$$Z_m^{(i)} = \frac{1}{\omega\epsilon} \sqrt{\omega^2\mu\epsilon - k_{Tm}^{(i)2}} = \frac{k_{zm}^{(i)}}{\omega\epsilon} = \frac{k_{zm}^{(i)}}{k} \sqrt{\frac{\mu}{\epsilon}} \quad , \quad (5.31)$$

The transverse fields can now be expanded in terms of the basis functions into the following series

$$E_r^{(i)} = E_r^{(i)}(r, z) = \sum_{m=0}^{\infty} \left[c_m^{(i)+}(z) + c_m^{(i)-}(z) \right] Z_m^{(i)} \psi_m^{(i)}(r) \quad , \quad (5.32)$$

$$H_\phi^{(i)} = H^{(i)}(r, z) = \sum_{m=0}^{\infty} \left[c_m^{(i)+}(z) - c_m^{(i)-}(z) \right] \psi_m^{(i)}(r) \quad . \quad (5.33)$$

$$\text{with} \quad i = 1, 2, 3, 4 \quad \text{and} \quad m = 1, 2, 3, 4, \dots \quad . \quad (5.34)$$

Next, the boundary conditions at the planes $z = z_1$ and $z = z_2$ are considered. The electric field $\mathbf{E} = E_r \mathbf{e}_r$ is tangential to the plane $z = z_1$, and the boundary conditions in the plane $z = z_1$ indicate that the electric field is continuous over that boundary, i.e.

$$E_T(z_1-) = E_T(z_1+) \quad \Rightarrow \quad E(z_1-) = E(z_1+) \quad . \quad (5.35)$$

Since $\mathbf{E} = 0$ inside the conductive material of the obstacle, the electric field \mathbf{E}

vanishes at the metallic part of the plane $z = z_1$. Thus one can write

$$\begin{aligned}
 & \sum_{m=0}^{\infty} \left[c_m^{(3)+}(z_1) + c_m^{(3)-}(z_1) \right] Z_m^{(3)} \psi_m^{(3)}(r) = \\
 & = \begin{cases} \sum_{m=0}^{\infty} \left[c_m^{(1)+}(z_1) + c_m^{(1)-}(z_1) \right] Z_m^{(1)} \psi_m^{(1)}(r) & , \quad r_c < r < r_c + a_1 \\ 0 & , \quad r_c + a_1 < r < r_w - a_2 \\ \sum_{m=0}^{\infty} \left[c_m^{(2)+}(z_1) + c_m^{(2)-}(z_1) \right] Z_m^{(2)} \psi_m^{(2)}(x) & , \quad r_w - a_2 < r < r_w \end{cases} .
 \end{aligned} \tag{5.36}$$

In addition the magnetic field is continuous over the apertures, such that

$$\begin{aligned}
 & \sum_{m=0}^{\infty} \left[c_m^{(3)+}(z_1) - c_m^{(3)-}(z_1) \right] \psi_m^{(3)}(r) = \\
 & = \begin{cases} \sum_{m=0}^{\infty} \left[c_m^{(1)+}(z_1) - c_m^{(1)-}(z_1) \right] \psi_m^{(1)}(r) & , \quad r_c < r < r_c + a_1 \\ \sum_{m=0}^{\infty} \left[c_m^{(2)+}(z_1) - c_m^{(2)-}(z_1) \right] \psi_m^{(2)}(r) & , \quad r_w - a_2 < r < r_w \end{cases} .
 \end{aligned} \tag{5.37}$$

Multiplying the boundary condition for the electric field (5.36) by $\psi_{m_3}^{(3)}(r)$, where m_3 is a specific value of the coefficient m , and integrating over the interval $r_c < r < r_w$, one obtains

$$\begin{aligned}
 & \sum_{m=0}^{\infty} \left[c_m^{(3)+}(z_1) + c_m^{(3)-}(z_1) \right] Z_m^{(3)} \langle \psi_{m_3}^{(3)}(r) | \psi_m^{(3)}(r) \rangle = \\
 & = \sum_{m=0}^{\infty} \left[c_m^{(3)+}(z_1) + c_m^{(3)-}(z_1) \right] Z_m^{(3)} \delta_{m_3, m} = \left[c_{m_3}^{(3)+}(z_1) + c_{m_3}^{(3)-}(z_1) \right] Z_{m_3}^{(3)} = \\
 & = \sum_{m=0}^{\infty} \left[c_m^{(1)+}(z_1) + c_m^{(1)-}(z_1) \right] Z_m^{(1)} \int_{r_c}^{r_c + a_1} 2\pi r \psi_{m_3}^{(3)}(r) \psi_m^{(1)}(r) dr + \\
 & + \sum_{m=0}^{\infty} \left[c_m^{(2)+}(z_1) + c_m^{(2)-}(z_1) \right] Z_m^{(2)} \int_{r_w - a_2}^{r_w} 2\pi r \psi_{m_3}^{(3)}(r) \psi_m^{(2)}(r) dr \quad .
 \end{aligned} \tag{5.38}$$

Introducing here the notation

$$\langle \psi_{m_3}^{(3)}(r) | \psi_m^{(1)}(r) \rangle_1 = \int_{r_c}^{r_c+a_1} 2\pi r \psi_{m_3}^{(3)}(r) \psi_m^{(1)}(r) dr \quad , \quad (5.39)$$

$$\langle \psi_{m_3}^{(3)}(r) | \psi_m^{(2)}(r) \rangle_2 = \int_{r_w-a_2}^{r_w} 2\pi r \psi_{m_3}^{(3)}(r) \psi_m^{(2)}(r) dr \quad , \quad (5.40)$$

one obtains

$$\begin{aligned} \left[c_{m_3}^{(3)+}(z_1) + c_{m_3}^{(3)-}(z_1) \right] Z_{m_3}^{(3)} &= \sum_{m=0}^{\infty} \left[c_m^{(1)+}(z_1) + c_m^{(1)-}(z_1) \right] Z_m^{(1)} \langle \psi_{m_3}^{(3)}(r) | \psi_m^{(1)}(r) \rangle_1 + \\ &+ \sum_{m=0}^{\infty} \left[c_m^{(2)+}(z_1) + c_m^{(2)-}(z_1) \right] Z_m^{(2)} \langle \psi_{m_3}^{(3)}(r) | \psi_m^{(2)}(r) \rangle_2 \quad . \end{aligned} \quad (5.41)$$

Next by multiplying the boundary condition for the magnetic field (5.37) by $Z_{m_1}^{(1)} \psi_{m_1}^{(1)}(r)$, where m_1 is a specific value of the coefficient m , and integrating over the interval $r_c < r < r_c + a_1$, one obtains

$$\begin{aligned} \sum_{n=0}^{\infty} \left[c_m^{(3)+}(z_1) - c_m^{(3)-}(z_1) \right] Z_{m_1}^{(1)} \int_{r_c}^{r_c+a_1} 2\pi r \psi_{m_1}^{(1)}(r) \psi_m^{(3)}(r) dr = \\ = \sum_{m=0}^{\infty} \left[c_m^{(1)+}(z_1) - c_m^{(1)-}(z_1) \right] Z_{m_1}^{(1)} \int_{r_c}^{r_c+a_1} 2\pi r \psi_{m_1}^{(1)}(r) \psi_m^{(1)}(r) dr \quad . \end{aligned} \quad (5.42)$$

Here,

$$\langle \psi_{m_1}^{(1)}(r) | \psi_m^{(3)}(r) \rangle_1 = \int_{r_c}^{r_c+a_1} 2\pi r \psi_{m_1}^{(1)}(r) \psi_m^{(3)}(r) dr \quad , \quad (5.43)$$

$$\langle \psi_{m_1}^{(1)}(r) | \psi_m^{(1)}(r) \rangle_1 = \int_{r_c}^{r_c+a_1} 2\pi r \psi_{m_1}^{(1)}(r) \psi_m^{(1)}(r) dr = \delta_{m_1, m} \quad , \quad (5.44)$$

such that

$$\sum_{m=0}^{\infty} \left[c_m^{(3)+}(z_1) - c_m^{(3)-}(z_1) \right] Z_{m_1}^{(1)} \langle \psi_{m_1}^{(1)}(r) | \psi_m^{(3)}(r) \rangle_1 =$$

$$= \sum_{m=0}^{\infty} \left[c_m^{(1)+}(z_1) - c_m^{(1)-}(z_1) \right] Z_{m_1}^{(1)} \delta_{m_1, m} \quad , \quad (5.45)$$

or

$$\begin{aligned} & \left[c_{m_1}^{(1)+}(z_1) - c_{m_1}^{(1)-}(z_1) \right] Z_{m_1}^{(1)} = \\ & = \sum_{m=0}^{\infty} \left[c_m^{(3)+}(z_1) - c_m^{(3)-}(z_1) \right] Z_{m_1}^{(1)} \langle \psi_{m_1}^{(1)}(r) | \psi_m^{(3)}(r) \rangle_1 \quad , \end{aligned} \quad (5.46)$$

Finally by multiplying the boundary condition for the magnetic field (5.37) by $Z_{m_2}^{(2)} \psi_{m_1}^{(1)}(r)$, where m_2 is a specific value of the coefficient m , and integrating over the interval $r_w - a_2 < r < r_w$, one obtains

$$\begin{aligned} & \sum_{m=0}^{\infty} \left[c_m^{(3)+}(z_1) - c_m^{(3)-}(z_1) \right] Z_{m_2}^{(2)} \int_{r_w - a_2}^{r_w} 2\pi r \psi_{m_2}^{(2)}(r) \psi_m^{(3)}(r) dr = \\ & = \sum_{m=0}^{\infty} \left[c_m^{(2)+}(z_1) - c_m^{(2)-}(z_1) \right] Z_{m_2}^{(2)} \int_{r_w - a_2}^{r_w} 2\pi r \psi_{m_2}^{(2)}(r) \psi_m^{(2)}(r) dr \quad . \end{aligned} \quad (5.47)$$

Here,

$$\langle \psi_{m_2}^{(2)}(r) | \psi_m^{(3)}(r) \rangle_2 = \int_{r_w - a_2}^{r_w} 2\pi r \psi_{m_2}^{(2)}(r) \psi_m^{(3)}(r) dr \quad , \quad (5.48)$$

$$\langle \psi_{m_2}^{(2)}(r) | \psi_m^{(2)}(r) \rangle_2 = \int_{r_w - a_2}^{r_w} 2\pi r \psi_{m_2}^{(2)}(r) \psi_m^{(2)}(r) dr = \delta_{m_2, m} \quad , \quad (5.49)$$

such that

$$\begin{aligned} & \sum_{m=0}^{\infty} \left[c_m^{(3)+}(z_1) - c_m^{(3)-}(z_1) \right] Z_{m_2}^{(2)} \langle \psi_{m_2}^{(2)}(r) | \psi_m^{(3)}(r) \rangle_2 = \\ & = \sum_{m=0}^{\infty} \left[c_m^{(2)+}(z_1) - c_m^{(2)-}(z_1) \right] Z_{m_2}^{(2)} \delta_{m_2, m} \quad . \end{aligned} \quad (5.50)$$

or

$$\left[c_{m_2}^{(2)+}(z_1) - c_{m_2}^{(2)-}(z_1) \right] Z_{m_2}^{(2)} =$$

$$= \sum_{m=0}^{\infty} \left[c_m^{(3)+}(z_1) - c_m^{(3)-}(z_1) \right] Z_{m_2}^{(2)} \langle \psi_{m_2}^{(2)}(r) | \psi_m^{(3)}(r) \rangle_2 \quad . \quad (5.51)$$

Collecting together equations (5.41), (5.46) and (5.51) the complete set of boundary conditions at the plane $z = z_1$ is obtained in the form

$$\begin{aligned} Z_{m_3}^{(3)} \left[c_{m_3}^{(3)+}(z_1) + c_{m_3}^{(3)-}(z_1) \right] &= \sum_{m=0}^{\infty} \left[c_m^{(1)+}(z_1) + c_m^{(1)-}(z_1) \right] Z_m^{(1)} \langle \psi_{m_3}^{(3)}(r) | \psi_m^{(1)}(r) \rangle_1 + \\ &+ \sum_{m=0}^{\infty} \left[c_m^{(2)+}(z_1) + c_m^{(2)-}(z_1) \right] Z_m^{(2)} \langle \psi_{m_3}^{(3)}(r) | \psi_m^{(2)}(r) \rangle_2 \quad , \end{aligned} \quad (5.52)$$

$$\begin{aligned} &Z_{m_1}^{(1)} \left[c_{m_1}^{(1)+}(z_1) - c_{m_1}^{(1)-}(z_1) \right] = \\ &= \sum_{m=0}^{\infty} \left[c_m^{(3)+}(z_1) - c_m^{(3)-}(z_1) \right] Z_{m_1}^{(1)} \langle \psi_{m_1}^{(1)}(r) | \psi_m^{(3)}(r) \rangle_1 \quad , \end{aligned} \quad (5.53)$$

$$\begin{aligned} &Z_{m_2}^{(2)} \left[c_{m_2}^{(2)+}(z_1) - c_{m_2}^{(2)-}(z_1) \right] = \\ &= \sum_{m=0}^{\infty} \left[c_m^{(3)+}(z_1) - c_m^{(3)-}(z_1) \right] Z_{m_2}^{(2)} \langle \psi_{m_2}^{(2)}(r) | \psi_m^{(3)}(r) \rangle_2 \quad . \end{aligned} \quad (5.54)$$

By means of an analogous procedure in the boundary plane $z = z_2$, it is easily shown that the corresponding complete set of boundary conditions at the plane $z = z_2$ has the form

$$\begin{aligned} Z_{m_4}^{(4)} \left[c_{m_4}^{(4)+}(z_2) + c_{m_4}^{(4)-}(z_2) \right] &= \sum_{m=0}^{\infty} \left[c_m^{(1)+}(z_2) + c_m^{(1)-}(z_2) \right] Z_m^{(1)} \langle \psi_{m_4}^{(4)}(r) | \psi_m^{(1)}(r) \rangle_1 + \\ &+ \sum_{m=0}^{\infty} \left[c_m^{(2)+}(z_2) + c_m^{(2)-}(z_2) \right] Z_m^{(2)} \langle \psi_{m_4}^{(4)}(r) | \psi_m^{(2)}(r) \rangle_2 \quad , \end{aligned} \quad (5.55)$$

$$\begin{aligned} &Z_{m_1}^{(1)} \left[c_{m_1}^{(1)+}(z_2) - c_{m_1}^{(1)-}(z_2) \right] = \\ &= \sum_{m=0}^{\infty} \left[c_m^{(4)+}(z_2) - c_m^{(4)-}(z_2) \right] Z_{m_1}^{(1)} \langle \psi_{m_1}^{(1)}(r) | \psi_m^{(4)}(r) \rangle_1 \quad , \end{aligned} \quad (5.56)$$

$$\begin{aligned}
 & Z_{m_2}^{(2)} \left[c_{m_2}^{(2)+}(z_2) - c_{m_2}^{(2)-}(z_2) \right] = \\
 & = \sum_{m=0}^{\infty} \left[c_m^{(4)+}(z_2) - c_m^{(4)-}(z_2) \right] Z_{m_2}^{(2)} \langle \psi_{m_2}^{(2)}(r) | \psi_m^{(4)}(r) \rangle_2 \quad . \quad (5.57)
 \end{aligned}$$

The six equations (5.52)-(5.57) are the matrix equations for the mode coefficients at the boundaries $z = z_1$ and $z = z_2$. For the numerical implementation, each set of modes must be truncated to the finite number of M_i ($i = 1, 2, 3, 4$) lowest modes. The mode coefficients can then be collected into finite-dimensional vectors of the form described in (2.57)-(2.62). The matrix elements $\langle \psi_{m_i}^{(i)}(r) | \psi_{m_j}^{(j)}(r) \rangle_i$ are calculated using the definition formula

$$\langle \psi_{m_i}^{(i)}(r) | \psi_{m_j}^{(j)}(r) \rangle_i = \int_{I_i} \psi_{m_i}^{(i)}(r) \psi_{m_j}^{(j)}(r) 2\pi r dr \quad , \quad (5.58)$$

where I_i denotes the interval of integration for each of the regions. For example for region 1, $I_1 = [r_c, r_c + a_1]$. From the explicit results (5.20)-(5.21) and (5.26)-(5.27), it is seen that the matrix elements (5.58) are of the following form

$$\langle \psi_{m_i}^{(i)} | \psi_{m_j}^{(j)} \rangle = A_{m_i}^{(i)} A_{m_j}^{(j)} \times \int_{I_i} \left[J_1(k_{Tm_i}^{(i)} r) - \frac{J_0(k_{Tm_i}^{(i)} r_i)}{N_0(k_{Tm_i}^{(i)} r_i)} N_1(k_{Tm_i}^{(i)} r) \right] \times$$

$$\left[J_1(k_{Tm_j}^{(j)} r) - \frac{J_0(k_{Tm_j}^{(j)} r_j)}{N_0(k_{Tm_j}^{(j)} r_j)} N_1(k_{Tm_j}^{(j)} r) \right] 2\pi r dr =$$

$$A_{m_i}^{(i)} A_{m_j}^{(j)} \times \left[\int_{I_i} J_1(k_{Tm_i}^{(i)} r) J_1(k_{Tm_j}^{(j)} r) 2\pi r dr - \right.$$

$$\left. \frac{J_0(k_{Tm_i}^{(i)} r_i)}{N_0(k_{Tm_i}^{(i)} r_i)} \int_{I_i} N_1(k_{Tm_i}^{(i)} r) J_1(k_{Tm_j}^{(j)} r) 2\pi r dr - \right.$$

$$\left. - \frac{J_0(k_{Tm_j}^{(j)} r_j)}{N_0(k_{Tm_j}^{(j)} r_j)} \int_{I_i} J_1(k_{Tm_i}^{(i)} r) N_1(k_{Tm_j}^{(j)} r) 2\pi r dr + \right.$$

$$\frac{J_0(k_{Tm_i}^{(i)} r_i)}{N_0(k_{Tm_i}^{(i)} r_i)} \frac{J_0(k_{Tm_j}^{(j)} r_j)}{N_0(k_{Tm_j}^{(j)} r_j)} \int_{I_i} N_1(k_{Tm_i}^{(i)} r) N_1(k_{Tm_j}^{(j)} r) 2\pi r dr \Big] \quad . \quad (5.59)$$

where r_i and r_j are the limiting radii of I_i and I_j . In order to calculate the integrals in (5.59), the formula (5.54) in [34] can be used to write down three general integrals

$$I_{JJ} = \int J_1(\alpha r) J_1(\beta r) 2\pi r dr =$$

$$\frac{2\pi r}{\alpha^2 - \beta^2} [\beta J_1(\alpha r) J_0(\beta r) - \alpha J_0(\alpha r) J_1(\beta r)] \quad , \quad (5.60)$$

$$I_{NN} = \int N_1(\alpha r) N_1(\beta r) 2\pi r dr =$$

$$\frac{2\pi r}{\alpha^2 - \beta^2} [\beta N_1(\alpha r) N_0(\beta r) - \alpha N_0(\alpha r) N_1(\beta r)] \quad , \quad (5.61)$$

$$I_{JN} = \int J_1(\alpha r) N_1(\beta r) 2\pi r dr =$$

$$\frac{2\pi r}{\alpha^2 - \beta^2} [\beta J_1(\alpha r) N_0(\beta r) - \alpha J_0(\alpha r) N_1(\beta r)] \quad , \quad (5.62)$$

where in all three results (5.60)-(5.62), $\alpha \neq \beta$ is assumed. These three general indefinite integrals

$$I_{JJ}(\alpha, \beta, r) \quad , \quad I_{NN}(\alpha, \beta, r) \quad , \quad I_{JN}(\alpha, \beta, r) \quad , \quad (5.63)$$

can be used for numerical evaluation of the matrix elements (5.59).

Using now the matrix notation (2.57)-(2.62), the six equations (5.52)-(5.57) can be rewritten in the well-known form of (2.69)-(2.72). Hereafter, the identical mode-matching technique as in Chapter 2 Eqs. (2.75)-(2.160) is used to calculate the scattering parameters.

Chapter 6

Results and interpretation

6.1 Optimization principles

In the present thesis, the inverse problem is solved by means of an optimization method. Generally speaking, the optimization methods may be classified into local or global methods. An extensive list of publications with various optimization methods can be found in [36]. Local methods, although effective in terms of convergence speed, generally require a 'domain knowledge', since for nonlinear and multi-minima optimization functions the initial trial solution must lie in the so-called 'attraction basin' of the global solution to avoid the convergence solution being trapped into local minima (i.e. wrong solutions of the problem at hand).

In contrast, global methods with stochastic algorithms are potentially able to find the global optimum of the functional whatever the initial point(s) of the search. Regarding the choice of the optimization method, it is important that the optimization algorithm is efficient enough such that the best possible agreement between the theoretically obtained scattering data and corresponding measured scattering data is obtained. In other words, the optimization method must provide for a correct reconstruction of the target geometry.

6.2 Parallel-plate model

Present optimization method

The computer simulation geometry of our two-dimensional transformer winding model is shown in Fig. 6.1. The transformer is modeled as a two-dimensional parallel plate waveguide, where the upper plate represents the wall of the transformer tank and the lower plate represents the iron core that conducts the magnetic flux. In the present thesis, the principles are investigated, such that the chosen dimensions do not mimic any particular realistic transformer. The inverse problem at hand is to determine the studied parameters $\mathbf{x} = (x_1, x_2, \dots, x_n)$ and it is based on

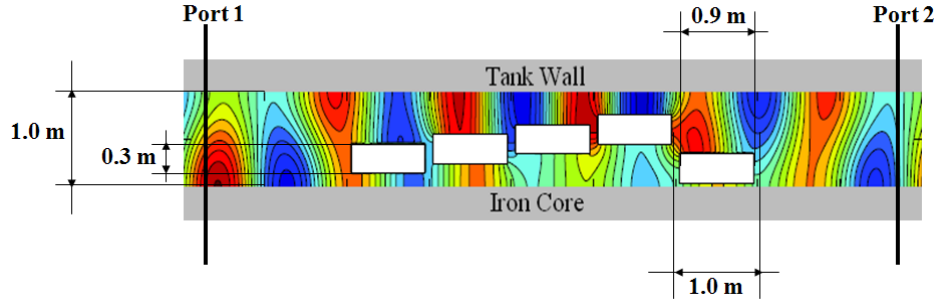


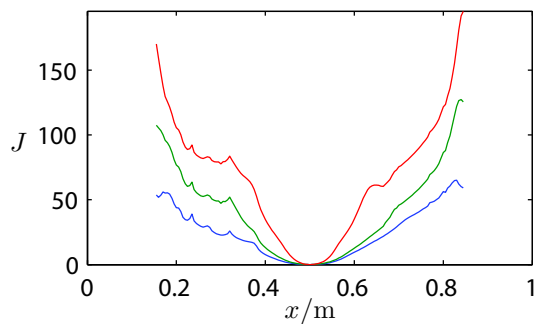
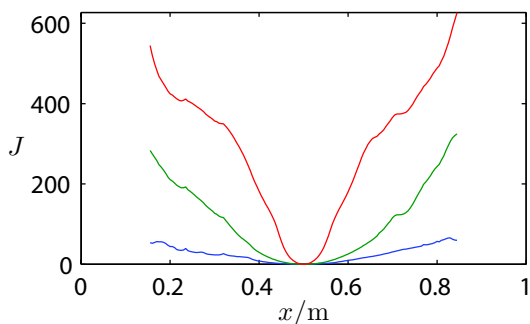
Figure 6.1: The computer simulation geometry with a distance between the tank wall and iron core $a = 1$ m and five winding cells each of length $\Delta z = 1$ m. The colors indicate the magnitude of the resulting magnetic field when the dominant TEM mode of frequency $f = 200$ MHz is incident from the left (Paper I).

minimizing the optimization function J , defined by

$$J(\mathbf{x}) = \sum_{i,j} |S_{ij}^{\text{calc}}(\mathbf{x}) - S_{ij}^{\text{meas}}|^2, \quad (6.1)$$

where $S_{ij}^{\text{calc}}(\mathbf{x})$ are the elements of the calculated scattering matrix and S_{ij}^{meas} are the corresponding elements of the measured scattering matrix. With this choice of the optimization function J , the position of the dislocated windings can be determined by solving the optimization problem.

Two graphs of the one-parameter optimization functions J are shown in Figs. 6.2 and 6.3. The graphs, computed and displayed using MATLAB, are obtained when the middle conductor (see Fig. 6.1) is moved in the vertical direction. However, similar results are obtained when any other of the conductors is moved in the vertical direction. The global minimum (here zero, due to the perfect model) is attained at the correct position of the middle conductor. The scattering matrix is calculated in the frequency range $2 \text{ MHz} \leq f \leq f_{\text{max}}$ in steps of 2 MHz up to the maximum frequencies $f_{\text{max}} = 150$ MHz (blue line), $f_{\text{max}} = 300$ MHz (green line) and $f_{\text{max}} = 400$ MHz (red line). The graph in Fig. 6.2 is obtained when the scattering data are obtained from the dominant (TEM = TM_0) mode only. The graph in Fig. 6.3 is obtained using the dominant mode, the first higher mode (starting to propagate at $f = 150$ MHz) and the second higher mode (starting to propagate at $f = 300$ MHz). The blue curves in both graphs are identical, since in that case only the dominant mode propagates in the waveguide model. In Figs. 6.2 and 6.3 it is seen that as the frequency region expands upward, the global minimum becomes narrower, which means reduced sensitivity to measurement errors. Comparing the two graphs, it is also seen that if scattering data is retrieved from all modes which can propagate in the frequency area (Fig. 6.3) rather than just the dominant mode (Fig. 6.2), the number of local minima of the J function is reduced. In both cases,

Figure 6.2: J -functions with the dominant TM mode only (Paper II).Figure 6.3: J -functions including the first three modes (Paper II).

local minima occur some distance away from the global minimum. Thus a good initial guess, which lies in the global well can make a local optimization method converge towards the global minimum.

After the one-parameter study, described above, an algorithm was developed to minimize $J(\mathbf{x})$ with respect to variation of all the conductor locations instead of just one. Initially, the multi-parameter algorithm was developed for one frequency at a time in order to limit the computation time.

In order to minimize $J(\mathbf{x})$ with respect to variation of multiple conductor locations, a modified steepest-descent optimization method was developed where first the gradient of J is computed, and then a minimum of the function is sought by stepping from an initial guess \mathbf{x}_0 in the direction of the negative of the gradient. The method is programmed to be quasi-genetic, so that if a specified number of iterations is exceeded and the gradient of J , as well as J itself have not simultaneously reached values sufficiently close to zero, the algorithm restarts itself with a new initial guess. All restarts are saved, and the one with the lowest J -value is printed. The model can in general handle any number of conductor cells (Paper I).

The initial guesses are chosen randomly by the computer based on the parallel plate waveguide geometry, such that they are within the waveguide. If the algorithm fails to obtain the J -value lower than the predefined target value after a predefined number of iterations (15 times the number of cells), the calculations are aborted and a new run of the algorithm is initiated. In each new run, the computer randomly selects a new set of initial guesses around the previous initial guesses. The number of reruns of the algorithm is limited to the number of cells. Thus the maximum allowed number of iterations is equal to $N_{max} = 15 \times N_{cells}^2$. In the case presented in Tables 6.2 with 10 conductors (i.e. 10 cells) the maximum allowed number of iterations is $N_{max} = 15 \times 10^2 = 1500$, while in the case presented in Tables 6.1 and 6.3 with 5 conductors (i.e. 5 cells) the maximum allowed number of iterations is $N_{max} = 15 \times 5^2 = 375$. For these runs, the target value of J was set relatively low and the actual numbers of iterations were in fact equal to the maximum number of iterations specified above. After performing the maximum number of iterations without reaching the target value of J , the algorithm returns the reconstruction results with the best value of J among the performed N_{cells} reruns as the final result of the optimization procedure.

HFSS setup

In order to avoid the inverse crime [37], the optimization model was tested by comparing the calculated scattering data with synthetic measurement data generated using the commercial program ANSYS High Frequency Structure Simulator (HFSS) Version 15. HFSS is an industry-standard simulation tool for three-dimensional full-wave electromagnetic simulations [38]. The software is based on three-dimensional full-wave frequency domain Finite Element Method (FEM) to calculate the electromagnetic behavior of a model. In this section, the implementation of the parallel-plate model in HFSS will be detailed. An overview of the parallel-plate model in HFSS is shown in Fig. 6.4. In order to perform the calculations in HFSS, first a solution type must be set for the model. HFSS allows three solution type options: Driven Modal, Driven Terminal and Eigenmode. For a scattering problem which is excited by a plane wave, the Driven Modal solution type should be used. Then, the rectangular winding conductors are drawn, as well as a box surrounding them. The conductor locations shown in the example of Fig. 6.4 are displaced in the same way as in Fig. 6.1, and the waveguide structure is directed in the z -direction. After this, material parameters of the objects are assigned (i.e. perfect electric conductors for the winding conductors and vacuum in the surrounding region of the box). In order to simulate a parallel-plate structure (infinite in the y and z directions), perfect magnetic conductor (PMC) boundaries are set on the two sides which lie in the xz -plane, while perfect electric conductor (PEC) boundaries are set on the two sides which lie above and below the conductors in the yz -plane. After drawing the model, assigning materials and setting the boundaries, the excitation source of the model must be defined. An incident plane wave is assigned, and since one has a waveguide model at hand, the Waveguide Port option is chosen in HFSS. The

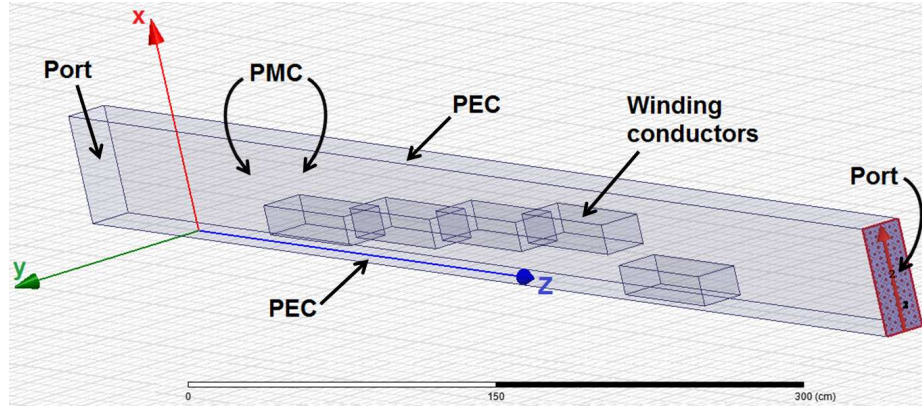


Figure 6.4: Overview of the parallel-plate model in HFSS.

waveguide ports are placed on each side of the winding conductors in the xy -plane, as shown in Fig. 6.4. The mode polarity is set manually via integration lines. In Fig. 6.4, the integration line is shown by the red arrow at the center of the port. When using waveguide ports in HFSS, any number of modes may be set. In our investigations however, the cases of (a) dominant mode only, (b) the dominant mode and first higher order mode, and (c) the dominant mode and the first two higher order modes were mainly used. Now, in order to calculate the S -parameters, the model was solved for several frequencies. A frequency band of 2 MHz to 400 MHz in steps of 2 MHz was swept. The accuracy was increased as much as possible while the simulation was time efficient, such that the numerical error is small. Finally, the S -parameters were exported directly to MATLAB .m files as matrix data in real/imaginary form. These matrices were then used directly in the optimization algorithm.

Optimization results

In Table 6.1, the results for reconstructing the positions of the 5 cells in Fig. 6.1 are shown. The three lowest modes are used at $f = 150$ MHz. In the optimization model, a partially randomized offset matrix has been added to S , corresponding to about 20% of the mean value of S .

In Table 6.2, a reconstruction of ten cells is shown. The three lowest modes are used at $f = 150$ MHz and the added offset is 10% of the mean value of S . Although the results obtained for ten cells are relatively accurate, it is noted that as the cell number increases, it is likely that more modes and a wider frequency band are needed to ensure a good optimization accuracy.

The optimization model is also tested using synthetic measurement data from HFSS. The results of the reconstruction using HFSS synthetic measurement data,

for $f = 250$ MHz, are shown in Table 6.3.

Conductor	1	2	3	4	5
True \mathbf{x} value	0.3000	0.4000	0.5000	0.6000	0.2000
Computed \mathbf{x} value	0.2994	0.3985	0.5028	0.5979	0.2000

Table 6.1: Case of 5 cell positions, with 20% offset at $f = 150$ MHz (Paper II).

Conductor	1	2	3	4	5
True \mathbf{x} value	0.3000	0.4000	0.5000	0.6000	0.2000
Computed \mathbf{x} value	0.3024	0.3935	0.4941	0.6019	0.1996

Conductor	6	7	8	9	10
True \mathbf{x} value	0.3000	0.7000	0.6000	0.5000	0.7000
Computed \mathbf{x} value	0.2986	0.7056	0.6106	0.4972	0.6994

Table 6.2: Case of 10 cell positions, with 10% offset at $f = 150$ MHz (Paper II).

Conductor	1	2	3	4	5
True \mathbf{x} value	0.3000	0.4000	0.5000	0.6000	0.2000
Computed \mathbf{x} value	0.2627	0.4382	0.5354	0.6101	0.1943

Table 6.3: Case of 5 cell positions, using HFSS data at $f = 250$ MHz (Paper II).

Thus, the inverse electromagnetic problem is solved for several winding configurations using an optimization procedure. From a parametric study of the optimization function, an agreement is found between the theory and measured data. It is also found that wide-band data may stabilize reconstructions and that information from multiple modes is likely to decrease the occurrence of local minima. Hence, it is important that several waveguide modes can be transmitted and received with high accuracy, which implies that many antennas are needed in the measurement system.

However, the present optimization algorithm is sensitive to the choice of the initial guess and easily stops at the local minima. Furthermore, difficulties were experienced in performing the multi-parameter algorithm with HFSS-data. This may be a consequence of the choice to run the algorithm with one frequency at the time, as discussed above. Expanding the algorithm to sweep over a wide band of frequencies may be a way to remedy these difficulties.

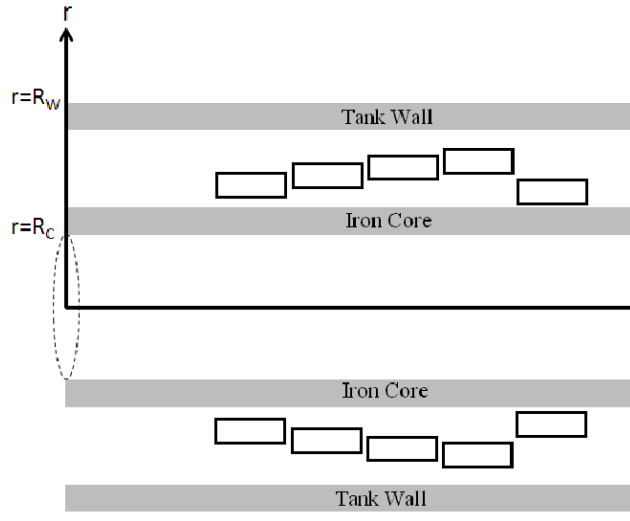


Figure 6.5: Effective problem geometry (Paper IV).

6.3 Approximate coaxial model

The geometry of the coaxial waveguide model of the power transformer winding structure is shown in Fig. 6.5. The geometry of the model is such that the transformer winding structure is surrounded by the transformer-tank wall and the magnetic core. The approximate analysis in the present section is based on the assumption that $R_W - R_C$ is small compared to the mean radius of the coaxial wave guide $(R_C + R_W)/2$. Although this assumption is generally not applicable to realistic power transformers, where $R_W - R_C$ can amount to 30 - 40 percent of the mean radius of the coaxial waveguide $(R_C + R_W)/2$, the approximate analysis discussed here can be considered as reasonably good, given the fact that the very model of coaxial cylindrical waveguide is approximate in the first place.

From the direct problem analysis described in Section 6.2 above, it is readily seen that the approximate cylindrical model is effectively reduced to the two-dimensional parallel-plate model discussed in the previous section. The rectangular coordinate x is simply replaced by the relative radial coordinate $\rho = r - R_I$. This is valid for the winding deformations that possess the axial symmetry as the ones assumed in the present section. Thus the numerical results presented in e.g. Tables 6.1, 6.2 and 6.3 above, remain valid in the approximate cylindrical model discussed here.

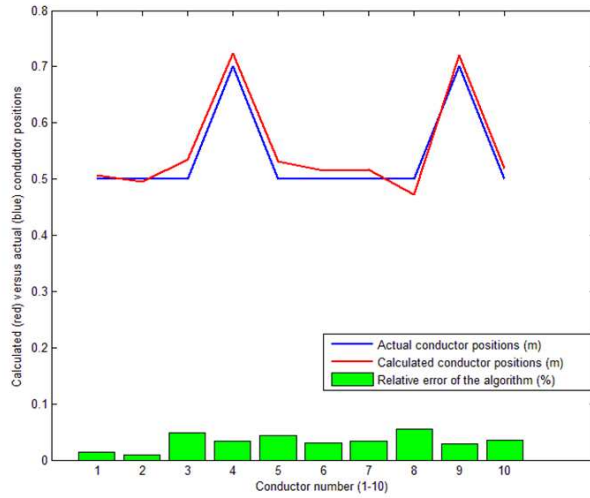


Figure 6.6: Calculated (red) versus actual (blue) conductor positions for the case of ten conductor cells at $f = 250$ MHz (Paper III).

6.4 Elliptic perturbation model

The geometry of the transformer winding model is shown in Fig. 6.5, where it is noted that the elliptic deformations are equivalent to the corresponding radial extensions of winding segments or turns, as shown in Fig. 6.5.

The inverse problem to determine the studied parameters $\mathbf{x} = (\rho_1, \rho_2, \dots, \rho_n)$ is based on minimizing the optimization function J , defined by (6.1). In the present section, the studied parameters are the radial positions of the winding segments that reflect the elliptic deformations.

The optimization model is tested by comparing our calculated scattering data with synthetic measurement data generated from the commercial program HFSS. Here, a case of reconstruction of 10 conductors is presented, where two of the conductors are subject to elliptic deviations. The results are shown in Fig. 6.6, where good reconstruction results are obtained for the effective winding positions that reflect the corresponding elliptic deformations.

6.5 Exact coaxial model with Bessel functions.

Optimization principles

In the present section, the transformer is modeled in the same way as described in Section 6.3. The studied parameters are the radial positions of the winding

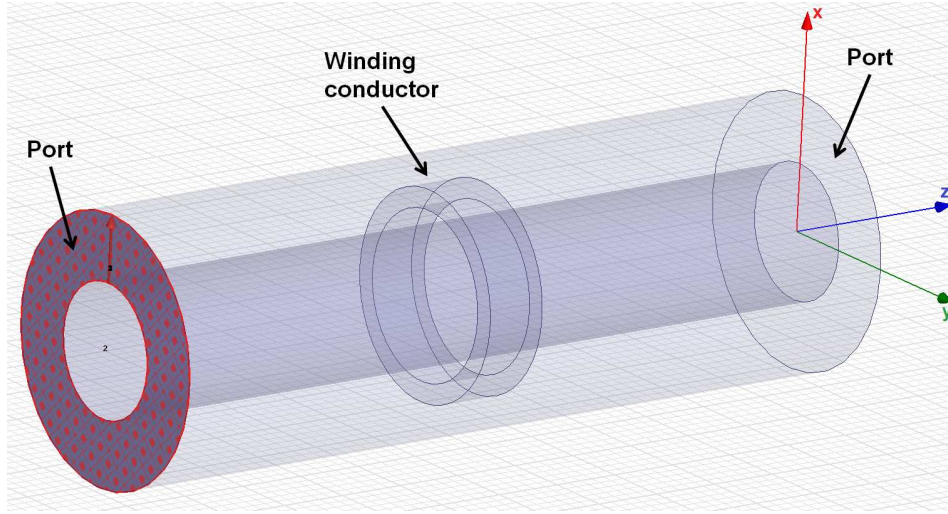


Figure 6.7: Overview of the coaxial model in HFSS.

segments. A multi-parameter steepest-descent optimization algorithm aiming to minimize $J(\mathbf{x})$ with respect to variation of all radial conductor positions is developed. The algorithm presented in this section is similar to the one described in Section 6.2, with the improvement that it can sweep over a range of frequencies.

HFSS setup

An overview of the exact coaxial model in HFSS is shown in Fig. 6.7. The coaxial structure is in the z -direction. The solution type used is Driven Modal. A plane wave is excited from two waveguide ports set in the xy -plane at each end of the coaxial structure. One port with mode polarity line is shown in Fig. 6.7.

The cases of (a) dominant mode only, (b) the dominant mode and first higher order mode, and (c) the dominant mode and the first two higher order modes were studied. The S -parameters were calculated for several frequencies using HFSS. A frequency band of 200 MHz to 4 GHz in steps of 100 MHz was swept. Finally, the solution data was exported in real/imaginary form to MATLAB .m matrix data, used directly in the optimization algorithm.

Optimization results

The results of the comparison of our calculated scattering data with the HFSS synthetic measurement data, for $f = 1200$ MHz, are shown in Table 6.4. From the results shown in Table 6.4, it is seen that in this case there is a good agreement between the theory and the HFSS data. Unfortunately, the present optimization

Conductor	1	2	3
True x value	1.5000	1.6000	1.7000
Computed x value	1.4912	1.6472	1.6627

Table 6.4: Case of 3 cell positions, using HFSS data at $f = 1200$ MHz (Paper IV).

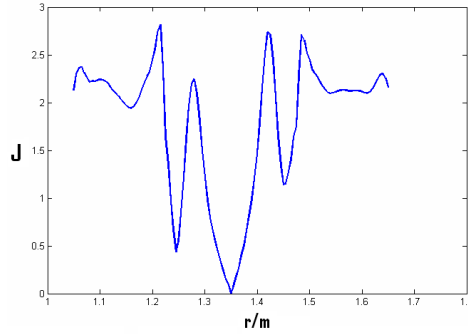


Figure 6.8: J -function for the proper coaxial model (Paper IV).

method with Bessel functions is very sensitive to the choice of the initial guess and likely to stop at the local minima. In order to illustrate the differences compared to the parallel-plate waveguide model, one can consider a single-cell optimization and compare the examples of J -functions from the parallel-plate waveguide model (Fig. 6.2) with an example of a J -function from the proper coaxial waveguide model presented in this section (Fig. 6.8). In both figures, the global minimum is obtained at the correct position of the middle conductor. In the parallel-plate waveguide model, it is seen that the local minima occurred some distance away from the global minimum. In the coaxial waveguide model presented here, this is not easy. In Fig. 6.8, it is noted that the local minima are very distinct and give deeper wells such that the use of the same (or slightly modified) optimization algorithm as the one used in Section 6.2 easily tends to detect spurious local minima. In some cases of the coaxial waveguide model, a wider global well could be found, while in many practical cases the occurrence of very close local minima effectively prevented a reliable optimization.

Chapter 7

Conclusions and future work

In the present thesis, the main goal was to perform a theoretical and numerical study of a proposed system for reconstruction of the power transformer winding geometry based on results of measurements of the scattered microwave radiation emitted by a number of antennas inserted on both sides of the winding package. The proposed measurement system is conceived as a set of antennas that alternately emit and receive the electromagnetic radiation in the microwave range of frequencies. The measured scattered microwaves are then used to determine the geometry of the scatterer structure, i.e. in our case the power transformer winding structure. Despite this idealization in our model, with a favorable deployment of microwave antennas and certain empirical corrections, our method may provide an accurate and stable diagnosis of mechanical deformations of transformer windings even in the more mechanically complex cases.

The inverse problem presented in the present thesis in Papers I - IV, is based on microwave tomography and solved using an optimization technique. The method is based on local optimization. A model of the transformer geometry (e.g. two-dimensional parallel-plate model or coaxial model etc.) is chosen and an initial guess of the transformer winding geometry is used to calculate the expected scattered microwaves. The calculated scattering data is then compared to the actual measured scattering data, whereby a suitable cost function is defined. Such a cost function is minimized by an optimization method, where the winding geometry is updated and the optimization procedure is repeated until a sufficient agreement with the measured scattering data is obtained.

An important issue is whether the global minimum is sufficiently "narrow" since a broad and flat global minimum allows for relatively large deviations in the reconstructed geometry from the actual physical geometry. This in turn makes the method very sensitive for measurement errors (both random and systematic) in the measured scattering data. The main challenge for an optimization method is the occurrence of local minima of the cost function. With a large number of local minima of the cost function, the optimization method can easily end up in a lo-

cal minimum point and largely deviate from the global minimum, thus giving an erroneous reconstruction of the target geometry.

The work presented in this thesis was an initial theoretical study of the possibilities to develop a monitoring method for deformations of the power transformer winding. No actual transformer structures were built and no actual measurements have been made so far. The optimization method was therefore primarily tested by comparing our calculated scattering data with the corresponding synthetic measurement data from the commercial program HFSS, in order to avoid the inverse crime.

An optimization algorithm was developed to minimize the cost function $J(\mathbf{x})$ with respect to variation of the locations of a number of winding segments (or turns). Our multi-parameter algorithm was initially developed in Papers I and II and used in Paper III for one frequency at a time only, in order to limit the computation times. Later on in Paper IV, the method was generalized such that it could sweep over several frequencies.

The method itself is a modified steepest-descent optimization method where the gradient of the cost function is computed, and then a minimum of the function is sought by stepping from an initial guess in the direction of the negative of the gradient. The developed method was programmed to be quasi-genetic, so that if the maximum number of iterations is exceeded and the gradient of the cost function has not reached a value near zero, the algorithm restarts itself with a new initial guess. All restarts are saved, and the one with the lowest value of the cost function is printed.

In the previous chapter, a number of optimization results from Papers I - IV was presented. From these results, it is seen that the optimization method developed so far does provide a reasonable accuracy for reconstructions of a number of target winding geometries. However, from the graphs of some one-dimensional cost functions presented in Figs. 6.2 and 6.3 from Paper II and in particular in Fig. 6.8 from Paper IV, it is immediately seen that the cost functions in the studied models generally have a large number of distinct local minima.

This property of the studied cost functions makes the optimization algorithms developed so far not sufficiently reliable for use in e.g. a commercial power transformer monitoring tool. The reason for such an assessment is the observed frequency of erroneous detection of the local minima instead of the actual global minimum during the development and testing of the present algorithm.

In particular for the exact solution with Bessel functions in the case of the coaxial waveguide model, presented in Paper IV, the occurrence of very close and distinct local minima effectively prevented a reliable optimization with the presently used optimization algorithm in many cases. This indicates that further efforts are needed to reduce the stochastic behavior of the cost function and develop a more robust algorithm. Other efficient optimization methods can be considered to improve efficiency and accuracy of the calculations (e.g. the method of conjugate gradients based on the quadratic polynomial fit of the cost function, genetic algorithms, etc).

Another possible way forward is to study continuous winding models, as op-

posed to the discrete winding model used in the present thesis. In such models, a power transformer winding can be viewed as a continuous metallic structure with deformations described by means of suitable continuous functions. In such a way, the perturbation theory for waveguide conductor boundaries can be used and the computation complexity can be reduced. Such an initial study has been presented in Paper VI.

The abovementioned conclusions open for two possible paths for future work. One is a continued effort to test some new more efficient and stable optimization algorithms in the discrete model of the transformer winding structure. The other is a deeper investigation of the continuous winding models as described above.

Bibliography

- [1] M. Wang, A. J. Vandermaar and K.D. Srivastava, "Review of Condition Assessment of Power Transformers in Service", Feature Article, IEEE Electrical Insulation Magazine, Vol. 18, No. 6, pp. 12 - 25, November/December 2002.
- [2] S. Tenbohlen, D. Uhde, J. Poittevin, H. Borsi, P. Werle, U. Sundermann and H. Matthes, "Enhanced Diagnosis of Power Transformers using On- and Off-line Methods: Results, Examples and Future Trends", Cigre, Session 2000, Paper 12-204 (2000)
- [3] "Transformer" (technical drawing), Wikimedia Foundation Inc., viewed 1 August 2013,
http://commons.wikimedia.org/wiki/File:Transformer3d_col3.svg.
- [4] Atlanta Electricals Pvt. Ltd., "Process", open access information, viewed 1 August 2013, <http://www.atlantaelectricals.com/process.htm>.
- [5] D. L. Harris, "The Design and Performance of Circular Disc, Helical and Layer Windings for Power Transformer Applications", Minnesota Power Systems Conference, University of Minnesota, Brooklyn Park Minneapolis, November 3-5 2009.
- [6] Å. Carlson, "Power Transformer Design Fundamentals", ABB Transformers, Ludvika (1995).
- [7] IEC 60076-5:2000(E) International Standard, "Power transformers - Part 5: Ability to withstand short circuit", International Electrotechnical Commission (IEC), 2000.
- [8] M. Duval, "A review of faults detectable by gas-in-oil analysis in transformers", IEEE Electrical Insulation Magazine, Vol. 18, No. 3, pp. 8 - 17, 2002.
- [9] L. E. Lundgaard, "Partial Discharge Detection - Part XIII Acoustic Partial Discharge Detection - Fundamental Considerations", IEEE Electrical Insulation Magazine, Vol. 8, No. 4, pp. 25 - 31, 1992.

- [10] M. D. Judd, L. Yang and B. B. I. Hunter, "Partial Discharge Monitoring for Power Transformers Using UHF Sensors Part 1: Sensors and Signal Interpretation", *IEEE Electrical Insulation Magazine*, Vol. 21, No. 2, pp. 5 - 14, 2005.
- [11] M. D. Judd, L. Yang and B. B. I. Hunter, "Partial Discharge Monitoring for Power Transformers Using UHF Sensors Part 2: field experience", *IEEE Electrical Insulation Magazine*, Vol. 21, No. 3, pp. 5 - 13, 2005.
- [12] T. Bengtsson, H. Kols and B. Jönsson, "Transformer PD Diagnosis using Acoustic Emission Technique", *10th International Symposium On High Voltage Engineering (ISH)*, Vol. 4, pp. 115-118, 1997.
- [13] R. Myska and P. Drexler, "Simulation and Verification of Methods for Partial Discharge Source Localization", *PIERS 2012 Proceedings*, Kuala Lumpur, Malaysia, March 27-30, pp. 704-708, 2012.
- [14] N. Abeywickrama, Y. V. Serdyuk and S. M. Gubanski, "High-Frequency Modeling of Power Transformers for Use in Frequency Response Analysis (FRA)", *IEEE Trans. On Power Delivery*, Vol. 23, No. 4, pp. 2042 - 2049, 2008.
- [15] H. Tavakoli, "An FRA Transformer Model with Application on Time Domain Reflectometry", *Ph.D. Thesis*, KTH Royal Institute of Technology, Sweden (2011).
- [16] L. Yanming, L. Gang, Z. Linhai, Z. Longjun and L. Zhiming, "Transformer Winding Deformation Diagnosis Using Middle Band Frequency Response Analysis", *2007 International Conference on Solid Dielectrics*, pp. 677 - 680, Winchester, UK, July 8-13 2007.
- [17] A. Shintemirov, W. Tang and Q. H. Wu, "Modeling of a Power Transformer Winding for Deformation Detection Based on Frequency Response Analysis", *Proceedings of the 26th Chinese Control Conference*, July 26-31, 2007, Zhangjiajie, Hunan, China, pp. 506 - 510, 2007.
- [18] U. Gäfvert, "Influence of geometric structure and material properties on dielectric frequency response of composite oil cellulose insulation", *International Symposium On Electrical Insulating Materials*, Vol. 1, pp. 73 - 76, 2005.
- [19] E. A. Mackenzie, J. Crossey, A. de Pablo and W. Ferguson, "On-line monitoring and diagnostics for power transformers", *Electrical Insulation (ISEI), Conference Record of the 2010 IEEE International Symposium*, pp. 1 - 5, San Diego, CA, 6-9 June 2010.
- [20] Y. Shao, Z. Rao and Z. Jin, "Online State Diagnosis of Transformer Windings Based on Time-frequency Analysis", *WSEAS Transactions on Circuits and Systems*, Issue 2, Volume 8, pp. 227 - 236, February 2009.

- [21] A. C. Monteith and C.F. Wagner, "Electrical Transmission and Distribution Reference Book 4th Edition", Westinghouse Electric Corporation, Pennsylvania, USA (1964).
- [22] Z. D. Wang, S. N. Hettiwatte and P. A. Crossley, "A measurements-based discharge location algorithm for plain disc winding power transformers", IEEE Transactions on Dielectric Insulation, Vol. 12, No. 3, pp. 416 - 422, 2005.
- [23] J. A. Brandão Faria, "High-frequency behavior of power inductor windings using an accurate multiconductor transmission line mode: Input impedance evaluation", European Transactions of Electric Power, Vol. 18, pp. 476 - 493, 2008.
- [24] S. M. Hassan Hosseini, M. Vakilian and G. B. Gharehtatian, "Comparison of transformer detailed models for fast and very fast transient studies", IEEE Transactions on Power Delivery, Vol. 23, Issue 2, pp. 733 - 741, 2008.
- [25] M. A. Hejazi, M. Choopani, M.Dabir, and G. B. Gharehpetian, "Effect of antenna position on on-line monitoring of transformer winding axial displacement using electromagnetic waves", 2nd IEEE International Conference on Power and Energy (PECon '08), pp. 44 - 49, Johor Baharu, Malaysia, December 1-3 2008.
- [26] D. Colton and R. Kress, "Inverse Acoustic and Electromagnetic Scattering Theory", Springer, Berlin (1992).
- [27] P. H. Masterman and P. J. B. Clarricoats, "Computer Field-Matching Solution of Waveguide Transverse Discontinuities", IEEE Proceedings, Vol. 118, pp. 51 - 63, 1971.
- [28] D. K. Cheng, "Field and Wave Electromagnetics", Addison-Wesley, Reading Massachusetts (1989).
- [29] Figure modified from open Internet Marketing Presentation by ABB Corporation: "Single phase overhead (polemounted) distribution transformers", courtesy of ABB Corporation.
- [30] Figure modified from open Marketing Materials by ABB Corporation: "Liquid-filled power transformers", courtesy of ABB Corporation.
- [31] S. A. Schelkunoff, "Electromagnetic Waves", D. Van Nostrand Company, Inc., New York (1943).
- [32] J. D. Jackson, "Classical Electrodynamics", Third Edition, Wiley, New York (1999).
- [33] M. Abramowitz and I. A. Stegun, "Handbook of Mathematical Functions", p. 374, US Dept of Commerce, National Bureau of Standards, Applied Mathematics Series 55, Washington D.C. (1964).

- [34] I. S. Gradshteyn and I. M. Ryzhik, "Tables of Integrals, Series and Products", p. 634, Fourth Edition, Academic Press, New York (1980).
- [35] W. Rosenheinrich, "Tables of some indefinite integrals of Bessel Functions", p. 142, University of Applied Sciences Jena, Jena, Germany (2013).
- [36] P. Rocca, G. Oliveri, and A. Massa, "Differential Evolution as Applied to Electromagnetics", IEEE Antennas and Propagation Magazine, Vol. 53, pp. 38 - 49, 2011.
- [37] D. Colton and R. Kress, "Integral Equation Methods in Scattering Theory", Wiley, New York, (1983).
- [38] "ANSYS - Simulation Driven Product Development", www.ansys.com.

Appendix A

General waveguide theory

Consider a hollow waveguide in the z -direction of arbitrary cross-sectional shape as shown in Fig. 2.2. The sinusoidal time dependence ($e^{j\omega t}$) and no sources of the field inside the waveguide ($\rho = 0$ and $\mathbf{J} = 0$) are assumed. The Maxwell equations in a linear medium are then

$$\begin{aligned}\nabla \times \mathbf{E} &= -j\omega\mu\mathbf{H} \quad , \quad \nabla \cdot \mathbf{E} = 0 \quad , \\ \nabla \times \mathbf{H} &= +j\omega\mu\mathbf{E} \quad , \quad \nabla \cdot \mathbf{H} = 0 \quad ,\end{aligned}\tag{A.1}$$

where $\mathbf{E}(\mathbf{r})$ and $\mathbf{H}(\mathbf{r})$ are complex phasors related to the actual fields by

$$\mathbf{E}(\mathbf{r}, t) = \text{Re} \{ \mathbf{E}(\mathbf{r}) e^{j\omega t} \} \quad , \quad \mathbf{H}(\mathbf{r}, t) = \text{Re} \{ \mathbf{H}(\mathbf{r}) e^{j\omega t} \} \quad ,\tag{A.2}$$

From Maxwell's equations one obtain

$$\nabla \times (\nabla \times \mathbf{E}) = -j\omega\mu(\nabla \times \mathbf{H}) = -j\omega\mu(j\omega\epsilon\mathbf{E}) = \omega^2\mu\epsilon\mathbf{E} \quad ,\tag{A.3}$$

$$\nabla \times (\nabla \times \mathbf{H}) = +j\omega\mu(\nabla \times \mathbf{E}) = +j\omega\epsilon(-j\omega\mu\mathbf{H}) = \omega^2\mu\epsilon\mathbf{H} \quad .\tag{A.4}$$

Using now

$$\nabla \times (\nabla \times \mathbf{A}) = \nabla (\nabla \cdot \mathbf{A}) - \nabla^2 \mathbf{A} \quad ,\tag{A.5}$$

one has

$$\nabla \times (\nabla \times \mathbf{E}) = \nabla (\nabla \cdot \mathbf{E}) - \nabla^2 \mathbf{E} = -\nabla^2 \mathbf{E} \quad ,\tag{A.6}$$

$$\nabla \times (\nabla \times \mathbf{H}) = \nabla (\nabla \cdot \mathbf{H}) - \nabla^2 \mathbf{H} = -\nabla^2 \mathbf{H} \quad .\tag{A.7}$$

The first two terms on the right-hand side of the equations vanish, due to $\nabla \cdot \mathbf{E} = 0$ and $\nabla \cdot \mathbf{H} = 0$. Thus,

$$-\nabla^2 \mathbf{E} = \omega^2 \mu \epsilon \mathbf{E} \quad , \quad -\nabla^2 \mathbf{H} = \omega^2 \mu \epsilon \mathbf{H} \quad , \quad (\text{A.8})$$

or

$$(\nabla^2 + \omega^2 \mu \epsilon) \mathbf{E} = 0 \quad , \quad (\text{A.9})$$

$$(\nabla^2 + \omega^2 \mu \epsilon) \mathbf{H} = 0 \quad . \quad (\text{A.10})$$

Since the waveguide is directed in z -direction (longitudinal direction), the ansatz

$$\mathbf{E}(x, y, z) = \mathbf{E}(x, y) e^{(\pm j k_z \cdot z)} \quad , \quad (\text{A.11})$$

$$\mathbf{H}(x, y, z) = \mathbf{H}(x, y) e^{(\pm j k_z \cdot z)} \quad . \quad (\text{A.12})$$

is assumed. Thus,

$$\frac{\partial^2 \mathbf{E}}{\partial z^2} = -k_z^2 \mathbf{E} \quad , \quad \frac{\partial^2 \mathbf{H}}{\partial z^2} = -k_z^2 \mathbf{H} \quad , \quad (\text{A.13})$$

and the two-dimensional equations

$$(\nabla^2 + \omega^2 \mu \epsilon) \mathbf{E} = [\nabla_T^2 + (\omega^2 \mu \epsilon - k_z^2)] \mathbf{E} = (\nabla_T^2 + k_T^2) \mathbf{E} = 0 \quad , \quad (\text{A.14})$$

$$(\nabla^2 + \omega^2 \mu \epsilon) \mathbf{H} = [\nabla_T^2 + (\omega^2 \mu \epsilon - k_z^2)] \mathbf{H} = (\nabla_T^2 + k_T^2) \mathbf{H} = 0 \quad , \quad (\text{A.15})$$

are obtained, where

$$\nabla_T^2 = \frac{\partial^2}{\partial x^2} + \frac{\partial^2}{\partial y^2} \quad , \quad (\text{A.16})$$

is the transverse part of the Laplacian operator in cartesian coordinates and k_T is the transverse wave number. The fields can now be separated into transverse and longitudinal (z -direction) components

$$\mathbf{E} = \mathbf{E}_z + \mathbf{E}_T \quad , \quad \mathbf{H} = \mathbf{H}_z + \mathbf{H}_T \quad , \quad (\text{A.17})$$

where $\mathbf{E}_z = E_z \mathbf{e}_z$, $\mathbf{H}_z = H_z \mathbf{e}_z$ and

$$\mathbf{E}_T = E_x \mathbf{e}_x + E_y \mathbf{e}_y \quad , \quad \mathbf{H}_T = H_x \mathbf{e}_x + H_y \mathbf{e}_y \quad . \quad (\text{A.18})$$

Let us now analyze Maxwell's equations $\nabla \times \mathbf{E} = -j\omega\mu\mathbf{H}$, $\nabla \times \mathbf{H} = j\omega\mu\mathbf{E}$ such that

$$\begin{aligned}\frac{\partial E_z}{\partial y} - \frac{\partial E_y}{\partial z} &= -j\omega\mu H_x \quad , \quad \frac{\partial H_z}{\partial y} - \frac{\partial H_y}{\partial z} = -j\omega\epsilon E_x \quad , \\ \frac{\partial E_x}{\partial z} - \frac{\partial E_z}{\partial x} &= -j\omega\mu H_y \quad , \quad \frac{\partial H_x}{\partial z} - \frac{\partial H_z}{\partial x} = -j\omega\epsilon E_y \quad , \\ \frac{\partial E_y}{\partial x} - \frac{\partial E_x}{\partial y} &= -j\omega\mu H_z \quad , \quad \frac{\partial H_y}{\partial x} - \frac{\partial H_x}{\partial y} = -j\omega\epsilon E_z \quad ,\end{aligned}\tag{A.19}$$

or combining the first two components of the equation $\nabla \times \mathbf{E} = -j\omega\mu\mathbf{H}$ in a different way

$$\left(\frac{\partial E_x}{\partial z} - \frac{\partial E_z}{\partial x}\right)\mathbf{e}_x - \left(\frac{\partial E_z}{\partial y} - \frac{\partial E_y}{\partial z}\right)\mathbf{e}_y = -j\omega\mu (H_y\mathbf{e}_x - H_x\mathbf{e}_y) \quad , \tag{A.20}$$

or

$$\frac{\partial}{\partial z} (E_x\mathbf{e}_x + E_y\mathbf{e}_y) - j\omega\mu(-H_y\mathbf{e}_x + H_x\mathbf{e}_y) = \left(\mathbf{e}_x\frac{\partial}{\partial x} + \mathbf{e}_y\frac{\partial}{\partial y}\right)E_z \quad , \tag{A.21}$$

or

$$\frac{\partial \mathbf{E}_T}{\partial z} - j\omega\mu (\mathbf{e}_z \times \mathbf{H}_T) = \nabla_T E_z \quad , \tag{A.22}$$

where

$$\mathbf{E}_T = E_x\mathbf{e}_x + E_y\mathbf{e}_y \quad , \tag{A.23}$$

$$\mathbf{e}_z \times \mathbf{H}_T = -H_y\mathbf{e}_x + H_x\mathbf{e}_y \quad , \tag{A.24}$$

$$\nabla_T = \frac{\partial}{\partial x}\mathbf{e}_x + \frac{\partial}{\partial y}\mathbf{e}_y \quad . \tag{A.25}$$

were used. Combining the first two components of the equation $\nabla \times \mathbf{H} = j\omega\mu\mathbf{E}$ in a similar way, one obtains

$$\frac{\partial \mathbf{H}_T}{\partial z} + j\omega\epsilon (\mathbf{e}_z \times \mathbf{E}_T) = \nabla_T H_z \quad , \tag{A.26}$$

Thus the complete set of Maxwell equations become

$$\begin{aligned} \frac{\partial \mathbf{E}_T}{\partial z} - j\omega\mu (\mathbf{e}_z \times \mathbf{H}_T) &= \nabla_T E_z \quad , \quad \mathbf{e}_z \cdot (\nabla_T \times \mathbf{E}_T) = -j\omega\mu H_z \quad , \\ \frac{\partial \mathbf{H}_T}{\partial z} + j\omega\epsilon (\mathbf{e}_z \times \mathbf{E}_T) &= \nabla_T H_z \quad , \quad \mathbf{e}_z \cdot (\nabla_T \times \mathbf{H}_T) = +j\omega\epsilon E_z \quad , \\ \nabla_T \cdot \mathbf{E}_T &= -\frac{\partial E_z}{\partial z} \quad , \quad \nabla_T \cdot \mathbf{H}_T = -\frac{\partial H_z}{\partial z} \quad , \end{aligned} \quad (\text{A.27})$$

where by definition

$$\nabla_T \times \mathbf{E}_T = \begin{vmatrix} \mathbf{e}_x & \mathbf{e}_y & \mathbf{e}_z \\ \frac{\partial}{\partial x} & \frac{\partial}{\partial y} & 0 \\ E_x & E_y & 0 \end{vmatrix} = \mathbf{e}_z \left(\frac{\partial E_y}{\partial x} - \frac{\partial E_x}{\partial y} \right) \quad . \quad (\text{A.28})$$

If E_z and H_z are known, they can be treated as "sources" of the transverse fields \mathbf{E}_T and \mathbf{H}_T , according to (A.27). In other words, if E_z and H_z are known, the transverse fields are uniquely determined by Maxwell's equations. Using here

$$\frac{\partial \mathbf{E}_T}{\partial z} = \pm jk_z \mathbf{E}_T \quad , \quad \frac{\partial \mathbf{H}_T}{\partial z} = \pm jk_z \mathbf{H}_T \quad , \quad (\text{A.29})$$

one has

$$\pm jk_z \mathbf{E}_T - j\omega\mu (\mathbf{e}_z \times \mathbf{H}_T) = \nabla_T E_z \quad , \quad (\text{A.30})$$

$$\pm jk_z \mathbf{H}_T + j\omega\epsilon (\mathbf{e}_z \times \mathbf{E}_T) = \nabla_T H_z \quad . \quad (\text{A.31})$$

From (A.31), one obtains

$$\mathbf{e}_z \times \mathbf{E}_T = \frac{1}{j\omega\epsilon} (\nabla_T H_z \mp jk_z \mathbf{H}_T) \quad . \quad (\text{A.32})$$

From (A.30), one can write

$$\mathbf{e}_z \times [\pm jk_z \mathbf{E}_T - j\omega\mu (\mathbf{e}_z \times \mathbf{H}_T)] = \mathbf{e}_z \times \nabla_T E_z \quad , \quad (\text{A.33})$$

or

$$\pm j k_z (\mathbf{e}_z \times \mathbf{E}_T) - j \omega \mu \mathbf{e}_z \times (\mathbf{e}_z \times \mathbf{H}_T) = \mathbf{e}_z \times \nabla_T E_z \quad . \quad (\text{A.34})$$

Since $\mathbf{e}_z \times \mathbf{E}_T = \frac{1}{j\omega\epsilon} (\nabla_T H_z \mp j k_z \mathbf{H}_T)$ and $\mathbf{e}_z \times (\mathbf{e}_z \times \mathbf{H}_T) = -\mathbf{H}_T$, one obtains

$$\pm \frac{j k_z}{j\omega\epsilon} (\nabla_T H_z \mp j k_z \mathbf{H}_T) + j \omega \mu \mathbf{H}_T = \mathbf{e}_z \times \nabla_T E_z \quad . \quad (\text{A.35})$$

Multiplying the above equation with $j\omega\epsilon$, one obtains

$$\pm j k_z (\nabla_T H_z \mp j k_z \mathbf{H}_T) - \omega^2 \mu \epsilon \mathbf{H}_T = j \omega \epsilon \mathbf{e}_z \times \nabla_T E_z \quad , \quad (\text{A.36})$$

or

$$\pm j k_z \nabla_T H_z - (\omega^2 \mu \epsilon - k_z^2) \mathbf{H}_T = j \omega \epsilon \mathbf{e}_z \times \nabla_T E_z \quad , \quad (\text{A.37})$$

or finally

$$\mathbf{H}_T = \frac{j}{\omega^2 \mu \epsilon - k_z^2} [\pm k_z \nabla_T H_z - \omega \epsilon \mathbf{e}_z \times \nabla_T E_z] \quad . \quad (\text{A.38})$$

By means of an analogous procedure, one obtains

$$\mathbf{E}_T = \frac{j}{\omega^2 \mu \epsilon - k_z^2} [\pm k_z \nabla_T E_z + \omega \mu \mathbf{e}_z \times \nabla_T H_z] \quad . \quad (\text{A.39})$$

This proves that for the non-vanishing of at least one of E_z or H_z , the transverse fields are determined by the above two results. Depending on the choice of E_z and H_z , there are several possible solutions. One special solution is the transverse electromagnetic (TEM) wave where $E_z = 0$ and $H_z = 0$. Based on the above analysis, it is seen that TEM waves cannot exist inside a single hollow waveguide. In other words, $\mathbf{E}_T = 0$ and $\mathbf{H}_T = 0$ everywhere inside the waveguide. Another two important examples have the following boundary conditions

- Transverse magnetic (TM) waves

$$H_z = 0 \quad (\text{everywhere}) \quad , \quad E_z \quad (\text{on the boundary } S) = 0 \quad , \quad (\text{A.40})$$

- Transverse electric (TE) waves

$$E_z = 0 \quad (\text{everywhere}) \quad , \quad \mathbf{n} \cdot \nabla H_z \quad (\text{on the boundary } S) = 0 \quad . \quad (\text{A.41})$$

Using now the results for \mathbf{E}_T and \mathbf{H}_T , one can write

$$\mathbf{e}_z \times \mathbf{E}_T = \frac{j}{\omega^2 \mu \epsilon - k_z^2} [\pm k_z \mathbf{e}_z \times \nabla_T E_z + \omega \mu \mathbf{e}_z \times (\mathbf{e}_z \times \nabla_T H_z)] \quad . \quad (\text{A.42})$$

Using $\mathbf{e}_z \times (\mathbf{e}_z \times \nabla_T H_z) = -\nabla_T H_z$, one obtains

$$\mathbf{e}_z \times \mathbf{E}_T = \frac{j}{\omega^2 \mu \epsilon - k_z^2} [-\omega \mu \nabla_T H_z \pm k_z \mathbf{e}_z \times \nabla_T E_z] \quad , \quad (\text{A.43})$$

$$\mathbf{e}_z \times \mathbf{E}_T = \frac{j}{\omega^2 \mu \epsilon - k_z^2} \left[\mp \frac{\omega \mu}{k_z} (\pm k_z \nabla_T H_z) \mp \frac{k_z}{\omega \epsilon} (-\omega \epsilon \mathbf{e}_z \times \nabla_T E_z) \right] \quad . \quad (\text{A.44})$$

For the case of TM waves ($H_z = 0$) one has

$$\mathbf{e}_z \times \mathbf{E}_T = \mp \left(\frac{k_z}{\omega \epsilon} \right) \frac{j}{\omega^2 \mu \epsilon - k_z^2} [-\omega \epsilon \mathbf{e}_z \times \nabla_T E_z] = \mp Z \mathbf{H}_T \quad , \quad (\text{A.45})$$

or

$$\mathbf{H}_T = \frac{\mp 1}{Z} \mathbf{e}_z \times \mathbf{E}_T \quad , \quad Z = \frac{k_z}{\omega \epsilon} \quad . \quad (\text{A.46})$$

For TE waves ($E_z = 0$) one has

$$\mathbf{e}_z \times \mathbf{E}_T = \mp \left(\frac{\omega \mu}{k_z} \right) \frac{j}{\omega^2 \mu \epsilon - k_z^2} [\pm k_z \nabla_T H_z] = \mp Z \mathbf{H}_T \quad , \quad (\text{A.47})$$

or

$$\mathbf{H}_T = \frac{\mp 1}{Z} \mathbf{e}_z \times \mathbf{E}_T \quad , \quad Z = \frac{\omega \mu}{k_z} \quad . \quad (\text{A.48})$$

Introducing here $k^2 = \omega^2 \mu \epsilon$, one has

$$Z = \left\{ \begin{array}{l} \frac{k_z}{\omega \epsilon} = \frac{k_z}{\omega \sqrt{\epsilon \mu}} \sqrt{\frac{\mu}{\epsilon}} = \frac{k_z}{k} \sqrt{\frac{\mu}{\epsilon}} \quad (\text{TM}) \\ \frac{\omega \mu}{k_z} = \frac{\omega \sqrt{\epsilon \mu}}{k_z} \sqrt{\frac{\mu}{\epsilon}} = \frac{k}{k_z} \sqrt{\frac{\mu}{\epsilon}} \quad (\text{TE}) \end{array} \right\} \quad . \quad (\text{A.49})$$

For TM waves, the impedance Z can be written as

$$Z = \frac{k_z}{\omega \epsilon} = \frac{1}{\omega \epsilon} \sqrt{k^2 - k_T^2} = \frac{1}{\omega \epsilon} \sqrt{\omega^2 \mu \epsilon - k_T^2} \quad , \quad (\text{A.50})$$

Thus,

$$k_z = \sqrt{\omega^2 \mu \epsilon - k_T^2} = \sqrt{\frac{\omega^2}{c^2} - k_T^2} = \frac{\omega}{c} \sqrt{1 - \frac{k_T^2 c^2}{\omega^2}} \quad . \quad (\text{A.51})$$

Furthermore, the TM waves can only propagate when

$$1 - \frac{k_T^2 c^2}{\omega^2} > 0 \quad \implies \quad \frac{k_T^2 c^2}{\omega^2} < 1 \quad , \quad (\text{A.52})$$

or

$$\omega^2 > c^2 k_T^2 \quad \implies \quad \omega > \omega_c = ck_T \quad . \quad (\text{A.53})$$

where ω_c is the cutoff angular frequency. Otherwise, the waves are evanescent.